Brigham Young University

BYU ScholarsArchive

2008-03-21

Characterization of Synthetic, Self-Oscillating Vocal Fold Models

James S. Drechsel
Brigham Young University - Provo

Follow this and additional works at: https://scholarsarchive.byu.edu/etd

Part of the Mechanical Engineering Commons

CHARACTERIZATION OF SYNTHETIC, SELF-OSCILLATING

VOCAL FOLD MODELS

by

James S. Drechsel

A thesis submitted to the faculty of

Brigham Young University

in partial fulfillment of the requirements for the degree of

Master of Science

Department of Mechanical Engineering

Brigham Young University

December 2007

BRIGHAM YOUNG UNIVERSITY

GRADUATE COMMITTEE APPROVAL

of a thesis submitted by

James S. Drechsel

This thesis has been read by each member of the following graduate committee and by majority vote has been found to be satisfactory.

Date	Scott L. Thomson Chair

Date	R. Daniel Maynes

Date	Mark B. Colton

BRIGHAM YOUNG UNIVERSITY

As chair of the candidate's graduate committee, I have read the thesis of James S. Drechsel in its final form and have found that (1) its format, citations, and bibliographical style are consistent and acceptable and fulfill university and department style requirements; (2) its illustrative materials including figures, tables, and charts are in place; and (3) the final manuscript is satisfactory to the graduate committee and is ready for submission to the university library.

_____
Date

_____
Scott L. Thomson
Chair, Graduate Committee

Accepted for the Department

_____
Matthew R. Jones
Graduate Coordinator

Accepted for the College

_____
Alan R. Parkinson
Dean, Ira A. Fulton College of Engineering and Technology

ABSTRACT

CHARACTERIZATION OF SYNTHETIC, SELF-OSCILLATING

VOCAL FOLD MODELS

James S. Drechsel

Department of Mechanical Engineering

Master of Science

The vocal folds are essential for speech production, and a better understanding of vocal fold vibration characteristics may help improve treatments of voice disorders. However, studying real vocal folds presents significant challenges. *In-vivo* studies are limited by access and safety issues. Excised larynges have a short useable lifetime (on the order of minutes) and are difficult to parameterize. In contrast, synthetic vocal fold models have long useable lifetimes and can be easily parameterized. In this thesis, a series of tests performed on recently developed synthetic, self-oscillating models of the human vocal folds are discussed. These tests include measurements of vibration frequency, sub-glottal pressure, and time-averaged flow rate. The differences between one-layer and two-layer synthetic models are evaluated. Comparisons are made between synthetic model and real vocal fold behavior. The synthetic model is shown to have vibrated at frequencies, pressures, and flow rates consistent with human phonation.

The influence of sub-glottal tube length on model vibration frequency is examined. Motion is observed using high-speed imaging. Velocity measurements of the glottal jet using particle image velocitmetry (PIV) were performed with and without an idealized vocal tract, including the effects of the false folds, for various cases of vocal tract asymmetry. Glottal jet velocities measured using PIV were consistent with velocities measured using excised larynges. A starting vortex was observed in all test cases. The presence of the false folds acted to restrain the sides of the starting vortex, and in some cases created new vortical structures shed from the false folds. An algorithm was created to calculate and visualize the jet core centerline. In the vocal tract cases, the glottal jet tended to skew toward the nearest wall; in the false fold cases, the opposite trend was observed as the jet skewed away from the nearest wall (towards the midplane). Plots of RMS velocity showed distinct regions of shear layer and jet core. Vocal tract cases at pressures much greater than phonation onset pressure showed significant increases in RMS velocities compared to open jet and false fold cases.

ACKNOWLEDGMENTS

A singular experience many years ago led me to mechanical engineering, and ultimately to this Masters degree. I am grateful to my Father in Heaven who took the time to give me the guidance I needed. It has been a privilege to study at Brigham Young University.

I would like to thank my advisor, Dr. Scott Thomson, for all of his guidance, time, and patience. I learned from him each time we met together; I could not have selected a better advisor. In particular, I am grateful for his insights into the various drafts of this thesis and for his enthusiasm for research in general. I would also like to thank the BYU Mechanical Engineering Department for the tuition scholarship I received, as well as NIH for research funding, both of which allowed me to focus on this thesis research full-time.

I am grateful to the rest of my committee, Dr. Daniel Maynes and Dr. Mark Colton for their willingness to help me evaluate and improve this thesis. I have enjoyed learned from and associating with both of them.

I am indebted to Jake Munger for fabricating all of the vocal fold models and test specimens used in this research, for performing the static testing described in Chapter 3, and for manufacturing most of the test fixture components.

Finally, I dedicate this work to my wonderful wife, Parie, and our daughter, Sophie, who bring so much joy to my life. I love them very much. Without them to enjoy it with, the accomplishment of completing this thesis would feel hollow indeed.

TABLE OF CONTENTS

LIST OF TABLES

LIST OF FIGURES

xviii

1 Introduction

1.1 Anatomy and Function of the Human Larynx

Speech is a vital part of human life. Many people use their voices professionally (e.g. teachers, singers). However, many people suffer from voice disorders. A better understanding of vocal fold behavior can lead to improvements in the treatment and prevention of voice-related problems.

Sound is produced when pressurized air from the lungs is passed through the larynx to the vocal tract (mouth and nose). When this pressure reaches a critical value ("onset pressure"), the region of the larynx called the vocal folds (commonly referred to as the vocal cords) will start to self-oscillate. The term "self-oscillation" in this sense refers to flow-induced vibration, where the tissue and fluid dynamics are coupled.

Figure 1-1 shows the basic anatomy of the larynx. The larynx connects the vocal tract and the lungs, thus occupying the front portion of the neck. The vocal folds are located roughly in the vertical center of the larynx, and are situated behind and below the laryngeal prominence of the thyroid cartilage (commonly referred to as the Adam's apple).
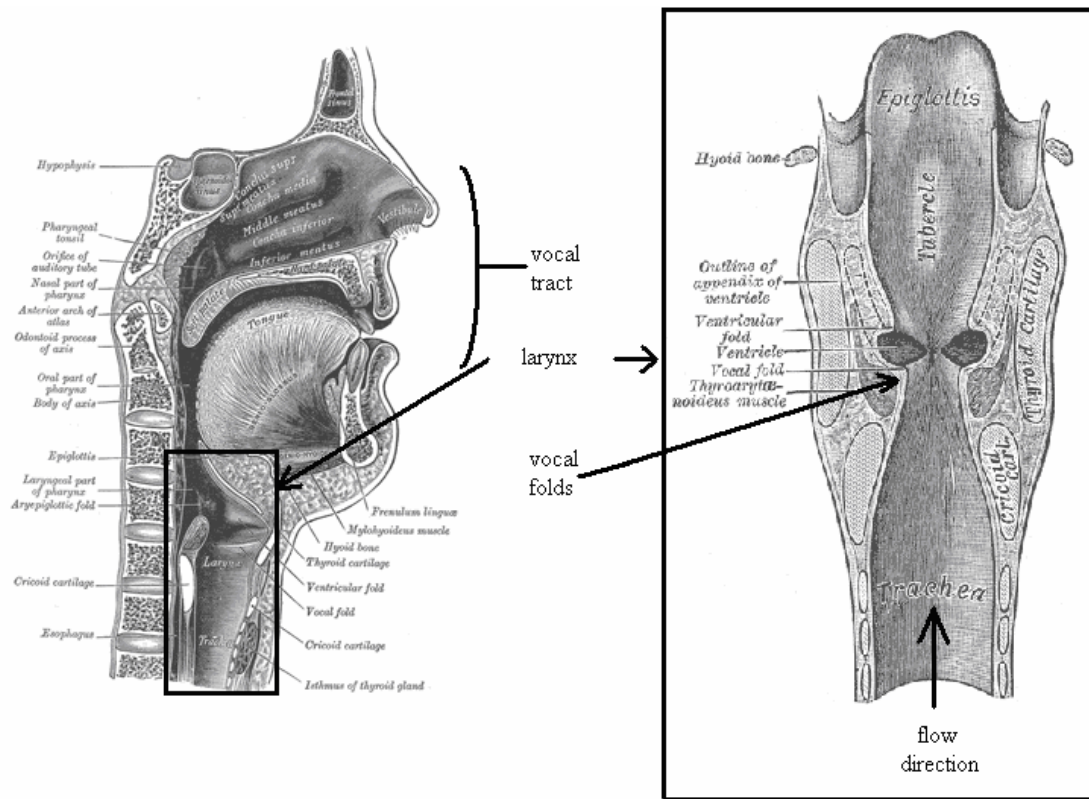
Figure 1-1 Basic anatomy of the human larynx: sagittal view of human head (left) and enlarged coronal view of larynx (right) (adapted from Gray's *Anatomy of the Human Body*, images public domain, www.bartleby.com).

The vocal folds, shown in greater detail in Figure 1-2, include both halves of a matching set of soft tissue "folds" attached to the laryngeal wall. They are approximately symmetric across the medial-sagittal plane and have a cross-section that is non-uniform in the anterior-posterior direction. The volume of space between the vocal folds is referred to as the glottis. The regions immediately above and below the vocal folds are termed, respectively, the supra-glottis and sub-glottis. The ventricular or false vocal folds are located just above the true vocal folds. In between the true and false folds is a space termed the laryngeal ventricle.
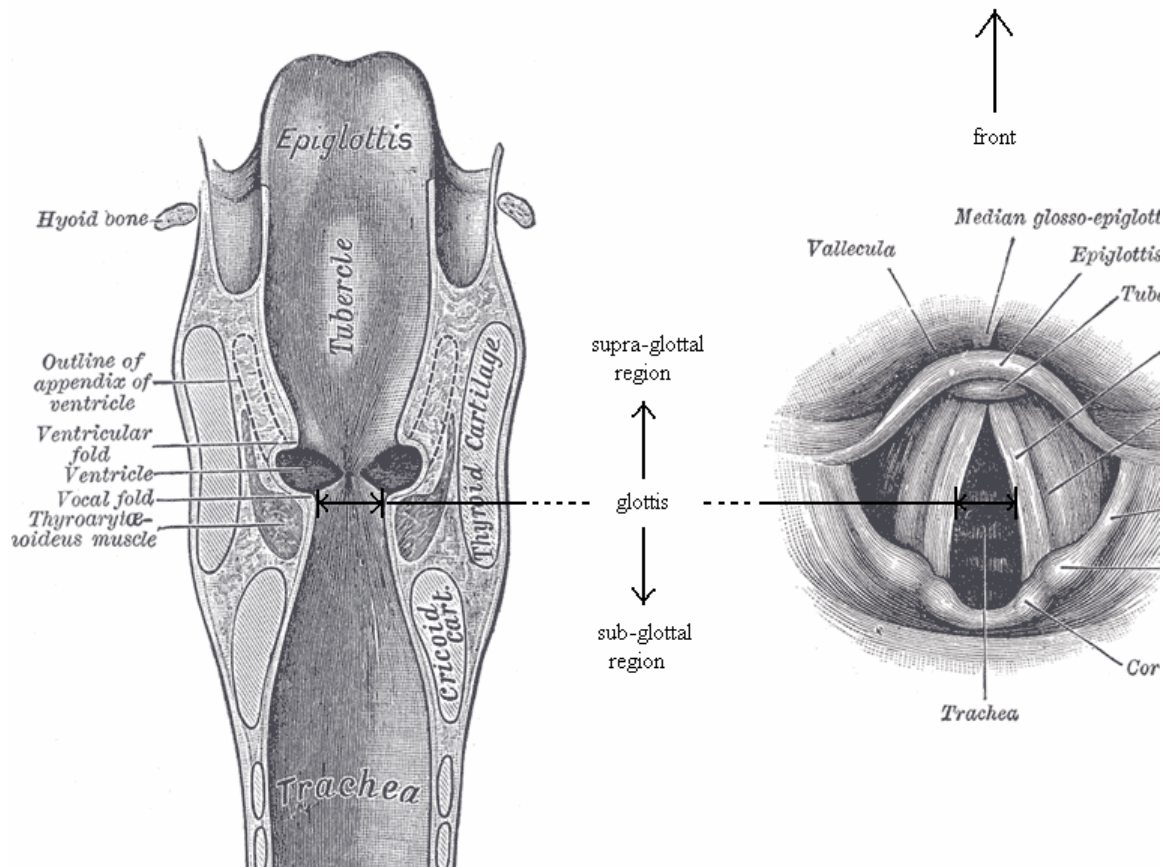
Figure 1-2 Coronal (left) and superior (right) views of human larynx (adapted from Gray's *Anatomy of the Human Body*, images public domain, www.bartleby.com).

Vocal fold vibration is strongly dependent on the composition of the mechanically-differing layers. It has been stated that "the most important notion of the structure of the vocal fold is that the vocal fold consists of multiple layers, each having its own mechanical properties" (Hirano and Kakita, 1985). Based on histological sections of the human vocal folds, Hirano and Kakita (1985) developed the "cover-body" theory of vocal fold anatomy, wherein the multiple tissue layers are grouped together, as illustrated in Figure 1-3.
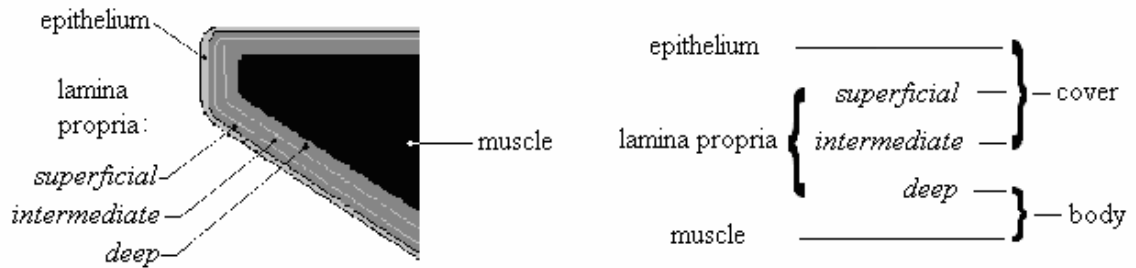
Figure 1-3 Idealized representation of the multi-layer composition of the vocal folds according to the cover-body theory of vocal fold vibration (layers not shown to scale).

General descriptions of the various vocal fold layers are summarized in Table 1-1 and briefly described here. The epithelium is very thin but has a relatively high modulus of elasticity. The superficial layer of the lamina propria is very soft (e.g., the consistency of gelatin). The intermediate and deep layers are elastic and have progressively denser distributions of relatively stiff collagen fibers. The epithelium and superficial and intermediate layers of the lamina propria constitute the "cover" layer. The loose cover facilitates the propagation of vertically-traveling waves on the vocal fold surface during vibration; these waves are an important ingredient in the generation of the time-varying flow rate (i.e., pulsating jet) that is the primary source of sound. The deep layer of the lamina propria and the vocalis muscle constitute the "body" layer and comprise the bulk of the vocal fold tissue. The muscle can contract or relax, thereby changing the stiffness of the body and the positioning of the vocal folds, thus affecting the vibrational qualities of the vocal folds. In addition to the vocalis muscle, there are several other intrinsic muscles attached to laryngeal cartilage which assist in vocal fold posturing and tension.

Table 1-1 Description of vocal fold layers (from Hirano and Kakita, 1985).

Layer		Typical thickness	Tissue type
Epithelium		50 μm	Stratified squamous cell
Lamina propria	*Superficial*	250 μm	Thin, loose collagen fibrils
	Intermediate	400 μm	Non-straight, bundles of elastic fibers
	Deep	400 μm	Densely crowded, spiraling collagen fibers
Muscle		7.3 mm	Muscle fibers

1.2   Voice Production Research using Vocal Fold Models

Studies have been performed to characterize various aspects of vocal fold vibration. Parameters of interest include intra-glottal pressure, glottal jet characteristics (including velocity and turbulence characteristics), vocal fold *in vacuo* modes of vibration, sound generation, airway surface layer adhesion, laryngeal geometry, and tissue mechanical and rheological properties. Methods for studying these parameters include real (*in-vivo* or excised) vocal folds, synthetic vocal folds, and computational models (some of these are discussed further in Chapter 2).

Methods which use real vocal folds have the advantage of physiological accuracy but present significant challenges. *In-vivo* studies are generally limited to superior imaging of the vocal folds using laryngeal endoscopy, which images often suffer from insufficient temporal and spatial resolution. Because of tissue sensitivity, excised larynges are typically only able to be vibrated for a few minutes and must be kept properly hydrated, which can present challenges to instrumentation and observation. *In-*

vivo and excised experiments are also limited in the potential for being used in detailed parametric studies involving vocal fold geometry and/or material properties.

Synthetic and computational vocal fold models can be useful tools to investigate the vocal folds as long as their behavior sufficiently approximates that of the real vocal folds. Synthetic models are useful for many reasons, including long usable lifetime (usually on the order of months) and ease of parameterization. However, they necessarily involve structural and material idealizations. A scientifically useful synthetic model of the vocal folds should incorporate multiple layers of differing material properties and be self-oscillating.

1.3 Thesis Research Overview

Thomson et al. (2005) introduced a new synthetic vocal fold model. This model is capable of being manufactured in such a way as to create distinct layers with differing material properties and is self-oscillating. The purpose of the research described in this thesis was to characterize this synthetic vocal fold model and modifications of this vocal fold model that included multiple layers (see Figure 1-4). Comparisons were made with previously published studies using synthetic, excised, and in-vivo larynges.

A test fixture was constructed that incorporated an idealized sub-glottal duct, a two-layer vocal fold model, and an idealized supra-glottal vocal tract that included the false vocal folds (see Figure 1-5). These sub- and supra-glottal tracts are important for many reasons, including their acoustic loading effect on vocal fold vibration and their potential for influencing the glottal jet.

idealized schematic   one-layer model   two-layer model
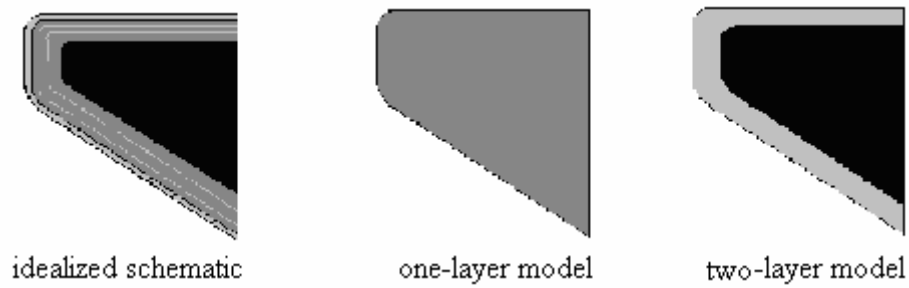
Figure 1-4 Conceptualization of one- and two-layer synthetic vocal fold models. In the one- and two-layer models, the cross-sections (out-of-the-page) are uniform, and each layer is isotropic.
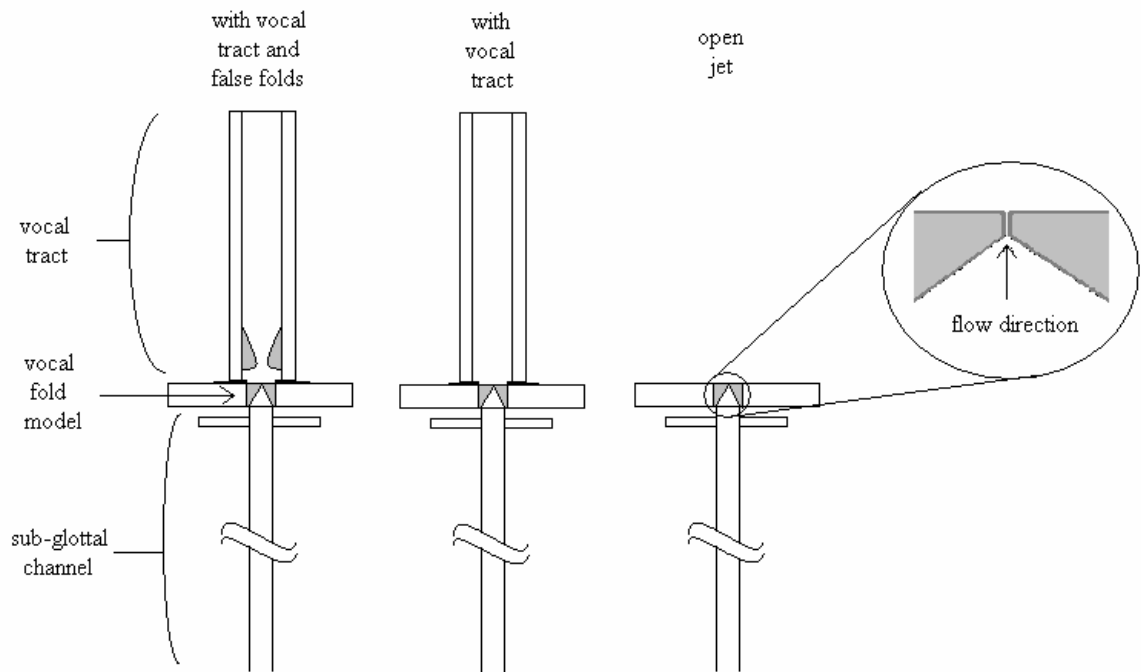
Figure 1-5 Schematic of different test sections.

The glottal jet was characterized in three cases: a free jet (no vocal tract), with a vocal tract but without false folds, and with a vocal tract and false folds. Measurements included oscillation frequency vs. sub-glottal pressure for varying sub-glottal tube

7

lengths, time-averaged flow rate vs. sub-glottal pressure, high-speed flow visualization, and two-dimensional flow velocity (using particle image velocimetry, or PIV).

1.4   Thesis Outline

Chapter 2 includes a review of previous experimental studies of vocal fold vibration using real and synthetic vocal fold models. Chapter 3 describes the model fabrication process and experimental setup. Results for experiments in which the model oscillation frequency vs. sub-glottal pressure was measured for varying sub-glottal tube lengths are reported, along with time-averaged flow rate vs. sub-glottal pressure data and stroboscopic flow visualization images. Chapter 4 presents qualitative and quantitative glottal jet measurements using high-speed imaging and PIV. Chapter 5 summarizes the main contributions of this thesis, discusses the significance of this synthetic model for future vocal fold research, and discusses areas for further work.

2   Literature Review

This chapter summarizes fluid mechanics-related vocal fold research with two purposes in mind. The first is to expose the reader to prior research, including *in-vivo*, excised, and synthetic larynx experiments. Since this thesis focuses on synthetic vocal fold models, studies using these types of models are emphasized in this chapter. The second purpose of this section is to highlight limitations common to these studies and show how this thesis research addresses some of these limitations.

In-vivo experiments are first discussed, followed by excised larynx experiments. The results from these studies comprise the basis for comparison with the synthetic model experiment results presented later in this thesis. Next, static synthetic models of the vocal folds are discussed. Lastly, various forms of dynamic (oscillating) synthetic vocal fold models are presented. This chapter ends with a summary of the limitations inherent in many of the experiments and a discussion of the ways in which this research addresses them.

2.1   *In-vivo* and Excised Larynx Experiments

Studies have been performed using *in-vivo* and excised larynx models, typically using either human or canine larynges. Canine larynges have been used because there exists a degree of similarity in size, geometry, and tissue properties with the human

larynx. While these experiments are, by definition, physiologically and anatomically realistic, they cannot be performed for long periods of time and are difficult to parameterize. Nevertheless, they have been very useful in studying various aspects of vocal fold vibration.

2.1.1 Jet Flow

Several studies have been performed to characterize the glottal jet, two of which are mentioned here. Alipour and Scherer (1995) performed a series of experiments designed to quantify the jet flow one centimeter above the vocal folds using several excised canine larynges. It was shown that evaluation of the flow parameters near the glottal exit at a single spatial location is inadequate since the flow field is unsteady and non-uniform. It was suggested that a more exhaustive study is necessary to understand the glottal jet and its characteristics. Advantages to this study include the use of real vocal folds and physiologically realistic pressures and flow rates. Limitations include that velocity data was collected using single-probe hot-wire anemometry so that no flow direction information was obtained, data was only acquired at a fixed distance from the glottal exit, and only the open jet case was evaluated.

Alipour et al. (1996) expanded on his previous work by measuring velocity distributions upstream and downstream of the glottis in an excised larynx, a static synthetic model, and a computational model. There were inconsistencies between the ways the different models were fixtured, namely that the excised larynx case was an open jet (the false folds and other downstream tissue being removed) and the synthetic model was not. The pressurized flow of air for the synthetic model was produced using suction, and thus a 32 cm length downstream section was in place, which acted as an

idealized vocal tract. Based on results presented for the computational model, it appeared as though some kind of downstream length had been assumed, but the details were not presented.

Khosla et al. (2007) used particle image velocimetry (PIV) and high-speed imaging to evaluate, respectively, the flow structures immediately downstream of the glottal exit and the vocal fold motion for three different canine larynges. The use of PIV yielded two-dimensional velocity field results, rather than point-wise velocity measurements, but the experiments only considered the open jet case for one sub-glottal pressure (the lowest pressure for which stable phonation could be obtained). The range of frequencies, sub-glottal pressures, and flow rates used in this study were 200 - 235 Hz, 0.49 – 0.69 kPa, and 185 – 450 mL/s, respectively. Phased-locked image acquisition was used to create average velocity (using 10 averages) vector fields over 30 phase positions. This number of averages is probably too few to expect the average velocity field to have converged, as discussed in Section 4.4.2, and was probably selected to reduce the length of time the excised larynges would be vibrating (resulting in a 2-3 minute vibration time). Observations included the description of various vortical structures near the glottal exit.

2.2   Synthetic Vocal Fold Models

A variety of synthetic models have been devised over the years. For the purposes of this thesis, they have been divided into three types: static models, driven models, and self-oscillating models.

2.2.1 Static Models

Numerous studies of static physical vocal fold models have been performed, e.g., Scherer et al. (1981, 1983, and 2001). These have been performed primarily to study the effect of intra-glottal profile on flow separation and intra-glottal pressure distributions. They have also observed the shape of the glottal jet and it's tendencies to skew based on exit geometry. The model geometry was based on laminograms of the human vocal folds, was scaled up to approximately seven times human size, and was rigid. Shinwari et al. (2003), using the same model as Scherer et al. (2001), also investigated intra-glottal pressures. This study used flow visualization to study jet skewing and flow separation location. Static vocal fold models rely on the quasi-steady assumption, which is not always valid (see Section 2.2.2).

2.2.2 Driven Models

Synthetic models of the vocal folds with motion prescribed via mechanical shakers have been used to study voice acoustics and glottal jet characteristics. Shadle et al. (1991) constructed a dynamic, life-size vocal fold model primarily for the purpose of flow visualization. While the scale was life-size, the dynamic case was significantly simplified by having only one of two thin, Teflon shutters representing the vocal folds driven together in simple harmonic motion by an electromechanical shaker; the glottal profile was rectangular. This configuration was described by the authors as representing one functioning and one paralyzed vocal fold. The driven model was placed in a square duct, with the model exit located 13.3 cm downstream from the glottal exit (i.e., a vocal tract). This model also included a set of false vocal folds. It was observed that the presence of the vocal tract delayed the jet growth. However, when the vibration

frequency matched the first resonance of the vocal tract, the jet started earlier in the cycle. The influence of the false folds in the downstream duct was described as straightening out the jet (so as to be parallel to the duct walls), even when the glottis itself was off-center. The geometry of the false folds, as well as their position downstream of the glottis, was not specified, but a test setup schematic showed the false folds positioned relatively close to the glottal exit, having hemispherical shapes. The sub-glottal length and its influence were not discussed.

Barney et al. (1999) and its companion paper Shadle et al. (1999) also used this setup to investigate the influence of glottal velocities on the glottal acoustic source. Again, the presence of a vocal tract was included. However, the false folds were not used and the square duct in which the model was placed was replaced with a cylindrical duct. Velocities were measured using hot-wire anemometry at three positions (centered in duct, and at two offset positions) at each of three downstream locations (1, 4, and 17 cm). Conclusions pertinent to this thesis included the observation of an unsteady jet exiting the glottis which became increasingly uniform as the flow continued downstream. They did not include a comparison between the open jet case and their vocal tract case.

Mongeau et al. (1997) developed a dynamic vocal fold model in the form of driven, life-size rubber pads with a more realistic convergent glottal profile. One goal was to validate the quasi-steady assumption of vocal fold vibration, which is that the fluid dynamics in the vibrating vocal fold are approximately the same as that in a series of static geometries with the same set of enforced operational conditions. Measurements using this model generally agreed with data presented using the static models of Scherer

(1981) and with excised canine experiments of Alipour and Scherer (1995). The quasi-steady assumption was validated for most of the glottal cycle. However, it was reported that the assumption did not hold for roughly 1/5th of the cycle (during glottal opening and closing).

Zhang et al. (2002, 2004) used this same driven model for further validation of the quasi-steady approximation for a pulsating jet issuing from the glottal exit and to study the effect of sound generation issues. These studies maintained that detailed flow information must be obtained to truly understand the glottal flow field. While Mongeau et al. (1997) studied an open jet with a driven convergent orifice, this study used various glottal profiles (convergent, straight, and divergent) and included a vocal tract. The measurements in these studies were primarily acoustic, accompanied by some flow visualization for illustrative purposes. This paper also inferred that the field downstream of the glottal exit is three-dimensional and turbulent in nature.

Alipour and Scherer (2001) used a mechanical hemi-larynx model to study pressure-flow relationships. The vocal fold model geometry had a bell-shaped profile, which was significantly steeper downstream than upstream of the glottis, and was fabricated from hard plastic. The model was driven by a small acoustic driver, attached to the vocal fold model by a rigid bar. This vocal fold geometry was more realistic than other driven models discussed above. The setup included both sub- and supra-glottal ducts (both of which were longer than those found in humans). Both static and dynamic cases were evaluated. In the dynamic cases, glottal width and vibration amplitude and frequency were varied. The static results showed the relationship between trans-glottal pressure drop and average flow rate to be quadratic. The dynamic results showed that

the glottal width had the most pronounced effect on flow resistance. Amplitude of oscillation was also important, but less so for higher glottal widths. Changes in flow resistance due to changes in frequency were insignificant.

Erath and Plesniak (2006a, 2006b, 2006c) used a static model similar to those used by Scherer to study pulsatile jet flow through a divergent glottis. These studies were performed in a wind tunnel on a 7.5× scaled-up model and included a downstream length to simulate a vocal tract. An unsteadiness generator (rotating shutters downstream of the model test section) was used to create pulsatile flow. This study used PIV to visualize and quantify the jet flow. They observed erratic, random lateral skewing of the jet in the vocal fold model. Small divergent angles were found to be bi-modal, meaning that the jet was as likely to attach to either vocal fold. However, in large divergent angles (>40°) the bi-modal feature disappeared and the jet never reattached to a wall. It was also observed that the jet attached to the side of greatest asymmetry. As the divergence angle increased, the length of attachment was found to increase. Lastly, the acceleration profile of a flow, rather than its pulsatile frequency, was found to control the occurrence of the Coanda effect.

None of the driven models described in this section incorporated multiple layers. None of them self-oscillated; rather, they required some form of external driving force to create the oscillations; the forcing frequency was constant. A few studies included a vocal tract and Shadle et al. (1991) included a false folds model, but none of the studies compared the vocal tract case with the open jet case.

2.2.3   Self-Oscillating Models

Self-oscillating vocal fold models have also been studied. Titze et al. (1995) developed a dynamic, synthetic vocal fold model that consisted of a stainless steel "body" covered by a silicone "epithelium". A hemi-larynx configuration was used. Between the epithelium and the body was a cavity into which fluids of varying viscosity were injected; this was to simulate the superficial layer of the lamina propria. This model was life-sized. The model cover self-oscillated, but the body was static. This behavior is perhaps typical of small-amplitude vocal fold oscillation. The membrane thickness was approximately 200 μm; recall that 50 μm is physically realistic. The following parameters were adjusted and measured: fluid viscosity (viscosity of water, 1 cP, to 20 cP), glottal profile, and prephonatory glottal half-width (0 to 2.5 mm). The fluid viscosity was lower than that of the real lamina propria; Chan and Titze (1997, discussed below) used improved viscosity fluids. They used a long (3 m) sub-glottal tube to try and avoid the influence of sub-glottal resonances. This model did not use a vocal tract. This paper concluded that increases in both glottal half-width and cover layer viscosity increased phonation threshold pressure.

Chan and Titze (1997), which used the same model, varied the cover layer thickness (1 to 2 mm) and found that phonation threshold pressure (PTP, the minimum pressure required to sustain oscillations) increased for increased membrane thickness and fluid viscosity. PTP was higher for onset than for offset. As these parameters decreased, PTP also decreased. In all cases, a thicker vocal fold body (i.e. rigid portion) exhibited lower PTP than the thinner vocal fold body. Glottal width had a strong effect on these results as well. There was a linear increase in PTP for glottal half width from 1

to 3 mm. At small glottal half-widths, collisions introduce non-linearity in the pressure vs. frequency relationship. They suggested the existence of an optimal glottal gap width (later studied by Lucero, 1998). Rectangular glottal profiles (parallel medial surfaces) were determined to provide the lowest PTP. They attributed certain divergent glottis behavior to the presence of flow separation. Highly divergent or convergent glottal profiles were subject to higher values of PTP.

Chan and Titze (2006) refined the Titze model by decreasing cover layer thickness to a more physiologically realistic 70 μm, and by using three kinds of biomaterials currently under consideration for use in phonosurgery of the lamina propria: hyaluronic acid, fat, and fibronectin. These materials were no longer applied through injection but were implanted between the epithelium layer and the body during manufacturing at a fixed thickness of 1 mm. These biomaterials are better matches for the lamina propria tissue because they possess viscoelastic properties. In addition to improvements in material properties, this study also included the effects of a supra-glottal tube on the vocal fold model vibration. However, the static nature of the body limited the model to small-amplitude studies only, which limits the applicability of the model to real vocal fold behavior. The analytical expressions discussed ignored the effects of the sub-glottal acoustics and fluid viscous resistance for small glottal half-widths. These omissions may explain why the analytical results did not more closely match the experimental data (right order of magnitude but the analytical slope was very different). Chan and Titze (2006) found that the presence of a vocal tract consistently reduced PTP.

Thomson (2004) and Thomson et al. (2005) developed a self-oscillating, synthetic vocal fold model made of a three-part silicone solution. The model consisted of only one layer (homogeneous and isotropic) and was generally geometrically similar to the real vocal folds, but with a uniform cross-section. A manufacturing process was suggested in which the model could be manufactured in separate layers of different material properties. Recently, the addition of fibers to the silicone matrix to produce a nonlinear stress-strain response typical of human tissue has been suggested (Drechsel et al., 2007a, b).

Others to have used Thomson's model include Zhang et al. (2006a, 2006b) and Neubauer et al. (2007). Zhang et al. (2006a) studied the effect of sub-glottal acoustics on vocal fold model vibration on a one-layer model (a silicone ratio of 1:1:2 was used [see Section 3.1.1], which corresponds to a modulus of elasticity of approximately 11 kPa). Model vibration frequency was measured as sub-glottal tube length was varied. The results indicated that the frequency of model vibration was strongly dependent on the sub-glottal tube length, and that future studies must take these upstream acoustic effects into consideration when analyzing results.

In a follow-up study, Zhang et al. (2006b) investigated the difference between aerodynamically- and acoustically-driven modes of vibration. Aerodynamically-driven modes were distinguished by vibration independent of acoustic resonances, and are generally deemed to be preferable over acoustically-driven modes of vibration because they are less prone to frequency register "jumps." The superior surface of the self-oscillating vocal fold model was three-dimensionally imaged using a prism, and using cross-correlation techniques, different modes of vibration were identified. Using the

same model as the previous study, it was determined that a one-layer model would only vibrate aerodynamically when most of its superior surface area was vertically restrained. This artificially-enforced boundary condition essentially created a thinner cover layer at the portion of the model not held by the restraining device, which better facilitated the propagation of a surface wave.

Neubauer et al. (2007) also used the one-layer version of Thomson's model to examine flow structures immediately downstream of the glottal exit. The experiments used PIV to quantify velocities and visualize near field flow structures. Values of frequency and flow rate were reported in the following ranges: 100 – 122 Hz, 480 – 630 mL/s, respectively (sub-glottal pressure was not reported). Flow visualization was also performed using a high-speed camera. Flow structures were extracted from the jet flow using a statistical technique referred to as "principal component analysis", which identifies correlated dynamics in patterns. Qualitative measured results included oscillating jet angle, shear layer structure, flapping of the turbulent region, and coherent structures. This study observed vortex generation, vortex convection, and jet flapping. A pseudo-vocal tract was used to increase seed density, but its dimensions (25.4 cm $\times$ 12.5 cm $\times$ 12.5 cm) were roughly 5 times the size of the real vocal tract; they stated that the influence of the tract wall on jet dynamics could be neglected (i.e. it was effectively an open jet case). The false folds were not included in the test setup. Hardware restrictions limited this study only a few quasi phase-locked flow images (i.e. instantaneous, rather than spatially averaged, data).

Other than the Chan and Titze (2006), none of the experiments involving self-oscillating models have used a realistic vocal tract or used multiple layer-models. It

should also be noted that the model used in Titze et al. (1995) and Chan and Titze (1997, 2006) was a hemi-larynx setup, thus inherently precluding the possibility for investigating asymmetrical behavior.

2.3   Summary

Each of the *in-vivo*, excised, and synthetic vocal fold models discussed in this chapter were developed to study a particular aspect of real vocal fold behavior. Most of the research examples in this chapter illustrate the relative ease with which synthetic vocal fold models are parameterized.

Some of the models used a hemi-larynx configuration, which precludes the study of asymmetric vibration. However, recent studies have suggested that normal vocal fold vibration commonly includes some degree of asymmetry (Shaw and Deliyski, in press). Of the synthetic models discussed, only Titze's (Titze et al., 1995; Chan and Titze, 1997, 2006) can be considered multi-layered, although Titze's model had a rigid body layer. Recalling the statement by Hirano and Kakita (1985), which stated that the multi-layered aspect of vocal fold tissue physiology was the single most important element of vocal fold structure, a case can be made for the creation and characterization of a self-oscillating, multi-layered synthetic vocal fold model.

Also, few studies included a vocal tract. As the vocal tract is always present in real phonation, this is an important deficiency in previous studies. Those that have used a vocal tract have generally failed to compare the glottal jet with and without a vocal tract; this is important for drawing conclusions based on open jet studies. Finally, only Shadle et al. (1991) included false folds in their experiments, about which she included

20

only one sentence stating that the false folds tended to straighten out the jet flow (even for an asymmetrically positioned jet).

The research described in this thesis includes comparisons of one- and two-layer synthetic vocal fold models to examine the influence of multiple layers on model behavior. The frequency vs. pressure relationship, in particular, was evaluated. The behavior of a two-layer model was investigated to see if it is any less dependent on sub-glottal acoustic resonances than the one-layer model. Finally, the effect of different supra-glottal configurations on glottal jet behavior was investigated. These geometries included an open jet, five cases of varying vocal tract asymmetry without false folds, and three cases of varying vocal tract asymmetry with false folds; all of these were studied at multiple sub-glottal pressures. Glottal exit velocity was measured quantitatively using PIV and observed qualitatively using high speed imaging.

3 Flow Measurements

In this chapter the fabrication of a synthetic, self-oscillating two-layer body-cover model of the vocal folds is described. Measurements of the material properties are presented. Results are reported of dynamic tests, including the measurement of frequency vs. time to study model consistency, frequency vs. mean pressure to quantify the range of attainable frequencies (and the requisite pressures) for these synthetic models, stroboscopic flow visualization of the glottal jet, and frequency vs. sub-glottal tube length to examine the influence of sub-glottal acoustics on model behavior. Time-averaged flow rate and medial-lateral glottal displacement data are also presented.

3.1 Model Fabrication

3.1.1 Material Properties

The synthetic models used in this research were created using three-component addition-cure silicone (single-part Everflex^{TM} and two-part Evergreen 10^{TM}, Smooth-On, Inc.) The components were mixed in varying ratios of Evergreen 10 (Part A) **:** Evergreen 10 (Part B) **:** Everflex. Everflex reduces the material modulus of elasticity. For example, a ratio of 1:1:5 yields a much more flexible model than a ratio of 1:1:1.

3.1.2 Synthetic Vocal Fold Fabrication

The synthetic vocal fold geometry was based on dimensions given by Scherer et al. (2001); see Fig. 3-1. The process for fabricating the two-layer synthetic vocal fold model is illustrated in Figure 3-2 and is as follows. A CAD model was created using the software package Pro/Engineer, from which various rapid-prototype models were created. Each of these rapid prototype pieces was designed to create a different cover layer thickness. A single mold was created using the original one-layer rapid prototype as follows. The rapid-prototype model was sprayed with a universal release agent (Smooth-On, Inc., Universal Mold Release). A mold-making compound, Smooth-Sil 950 (also made by Smooth-On, Inc.), was poured around the rapid prototype model and allowed to cure.
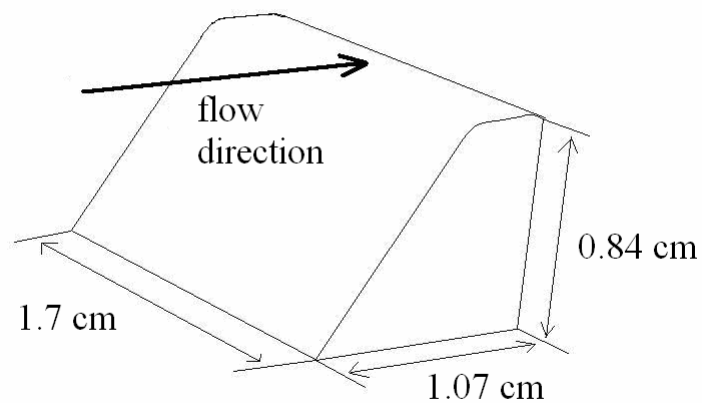
Figure 3-1 Geometry of synthetic vocal fold model.
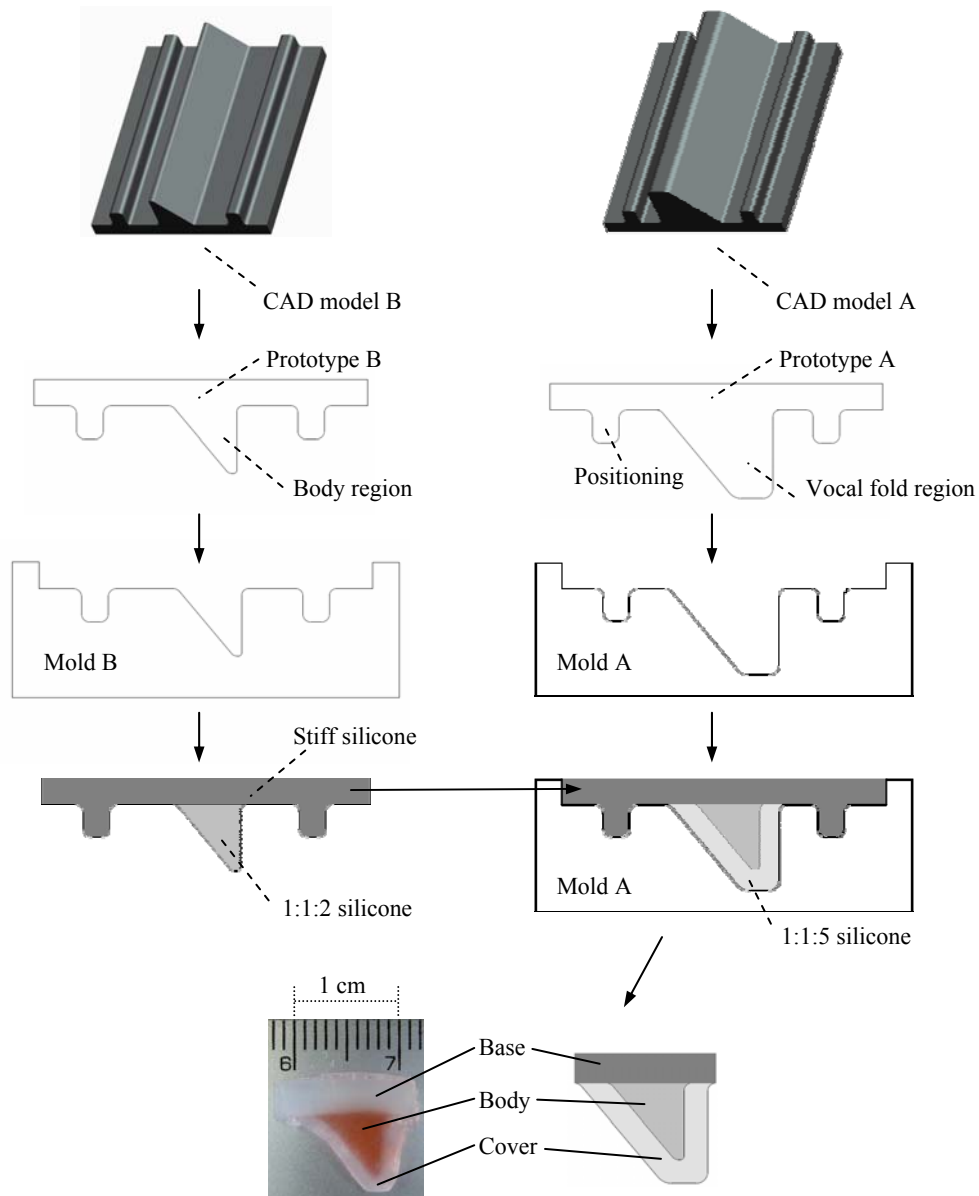
Figure 3-2 Schematic of the two-layer vocal fold fabrication process, including computer model generation, rapid prototyping, and molding of the different layers.   Shown at lower left is an image of the cross section of the vocal fold model. (Figure from Riede et al., in review.)

After removal of the rapid-prototype model from the newly created mold, a small

portion of a selected ratio of the three-part silicone solution was poured into the mold to

form the cover layer; the rapid prototype piece for the particular cover layer thickness of

interest was then inserted, along with appropriate application of the release agent. After

the cover layer had cured, the rapid prototype piece was carefully removed and the remainder of the mold was filled with the selected body ratio of the three-part silicone solution. Further details regarding the model fabrication process can be found elsewhere (Thomson, 2004; Thomson et al., 2005; Riede et al., in review).

3.2   Test Fixtures

In the course of this thesis research, two different test fixtures were used to mount the vocal fold model and necessary instrumentation. These are described below.

3.2.1   Test Fixture A

A test fixture ("Test Fixture A") was used to attach the vocal fold model to the accompanying sub- and supra-glottal systems; it is illustrated in Figure 3-3 and shown in Figure 3-4. Two vocal fold models were each attached to a separate rectangular acrylic plate (see Appendix A for drawings). These acrylic plates supported the vocal fold models and provided a surface for mounting to the sub- and supra-glottal tracts. The gap between the acrylic plates was sealed using closed-cell foam. The two acrylic pieces were brought together, compressing the closed-cell foam and bringing the synthetic vocal folds to within about one millimeter (or less) of each other. (Vocal fold behavior is sensitive to this gap size, see Lucero, 1996, but this was not one of the parameters selected for examination.) Bolts through the orifice plate were then tightened to control the initial glottal gap.

The acrylic plate assembly was positioned between a base plate and an orifice plate; these were sealed together by tightening the same two bolts (Fig. 3-4) as mentioned in the previous paragraph, with a rubber gasket and a small amount of vacuum grease

between the bottom of the acrylic pieces and the base plate. A sub-glottal (upstream) duct was attached to the base plate. It was fabricated from 1.25 cm thick aluminum, and had a square, internal cross-sectional area of 5 cm^2, which is approximately the area of the adult human trachea. It was 22.9 cm in length, and was capable of being simultaneously instrumented with a microphone and pressure tap at the same upstream location. A geometrically identical supra-glottal (downstream) duct (not shown in Figure 3-4) was fabricated, although it was not used in any of the measurements reported in this chapter. It was used in the measurements reported in Chapter 4, where details are provided.
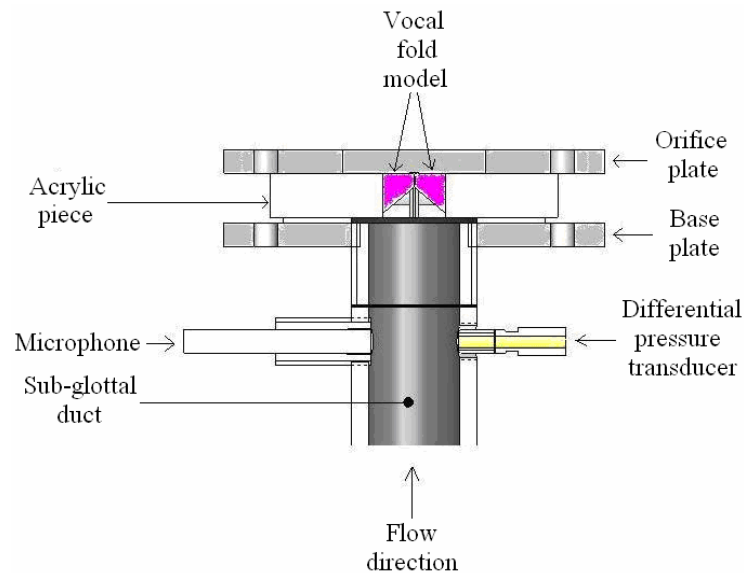
Figure 3-3 Cross-section schematic of Test Fixture A with instrumented sub-glottal tube attached.
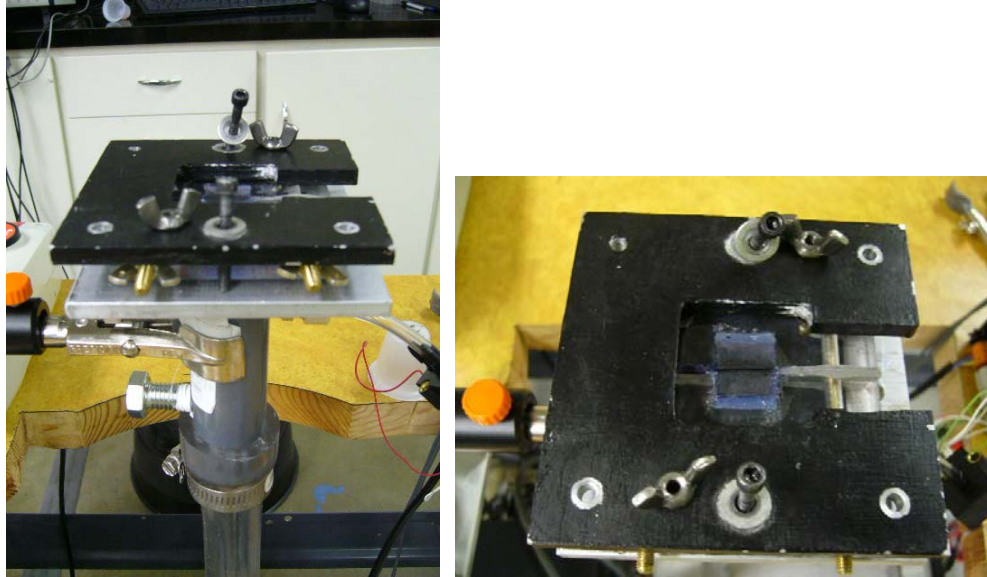
Figure 3-4 Test Fixture A with sub-glottal tube attached (seen at left as PVC tubing).

3.2.2   Test Fixture B

This setup was modified to improve control of the initial glottal gap, improve the seal between the vocal fold model and the orifice plate, remove visually-obstructive elements, refine sub-glottal geometry, and increase the ease with which the assembled model was mounted to the test apparatus. The change (see Figure 3-5) involved the following: eliminating the orifice plate, redesigning the acrylic plates using two bolts to attach each acrylic-vocal fold assembly to the base plate, using another set of bolts to seal the gap between the acrylic plates, and replacing the rectangular sub-glottal duct with a circular PVC pipe section of the same cross-sectional area (~5 cm^2). This modified version is referred to as Test Fixture B; dimensions can be found in Appendix A.
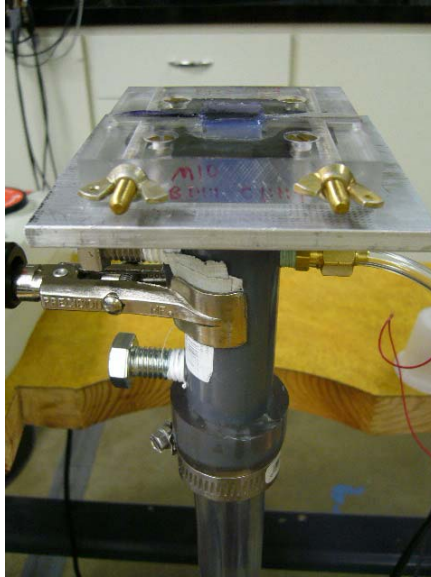
Figure 3-5 Test Fixture B.

3.2.3   Other Equipment Used with the Test Fixtures

The following equipment was used in conjunction with Test Fixtures A and B to facilitate the various measurements described throughout this thesis. Shop air was used as a flow source, with a pressure regulator (Pneufine 26129-1C-19, CKD Corp.) introduced to minimize source pressure fluctuations. A flow meter (Omega FL 4611, for measurements in Section 3.4.2, or a lower flow Matheson 605 for the measurements reported in Chapter 4, Section 4.4.1) was connected between the pressure regulator and a plenum. The plenum was used in some experiments to slow the airflow and to create a more uniform flow condition at the sub-glottal tube entrance. When used, the plenum was connected between the flow meter and the test fixture base plate.   It was manufactured from 3.175 mm thick plate aluminum, measured 30.5 cm on each side, and included inlet and outlet ports and interior flow straightening structures.

A differential pressure transducer (Omega PX138-001D5V) was placed in the sub-glottal duct approximately 3 cm upstream of the vocal fold model. This distance was selected to be about as close to the model as was physically practical. The transducer was connected to the sub-glottal tube via a 4.3 mm diameter, 8 cm length clear vinyl tube and fitting.

A microphone (GRAS 40BE, and later Larson Davis 2250) was placed at the same distance upstream of the glottis as the fitting for the relative pressure transducer. A data acquisition system (National Instruments PXI-1042Q) was used to collect data from the microphone and pressure transducers. Data was typically recorded at 3 kHz. Various LabVIEW^{TM} VI's (virtual instruments) were developed for the various experimental measurements. Example VI's are included in Appendix B.

A strobe light (Strobotac 1546) was used to illuminate the vocal folds while vibrating. In order to effectively visualize the model vibration using a digital camera, a strobe light was used to "sample," or discretize, the vocal fold motion. The lights in the room were turned off and the frequency of the strobe light was set to be just less than the model's vibration frequency. Because of the slight phase difference between the strobe light and the vocal fold frequencies, the vocal fold was observed to slowly proceed through its oscillation cycle. A digital video camera (Panasonic PVGS400) was used to record images of the model.

A LaVision aerosol generator was used to seed airflow in the flow visualization and PIV measurements. Regular olive oil was used for the tests in Chapter 3. DEHS oil was used for the PIV measurements in Chapter 4 (see Section 4.4.2 for details). Fine-

tuning of the seed density was required for the PIV measurements and is discussed in Section 4.4.1.

A set of variable length tubes was constructed out of flexible PVC tubing and electrical conduit, as shown in Figure 3-6, for the variable sub-glottal tube length experiments discussed in Section 3.4.6. The dimensions of the different tubes and fittings were selected to maintain as constant of an inner diameter as possible. The cross-sectional area of the tube section matched the sub-glottal duct ($\sim$5 cm^2). The PVC tubing (2.54 cm) slid over the outside of the electrical conduit (2.3 cm); the assembly was sealed using hose clamps. Standard conduit and PVC fittings were used at either end of the variable length tube to connect to the plenum (discussed below) and the sub-glottal duct.
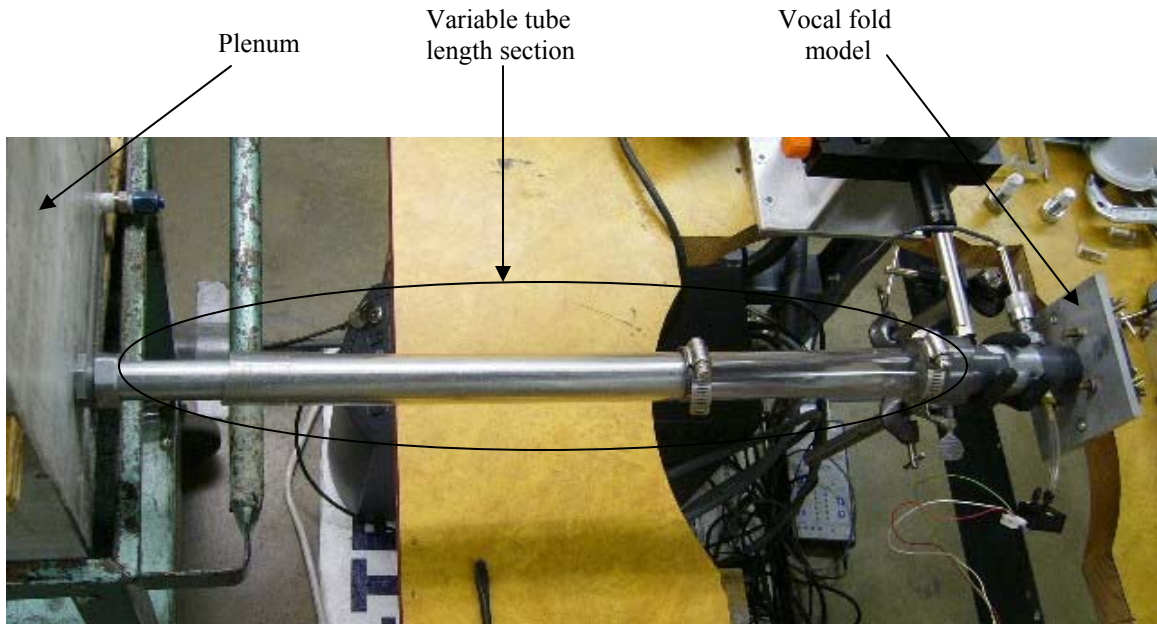
Figure 3-6 Variable sub-glottal tube length test setup.

3.3   Static Properties

Dozens of different synthetic vocal fold models were created in the course of this research. Each time a model was created, a cylindrical test specimen was simultaneously created using the same batch of silicone. These specimens were tested using an Instron 3342 tensile testing apparatus. The tensile testing procedure consisted of a pre-stressing cycle, followed by a tensile test to measure the tangent modulus. The tangent modulus, also referred to as the differential modulus, is the slope of the line tangent to the stress-strain curve at each successive data point. The tangent modulus was used rather than the Young's modulus, following the suggestion of Hirano and Kakita (1985) for vocal fold testing, which states that the tangent modulus is more appropriate for small variations in elongation with respect to the total length. The tensile testing was accomplished by attaching an aluminum fixture to each end of the test specimen using silicone adhesive. The specimens were about 7 cm long and 0.64 cm in diameter.   Specimens were generally strained to about 40%. The stress-strain curves were generally linear over this strain range (thus the tangent modulus was approximately equal to the Young's modulus).

Table 3-1 Tangent modulus data for different three-part silicone solution ratios.

	Tangent modulus, (kPa)		
Ratio	Maximum	Minimum	Average
1:1:0	67.21	63.85	65.44
1:1:1	22.86	22.02	22.54
1:1:2	11.36	10.49	10.88
1:1:3	6.97	5.48	6.02
1:1:4	5.15	3.02	4.10
1:1:5	2.57	1.18	2.00

Tangent modulus values ranging from 1.18 kPa to 67.2 kPa were measured for various silicone compound ratios. These are listed in Table 3-1, where the average values represent the average of 3 specimens.

Poisson's ratio, v, was also estimated by imaging the test specimen before and during testing. These images included a calibration length and were processed using a MATLAB script to locate the un-strained and strained locations of individual image points, allowing the estimation of Poisson's ratio according to the formula

$$v = \frac{\varepsilon_{transverse}}{\varepsilon_{axial}}, \tag{3.1}$$

where ε is strain. These measurements were only approximate, primarily due to resolution limitations of the camera, but are included here for reference in Table 3-2.

Table 3-2 Measured Poisson's ratio values for three-part silicone solution.

Ratio	Poisson's Ratio		
	Maximum	Minimum	Average
1:1:0	0.42	0.38	0.40
1:1:1	0.44	0.35	0.40
1:1:2	0.40	0.29	0.35
1:1:3	0.40	0.30	0.33
1:1:4	0.42	0.31	0.36
1:1:5	0.45	0.22	0.32

In later studies the vocal fold models themselves were used in the tensile testing. The tensile aluminum fixtures were bonded to each end of the vocal fold model prior to

being attached to the acrylic mounting plates. Following tensile testing the vocal fold model was severed from the aluminum fixtures and placed in the acrylic plates.

3.4   Dynamic Properties

Table 3-3 lists the names and geometries of the models tested and reported in Chapters 3 and 4. Most of the pressures required to initiate self-oscillation ranged from 0.6 to greater than 6 kPa. These values are above the typical onset pressure for normal human phonation, but are within the limits of human speech.

Table 3-3 Details of the models used in testing.

Model #	Ratio*	# of layers	Cover thickness (mm)	Notes
3	1:1:5	1	NA	rayon-poly cross-hatch weave
10	1:1:1	1	NA	short, cotton fibers overlapped
21	C1:1:5/B1:1:2	2	0.5	
28	1:1:4	1	NA	
29	1:1:5	1	NA	
30	C1:1:5/B1:1:3	2	0.5	
31	C1:1:5/B1:1:2	2	0.5	
34	C1:1:5/B1:1:2	2	0.25	
35	C1:1:5/B1:1:2	2	0.75	
36	C1:1:5/B1:1:2	2	1.5	
37	C1:1:5/B1:1:2	2	2	
M1	C1:1:5/B1:1:2	2	2	acrylic fibers in body
M3	C1:1:4/B1:1:1	2	>2	
M4	C1:1:4/B1:1:0	2	2	
M9	C1:1:5/B1:1:1	2	2	
M10	C1:1:4/B1:1:1	2	2	
M11	1:1:4	1	NA	

* C=cover layer, B=body layer

A few model preparatory steps were common to most experiments:

- A small amount of talcum powder was applied to the surface of the model in order to minimize adhesion of the vocal folds medial surfaces during vibration. This was done prior to the model being mounted in the test setup.

- The model was placed in the test fixture.

- A regulated flow of pressurized air was sent through a series of tubes to the vocal fold model. The onset pressure was measured by slowly increasing the pressure until the model started to vibrate. This process was repeated twice. The first time the model was vibrated served to relax the material; therefore, the recorded values of onset pressure were taken from the second start-up.

The complete upstream test system can be seen in Figure 3-7; it did not include the plenum. The total length of the upstream tubular system consisted of a 22.9 cm long, aluminum square duct (cross-sectional area of 5 cm^2) attached with a fitting to a 1.88 m length of standard 1.59 cm ID flexible PVC tubing, which was then connected to a 3.81 m length of standard 0.95 cm ID flexible PVC tubing. The fittings introduced abrupt changes in cross-sectional area. The smallest diameter tube was connected to the flow meter. Using this configuration, the following tests were performed: initial measurements of frequency and time-averaged flow rate vs. upstream pressure, maximum lateral glottal displacement, and model consistency.
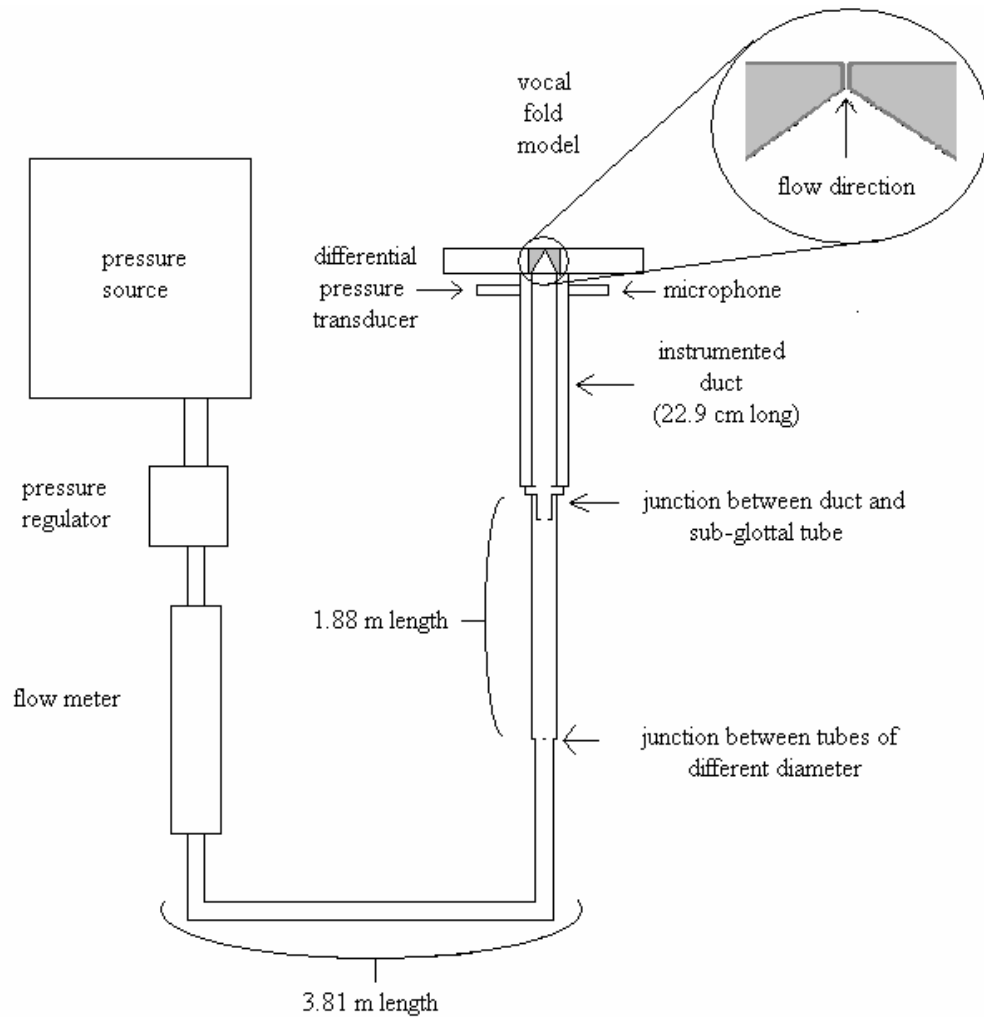
Figure 3-7   Upstream test system used in frequency vs. mean sub-glottal pressure, time-averaged flow rate, lateral glottal displacement, and model consistency experiments.   As shown, the test configuration is that of a free, or open, jet at the glottal exit.

3.4.1   Frequency vs. Pressure

The relationship between frequency and sub-glottal pressure for models with various material properties and cover thicknesses was measured.   In particular, the behavior of one- and two-layer models was compared.   While previous studies have used one-layer models (Thomson et al., 2005; Zhang et al., 2006a, b; Neubauer et al., 2007),

36

this is the first research to use a two-layer version; the effect of the cover layer on vibration is therefore unknown. The cover thicknesses ranged from 0.25 mm to 2 mm, the cover layer ratio was always 1:1:5, and the body layer ratio was varied from 1:1:1 to 1:1:3 (see Section 3.1.2 for two-layer model fabrication process).

Titze et al. (1995) states that phonation threshold pressure (PTP) "is a measure of 'ease' of phonation." PTP has an onset and offset value, and these values represent the minimum pressures required to initiate and maintain phonation, respectively (Chan and Titze, 1997). Values of onset PTP for the synthetic models were measured by increasing the pressure until the model began to vibrate, at which point measurements of frequency, mean sub-glottal pressure, time-averaged flow rate, and lateral glottal displacement were made. The pressure was then increased by a small increment (e.g. ~ 0.10 kPa), and the measurements were repeated until some maximum pressure was reached. This maximum pressure varied for each model and was selected to be the highest pressure at which the model vibration appeared to be on the verge of becoming chaotic, at which point the model was much more likely to become damaged through adhesion and separation of the vocal folds' medial surfaces. This threshold was audibly identified as a substantial increase in the complexity of the radiated sound.

Figure 3-8 shows the measured relationships between pressure and frequency; the data shown represent time-averaged values. Typical human values of PTP are on the order of 0.3 kPa at 100 Hz (Verdolini-Marston et al., 1990, 1994). Alipour and Scherer (1995) reported canine experiments that resulted in measured values of sub-glottal pressure as high as 1.37 kPa (pressure for maximum lateral glottal width), but added that these values are realistic for human phonation as well. Doellinger and Berry (2006)

stated that the excised human vocal folds used in the study vibrated at sub-glottal pressures ranging between 2.17 and 3.17 kPa and in the frequency range of 115 to 140 Hz (the excised larynx had been harvested from a 76-year old man). The frequency and pressure magnitudes reported in Figure 3-8 are of the same order of magnitude as those reported by Doellinger and Berry (2006), but higher than that for typical human phonation. The elevated PTP for the models tested here was presumably because the models were generally stiffer than the real vocal folds, and also possibly because of sub-glottal acoustic dependencies. However, the frequencies measured here are comparable to values reported in the above-mentioned vocal fold studies.
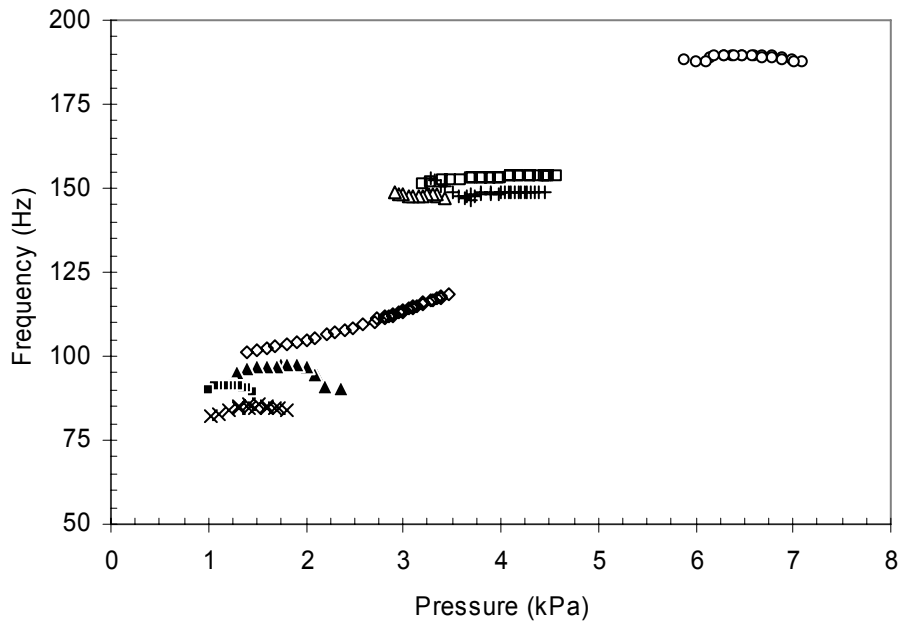
Figure 3-8 Frequency vs. mean sub-glottal pressure. (▲ = Model 28, ■ = Model 29, × = Model 30, + = Model 31, ○ = Model 34, □ = Model 35, △ = Model 36, ◇ = Model 37.)

Model 34 was determined to be the stiffest of the models because it had an almost negligible cover thickness (0.25 mm) and a body ratio of 1:1:2. Consequently, it showed

38

the highest measured fundamental frequency of 189.5 Hz. Practically speaking, fabrication of the thinnest cover layer (0.25 mm) was extremely difficult and it is possible that the Model 34 cover thickness was negligible. Three models (31, 35, and 36) vibrated at similar frequencies (~ 150 Hz). These three models also had a body ratio of 1:1:2, but all had slightly thicker cover layers (0.5, 0.75, and 1.25 mm, respectively).

The final grouping of four models (28, 29, 30, and 37) displayed the lowest measured frequencies. Models 28 and 29 were one-layer and had the most compliant material properties (1:1:4 and 1:1:5, respectively). The lowest measured frequency was observed with model 30, a two-layer model with a body ratio of 1:1:3, a cover ratio of 1:1:5, and a 0.5-mm thick cover. Its frequency would possibly have been expected to be higher than that of either model 28 or 29, given its stiffer body. Model 37 was also a two-layer model and had the thickest cover (2 mm). The two-layer model with the thickest cover (model 37) exhibited a wider range of frequencies and vibrated over a larger range of pressures than the other models similarly tested. The other models' frequencies of vibration did not change significantly with pressure. Some jumps were observed in vibration frequency for Models 28 and 31. This is possibly due to interactions with the sub-glottal acoustic system (discussed in Sec. 3.4.6). Following the data of Models 31 through 37, it is apparent that increasing the cover thickness tends to reduce the model fundamental frequency.

3.4.2   Time-Averaged Flow Rate vs. Pressure

Time-averaged flow rate data is shown in Figure 3-9. The slopes of the flow rate curves are approximately linear or quadratic. Alipour and Scherer (2001) noted that in general, flow rate and pressure have a quadratic relationship. Data was only acquired

over a relatively small range of pressures, so large quadratic behavior may not be expected to be visible. Further, since the flow rate and pressure data was acquired using a time-varying orifice, the quadratic pressure-flow relationship may not necessarily be expected. The flow rate data measured in this study is an order of magnitude higher than data reported from excised larynx experiments, such as Doellinger and Berry (2006), which reported time-averaged flow rates varied between 200 − 400 mL/s for an excised human larynx. Alipour and Scherer (1995) reported flow rates around 230 ml/s.
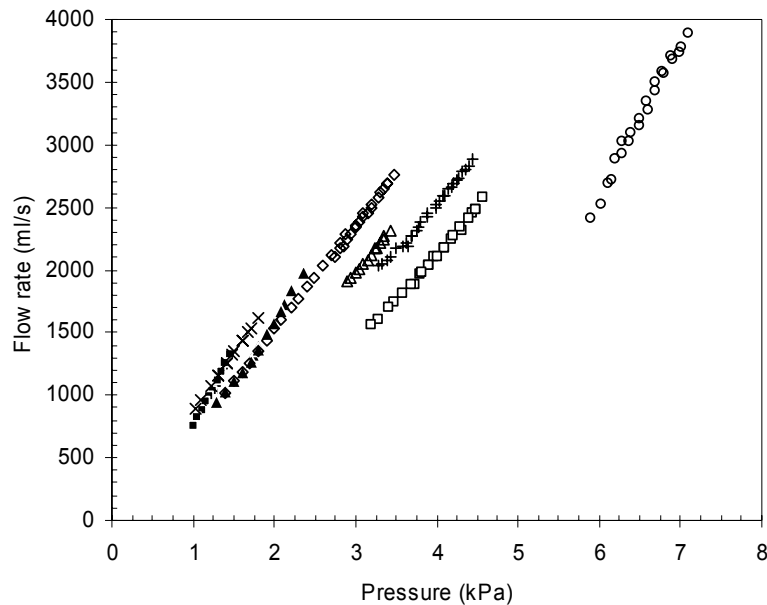
**Figure 3-9 Time-averaged flow rate vs. mean sub-glottal pressure. (▲ = Model 28, ■ = Model 29, ×
= Model 30, + = Model 31, ○ = Model 34, □ = Model 35, △ = Model 36, ◇ = Model 37.)**

The observed higher flow rates for models tested here are attributed to two potential sources. First, the models' oscillation patterns differed somewhat from that of the human vocal folds, and in general appeared to have a larger glottal opening throughout vibration (i.e., the time the orifice was open may have been larger than that

which is typical of human speech). Second, the initial glottal width was potentially larger

for these tests (always less than 1 mm, but never zero) than that which occurs in human

speech (which can be zero). As mentioned in Section 3.2.1, model behavior can be

sensitive to this glottal gap, but the glottal gap values were not of primary interest in this

research and were not rigorously controlled.

3.4.3   Amplitude of Glottal Displacement

Digital video of the view of the vocal folds was analyzed to measure the initial

(pre-vibratory) glottal width and the maximum glottal width during vibration. The image

analysis was performed in MATLAB (sample code included in Appendix B).
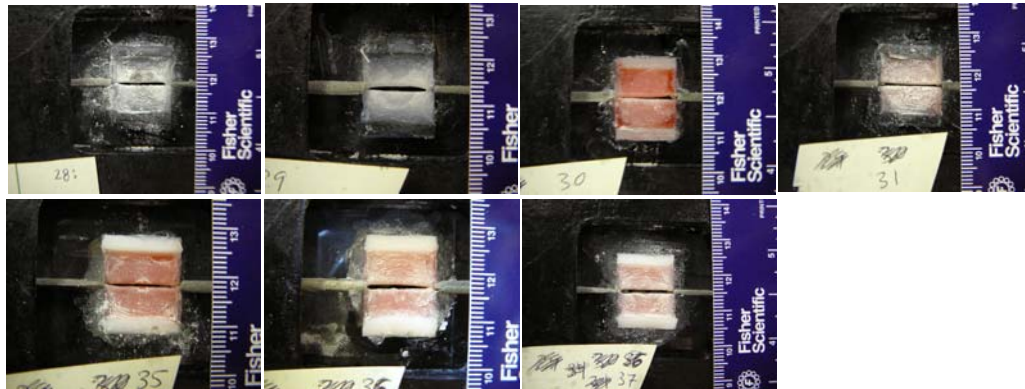
Figure 3-10 Varying glottal area profiles, widths, and calibration points.

Figure 3-10 shows pre-vibratory images of the different models. Table 3-4 lists

the measured glottal widths of each of the models, ordered from smallest to largest. All

glottal widths were less than 1 mm. While the values shown in Table 3-4 are reasonable

for phonation, the real vocal folds have a much larger of range of motion than the

synthetic model used in this research, which is highly idealized.

41

Table 3-4 Measured pre-vibratory glottal widths.

Model	Glottal width (cm)
31	0.033
30	0.040
35	0.041
28	0.074
36	0.082
37	0.087
29	0.096

Figure 3-11 shows the lateral glottal displacement data plotted vs. mean sub-glottal pressure. The one-layer models' (Models 28 and 29) maximum displacement exhibited a linear relationship with sub-glottal pressure. All of the two-layer models showed a curved, rather than a linear, relationship. This was especially pronounced in the stiffest two models (Models 31 and 34). All of the models exhibited similar glottal displacement magnitudes. The one-layer models had higher than average maximum displacements. The fact that Model 28 was driven over a larger range of pressures may partially explain why it showed a larger displacement than the other one-layer model (Model 29).

3.4.4   Model Consistency (Frequency vs. Pressure over Time)

The variability of a synthetic model's oscillatory frequency over time and for varying pressures was tested as follows. The pressure was first increased to PTP. Maintaining this pressure, measurements of frequency and time-averaged flow rate were repeated every five minutes for one hour, after which the flow supply was turned off. This procedure was repeated on three consecutive days. The model was not disturbed in between measurement sets.

On the fourth day, the pressure was increased to just above PTP (about 101% of PTP). After the model had vibrated for five minutes at this pressure, measurements of frequency and time-averaged flow rate were made. The pressure was then increased to a higher level (about 105.5% of PTP), the model was left to run for another five minutes, and measurements were once again made. This cycle of high and low pressure measurements was repeated for one hour.
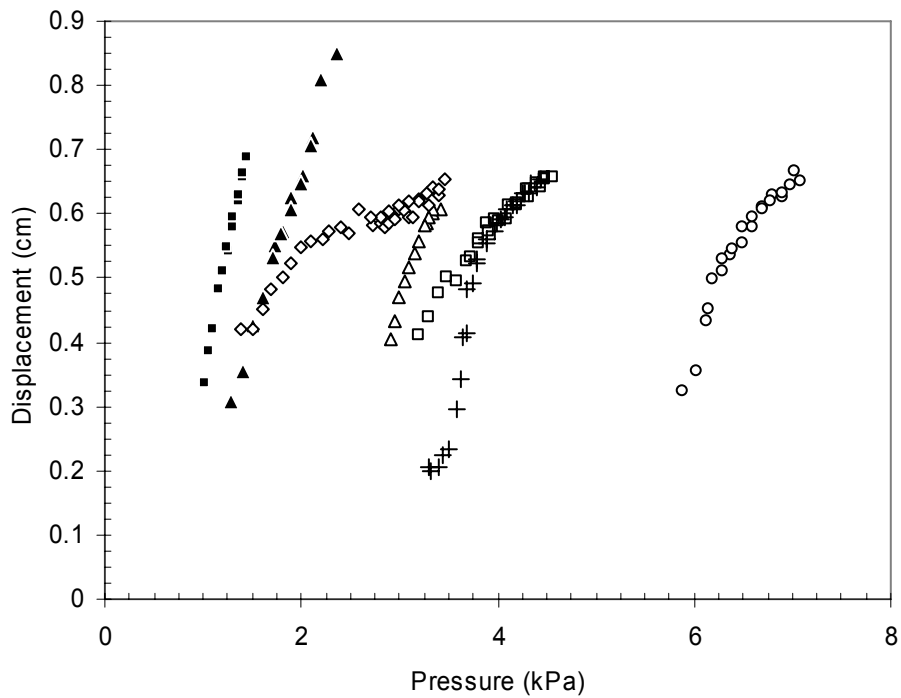
Figure 3-11 Maximum lateral glottal displacement vs. mean sub-glottal pressure. (▲ = Model 28, ■ = Model 29, + = Model 31, ○ = Model 34, □ = Model 35, △ = Model 36, ◇ = Model 37.)

The average frequency for the first three days of measurements was 153.1 Hz, with maximum and minimum measured frequencies of 153.3 and 152.9 Hz, respectively. The average standard deviation of the measured frequency was 0.1 Hz (or less than 0.1% of the mean frequency). Although the pressure was nominally constant, it did fluctuate

43

slightly. The average, maximum, and minimum pressures for the same time period were approximately 4.10, 4.15, and 4.07 kPa, respectively. The average standard deviation of the measured pressure was 0.023 kPa (or 0.56% of the mean pressure).

For the fourth day of testing, in which the same model was subjected to alternating pressures, the average frequencies at low and high pressures were 152.9 and 153.3 Hz, respectively. The average standard deviation of the low pressure frequency was 0.086 Hz (or 0.056% of the average low pressure frequency). The average standard deviation of the high pressure frequency was 0.005 Hz (or 0.0033% of the average high pressure frequency). The standard deviation of the pressure values were 0.33% and 0.46% of the average low and high pressure values, respectively. These values demonstrate good model consistency, particularly given that the model was left to run for one hour continuously on three consecutive days without any flow conditioning. For reference, typically excised larynges are only capable of several minutes of vibration with humidification and other tissue conditioning. It should be noted that sub-glottal acoustic coupling (discussed in more detail in Section 3.4.6) likely contributed to the steady frequency values.

3.4.5   Flow Visualization Experiments

It is generally accepted that the jet that forms at the exit of the glottis during vibration is a significant source of sound (e.g., Kaiser, 1983; Mongeau et al., 1997). Study of the glottal jet has been of increasing interest to vocal fold researchers (e.g., Alipour and Scherer, 1995; Zhang et al., 2002; Zhang et al., 2004). The purpose of the following tests was to visualize the glottal jet and to observe any differences between the different vocal fold models.

44

All of the measurements discussed up to this point used the upstream test system shown in Figure 3-7 (5.7 m tubing and 22.9 cm aluminum duct). For convenience, the upstream system was modified (see Figure 3-12) for the flow visualization tests discussed below. The length of the larger diameter tube, which connected the duct to the smaller diameter tube, was reduced to about 20.3 cm. The total length was about 5.92 m (20.3 cm tube + 5.49 m tube + 22.9 cm aluminum duct). The diameter of the tubes was unchanged. The plenum was not used.
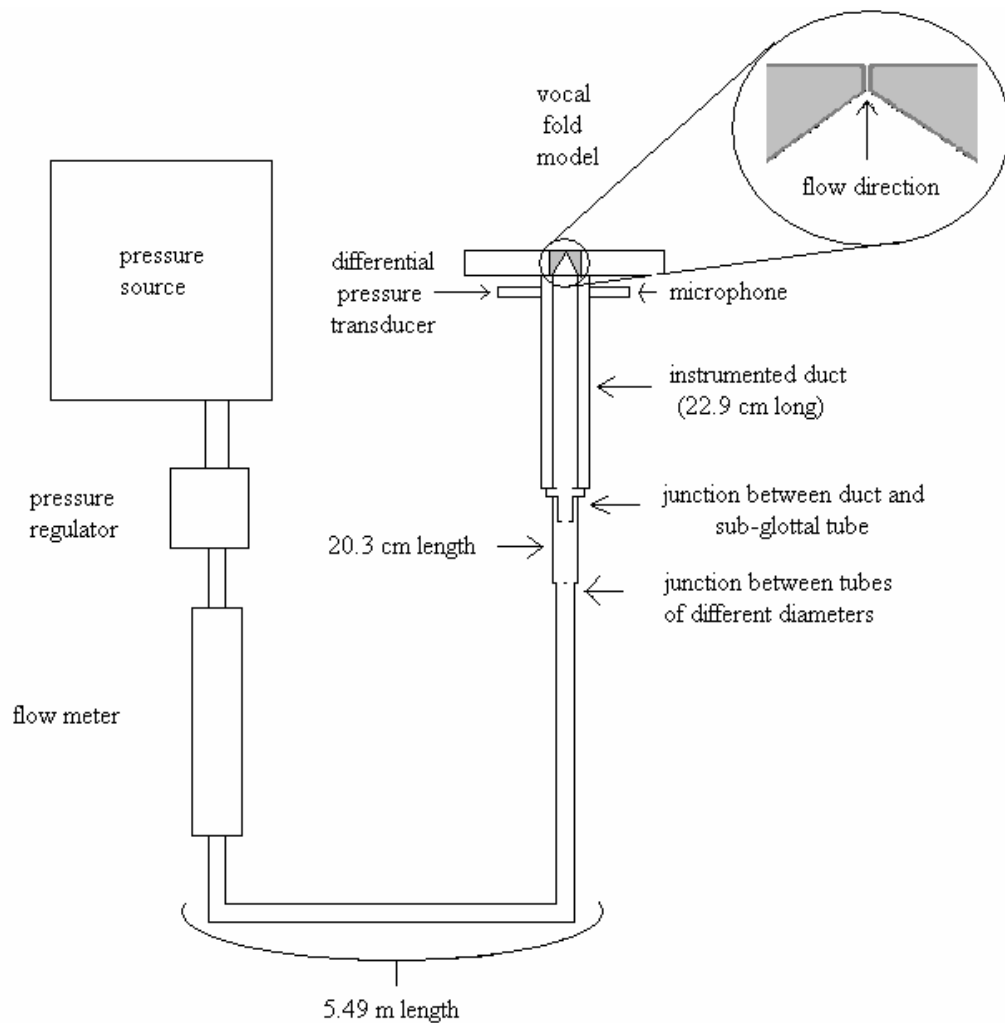
Figure 3-12 Test system used in flow visualization experiments.

Olive oil was used to seed the flow, a strobe light was used for illumination, and a digital video recorder acquired images of the jet from two different perspectives (see Figure 3-13). The model was vibrated near the onset pressure and the jet was imaged. The tests focused on observable features of the glottal jet, including: jet spreading angle and jet skewing.
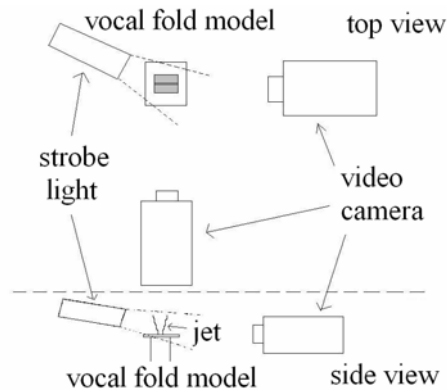
Figure 3-13 Schematic of different views used in flow visualization studies.

For each of the cases, the pressure was increased until the model vibrated. Measurements of frequency and mean sub-glottal pressure were recorded at each of three pressure settings. Simultaneously, the jet was recorded using the video camera. This process was repeated using the three pressures: a pressure close to the onset pressure, one pressure much greater than the onset pressure, and one pressure lower than the onset pressure (but while still vibrating). This was done in an attempt to excite and capture differing modes of vibration.

Using images from the video recorder and calibration images, the jet angle was measured by importing the image into MS Paint, drawing lines parallel to jet features, and measuring the angle between the lines using a protractor. The jet angle was

measured at a phase where divergent jet profile images were evident (e.g., the latter part of the jet cycle, when turbulence is considered to be highest).

Based on observation of the video images, the seven models were classified into one of two categories: symmetric or asymmetric. Note that this is largely qualitative, and improved quantitative jet angle measurements based on velocity profiles are given in Chapter 4.

The left side of Figure 3-14 shows the symmetric-type jet. The synthetic vocal folds, on the right of the left image in Figure 3-14, are approximately symmetric about a horizontal plane, as is the jet. Three of the models included in this study were observed to behave in this manner: 31, 35, and 37.
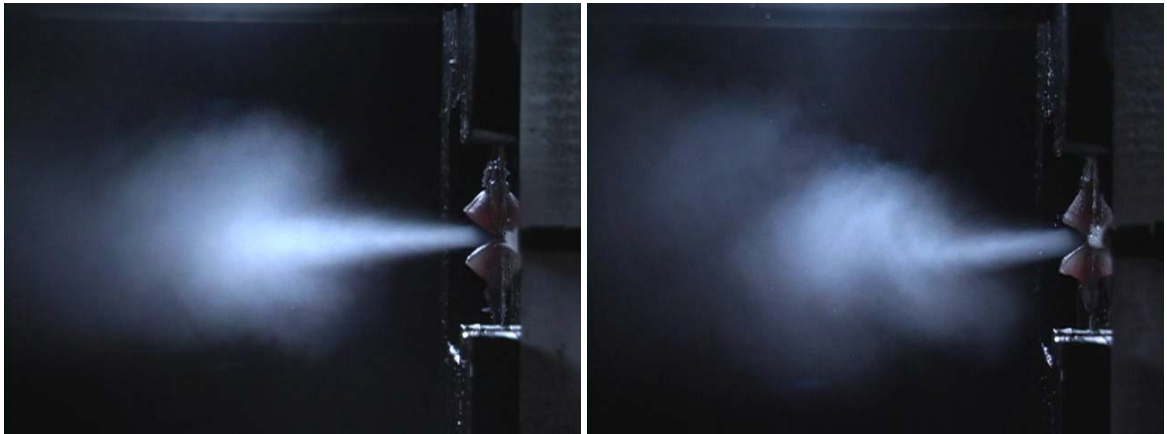
Figure 3-14 Symmetric jet (at left, Model 31) and asymmetric jet (at right, Model 36).

Figure 3-14 also shows the asymmetric-type jet (right image). The synthetic vocal folds are *asymmetric* with respect to the vector normal to the superior-lateral plane. Correspondingly, the visible jet is lop-sided when compared with the symmetric jet (i.e. the jet is angled away from the centerline, the turbulent vortex on the bottom of the image

is closer to the glottis than the corresponding lobe on the opposite side). The remaining four models examined in this study were observed to behave asymmetrically: 28, 29, 30, and 36. Complete cycles of the symmetric and asymmetric case front views are included below in Figure 3-15.
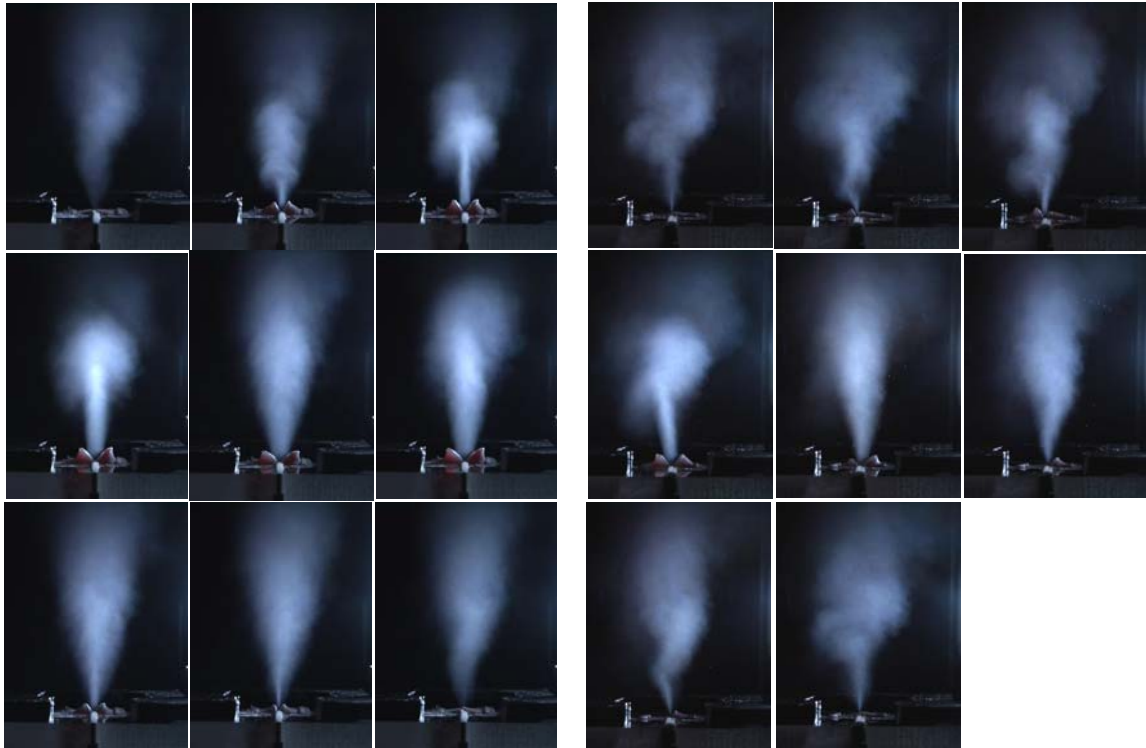
Figure 3-15   Front view of symmetric (Model 35, left) and asymmetric (Model 36, right) jet sequences.   Jet progression proceeds from left to right, top to bottom.

The varying jet angle affects the regions above the glottis that interact with the jet. In an open jet case, such as this, the skewing jet has no physical boundaries with which to interact. However, in the real larynx there exist real tissue boundaries (e.g. the vocal tract and false folds). The changing orientation of the jet, coupled with its interaction with other laryngeal tissue structures, creates the potential for sound generation. Also, the

frequency of jet skewing back and forth can also be a potential contributor to sound generation.

The side view showed little variation with model type, but showed strong dependence on pressure (see Figure 3-16). A cycle of the side view demonstrated prominent jets at the far left and right side of the vocal fold model when it closed, and the seeded air flowed out of the posterior and anterior commissure of the glottis (the view of these features is partially obstructed by a test fixture wing nut located in the center of the frame).

Figure 3-16 Side view of Model 36 for *p* >> PTP.

It should be noted that the posterior commissure is commonly seen in real vocal folds; an anterior commissure is not necessarily physiologically realistic. As the pressure decreased, regardless of whether or not the model was vibrating symmetrically or asymmetrically, the jet issuing from both extreme right and left edges of the glottis disappeared, and the appearance of the jet side view changed very little over the course of a cycle to sound generation.

Figure 3-17 shows the measurements of frequency vs. mean sub-glottal pressure for the flow visualization measurements; it shows an interesting pattern. The symmetrically vibrating models (Models 31, 35, and 37) appear to vibrate relatively independent of sub-glottal pressure.
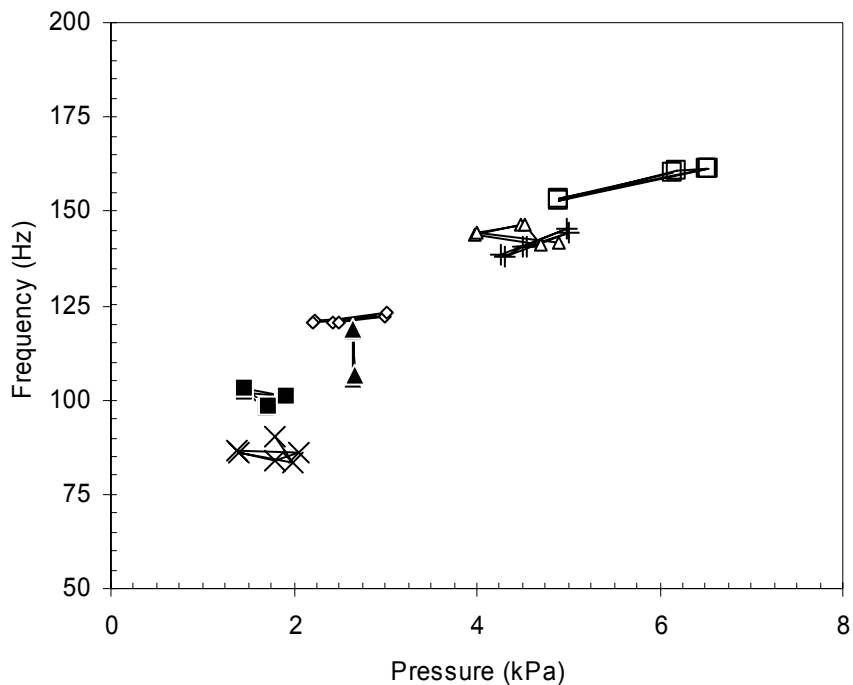
Figure 3-17   Flow visualization measurements of frequency vs. mean sub-glottal pressure for the seven different vocal fold models. (▲ = Model 28, ■ = Model 29, ✕ = Model 30, + = Model 31, □ = Model 35, △ = Model 36, ◇ = Model 37.)

Despite substantial changes in the driving pressure, these models could not be excited into a new mode of vibration. In contrast, the asymmetric models (models 28, 29, 30, and 36) all displayed varying degrees of multiple modes, which appear in the form of frequency jumps. These models appear as triangles or vertical lines in Figure 3-17. Vertical changes correspond to larger changes in frequency for small changes in pressure. Typically, the more chaotic modes vibrated at a lower frequency.

The models identified as asymmetric vibrators in this study can be seen to contain more jumps (or larger increases in frequency for small changes in pressure): Models 28, 29, 30, and 36 all contain curved patterns. An exception to this observation is Model 31 which jumps in Figure 3-17, but is smooth in Figure 3-8. However, Models 35 and 37 are consistently smooth lines.

These observations suggest that a thicker cover on a two-layer model stabilizes the vibration of the model, preventing other, more chaotic modes from being excited. Also, there may be a connection between asymmetric vibration and the potential for mode shifts during vibration.
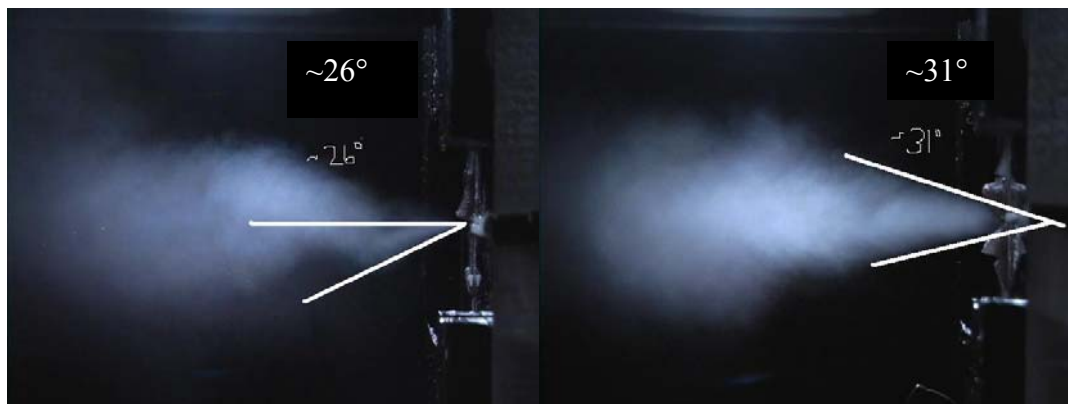
Figure 3-18 Jet centerline angle (left) and jet spreading angle (right).

51

Figure 3-18 shows sample measurements of jet angle. A wide variety of angles was measured. The widest and most uniformly dispersed jets occurred when the glottis took a divergent profile (i.e. at the latter end of the cycle).

Table 3-5 shows the jet spreading angles measured in this study. The angle of some models was remarkably consistent over the range of pressures used, particularly Models 31 and 37, as evidenced by their relatively low standard deviation. Regular deviations can be seen in the behavior of the asymmetric jet. The jet axis fluctuates by as much as $\pm 13°$ about an imaginary centerline jet axis.

Table 3-5 Maximum jet spread angles.

Model	Divergent Angles, (°)	Standard deviation (°)
28	32, 21	8
29	37, 18, 40	12
30	23, 42, 23	11
31	17, 14, 18	2
35	37, 25, 37	7
36	22, 25, 33	6
37	31, 36, 31	3

The jet spreading angle measurements in Table 3-5 supported the differentiation of models 31 and 37. They both showed remarkable consistency of jet angle given relatively large changes in pressure. Model 35, which has otherwise been grouped in with Models 31 and 37, had a higher standard deviation than either 31 or 37, but it was still lower than other angles. Generally, the asymmetrically vibrating models experienced a wide range of jet spreading angles.

Model 30 showed the lowest frequencies in Figure 3-17 (and in Figure 3-8). It is unclear why. However, it was the least stiff two-layer model. The combination of decreased body stiffness and a nominal cover layer may be enough to dramatically affect

the vibratory behavior. Also, Model 30 is the newest model made, and the effects of aging on these particular models are not known.

Generally, these results were effective at visualizing features of the glottal jet. See Section 4.2 for additional jet visualization, and Chapter 5 for recommendations on improvements for future studies.

Asymmetries in vocal fold vibration have been found to be correlated with the excitation of different modes of vibration. Also, the jet angle varies more when the model vibrates asymmetrically, which, in the real vocal folds, would direct the jet away from the channel centerline and towards the wall of the supra-glottis and the false vocal folds. Two-layer models, with a relatively thick cover layer, may be less prone to excitation of multiple modes.

3.4.6   Influence of Sub-Glottal Duct on Model Vibration

The sub-glottal system is always present in measurements of vocal fold behavior, and the degree to which this system influences the model vibration has generated recent interest (Zhang et al., 2006a, 2006b). The influence of the upstream length on model vibration was the subject of the next two series of tests; Figure 3-19 shows the test system used.

In order to assess the dependence of model vibration on sub-glottal resonances, measurements of frequency vs. mean sub-glottal pressure were repeated over a range of sub-glottal tube lengths. A strong dependence would indicate acoustic coupling between the vibrating model and the upstream system; relative independence of model vibration from the upstream system is often considered more desirable in phonation (Zhang et al., 2006a, 2006b) because it is less prone to frequency jumps.

53
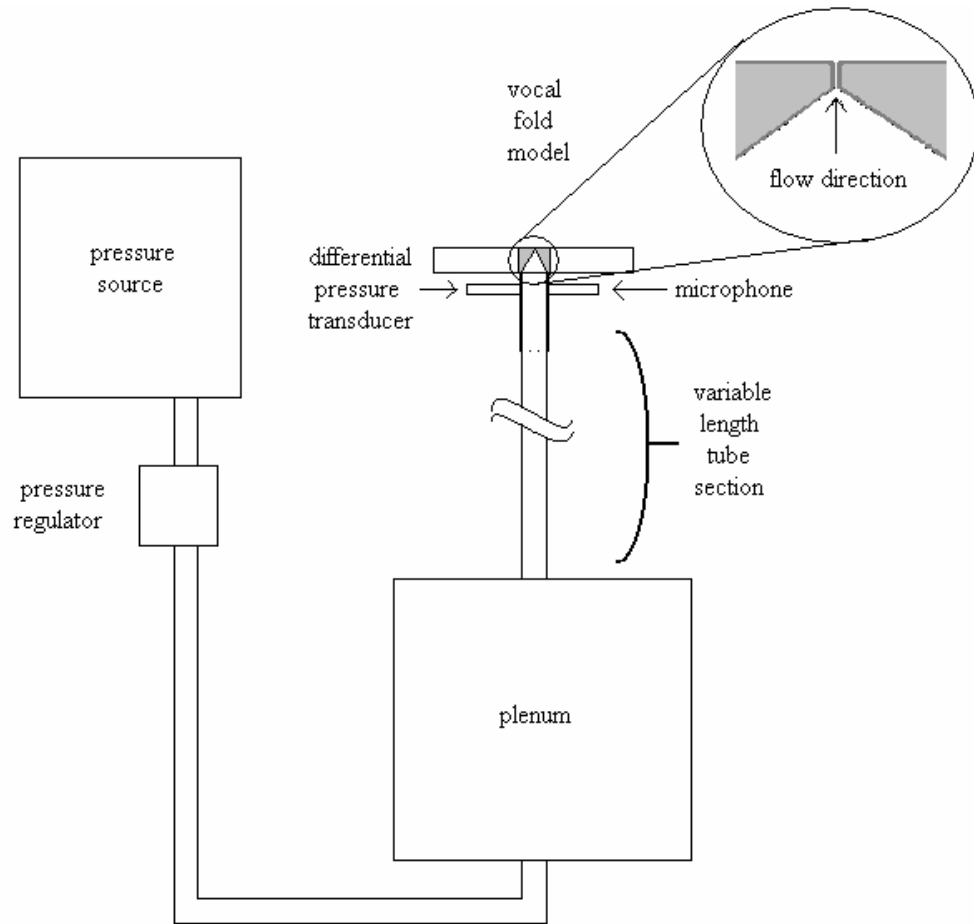
Figure 3-19 Upstream test system C (final system).

As mentioned earlier, the sub-glottal system was redesigned to maintain a near
constant cross-sectional area of 5 cm^2. The upstream aluminum duct was replaced with a
shorter cylindrical section of rigid PVC pipe. The flexible PVC tubing was replaced with
a series of variable length sections capable of producing tube lengths ranging from 17 cm
to more than 320 cm. The plenum was added to the system to approximate an anechoic
termination. The plenum was placed between the flow source and the vocal fold model.
The flow meter was removed from the measurement system. The variable length sub-
glottal tube system (discussed in Section 3.2.3), including the plenum, was consistent

54

with design parameters used in similar experiments (Zhang et al., 2006 a, 2006b), which assumes an ideal open-ended termination to the sub-glottal tube system.

Initially, the shortest length tube was inserted and the pressure was increased until the model began to vibrate. The PTP, tube length, time-averaged sub-glottal pressure, and frequency values were recorded. The tube length was then increased by a small amount (approximately 5 cm), and the measurements were repeated. These measurements were performed for the full range of tube lengths (32 cm to 320 cm). In a second experiment, these measurements were repeated but for a reduced set of tube lengths (32 cm to 162 cm) and for several different pressures at each tube length. Each of these tests was performed using several different models.

The acoustic resonances were predicted based on an ideal open-ended tube (see Figure 3-20), in which the pressure is a maximum at one end and zero (gage pressure) at the other.
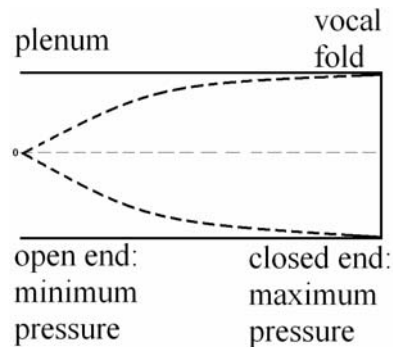
Figure 3-20 Illustration of an ideal, open-ended tube pressure profile (in bold dashed line).

An estimate of the sub-glottal resonance frequencies can be obtained from the following formula for standing waves in open-ended tubes:

$$f = \frac{nc}{4\lambda}$$

(3.2)

where c is the speed of sound in the fluid (for air, ~343 m/s), and λ is the wavelength (i.e. the length of the tube in meters), and n consists of odd integer values (Fishbane et al., 1993).

Figure 3-21 shows the results of the variable tube length tests for one- and two-layer models. Also shown are the predicted tube frequencies. Both types of models generally follow the predicted sub-glottal resonances. There does appear to be a degree of independence from the sub-glottal system at certain tracheal lengths for both one- and two-layer models: the two-layer model with the thickest cover layer (Model 37, cover = 2 mm) deviated from the predicted curves between lengths 100 to 125 cm, and the one-layer model (Model 28) deviated from the predictions from 30 to 50 cm. It is presumed that position of the model vibration on different resonance curves represents different modes of vibration; certain ranges of tracheal lengths were transitional lengths where the models "switched" between adjacent curves (e.g. 75 through 125 cm). In this manner, very different frequencies could be obtained from the same vocal fold model – frequencies could vary by as much as 90 Hz at these transitional lengths.
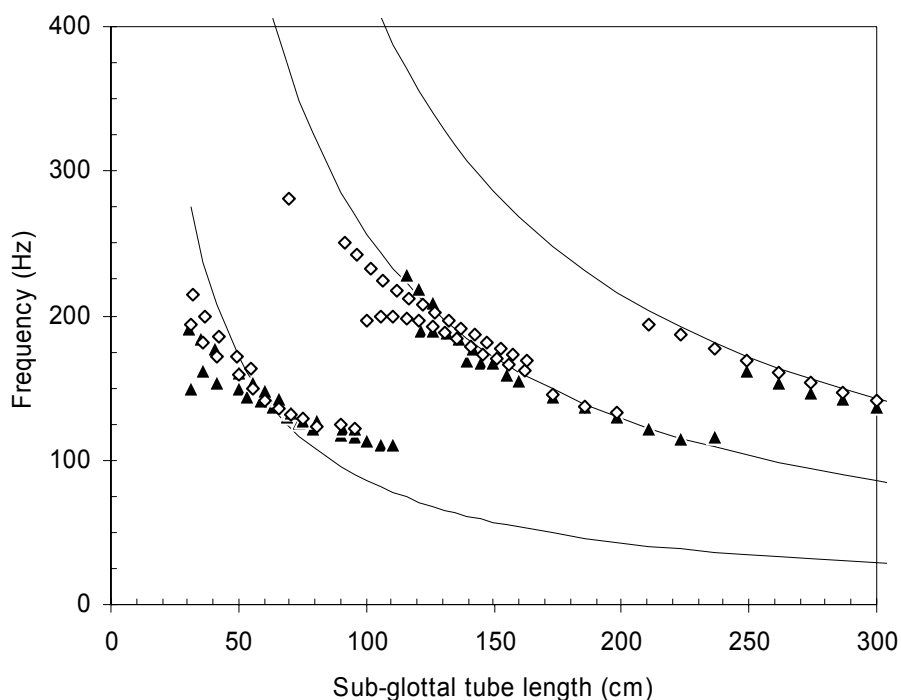
Figure 3-21 Original variable tube length tests at mean sub-glottal PTP. (▲ = one-layer model, ◇ = two-layer model, ─ = predicted).

The addition of fibers to the vocal fold models had an interesting effect. For two of the fiber types (cross-woven rayon poly and short, overlapping cotton), no change was evident. However, acrylic fibers (which are slightly "curled") that roughly spanned the anterior-posterior length of the vocal fold model caused the model to exhibit an increased independence from the sub-glottal resonances. This can be seen in Figure 3-22. The pressure was set to PTP, which varied according to sub-glottal tube length and model: 2 to 5.5 kPa (one-layer rayon model, Model 3), 4.6 to 8.4 kPa (one-layer cotton model, Model 10), and 0.6 to 2.2 kPa (two-layer acrylic model, M1).

When the pressure was increased above the onset pressure, the independence of the acrylic fiber model continued to increase, as seen in Figure 3-23.

57
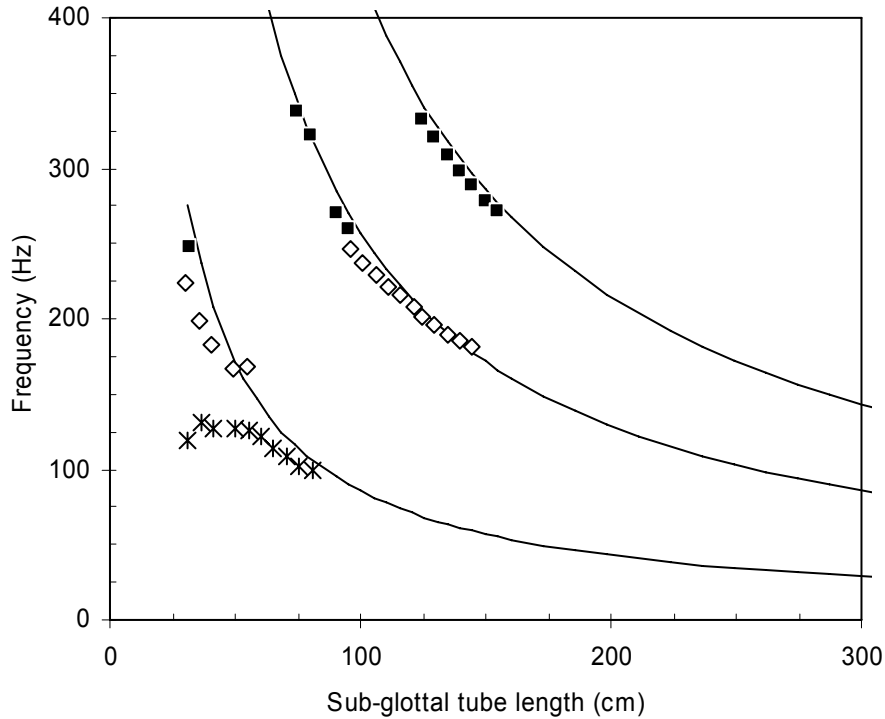
Figure 3-22 **Variable tube test for models with fibers in silicone matrix at PTP. (■ = short, overlapping cotton fibers in one-layer model, ◇ = rayon-poly weave in one-layer model, ∗ = long acrylic fibers in two-layer model).**

The pressure again varied with sub-glottal tube length and model: 3.6 to 6 kPa (one-layer model, Model 28), 3.2 to 5.3 kPa (two-layer model, Model 37), and 1.5 to 3 kPa (two-layer acrylic model, M1).

Figure 3-23 shows the model vibrating with relative independence of the tube length. This behavior was observed at pressures much higher than onset pressure (typically > 2 kPa vs. onset at less than 1 kPa). The acrylic model displayed this behavior, and the difference between its behavior and the other models tested is attributed to the presence of acrylic fibers in its body layer. These fibers are naturally curled. As the pressure increases, the fibers are uncurled and stretched, creating a non-linear increase in stiffness.
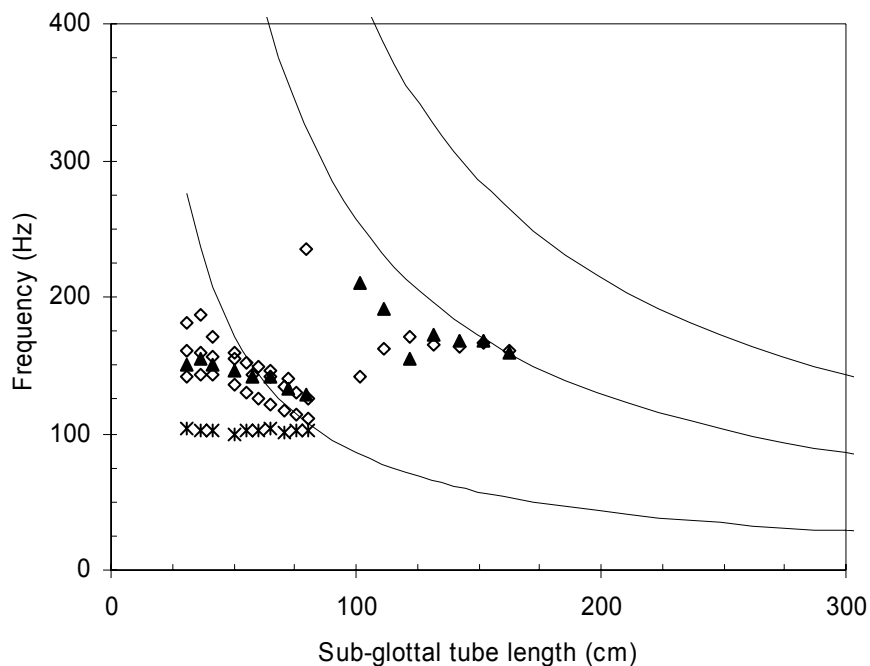
Figure 3-23 Variable tube test for models with fibers in silicone matrix at p > PTP. (▲ = one-layer model, ◇ = two-layer model, ✳ = two-layer model with fibers).

Figure 3-24 shows the frequency vs. pressure relationship for the two-layer acrylic model, which appeared to vibrate independently from sub-glottal tube length in Figure 3-23. The curves shown in Figure 3-24 correspond to frequency vs. sub-glottal pressure relationships for different sub-glottal lengths. As the pressure increased, the frequencies converged on a value close to 100 Hz as the length of the sub-glottal tract was varied. For certain lengths, there were large changes in frequency as pressure was varied. However, by the time the lengths reached 65 – 80 cm, the range of frequencies decrease, and the model entrained itself with what was apparently the dominating vibrational influence (the sub-glottal resonance).
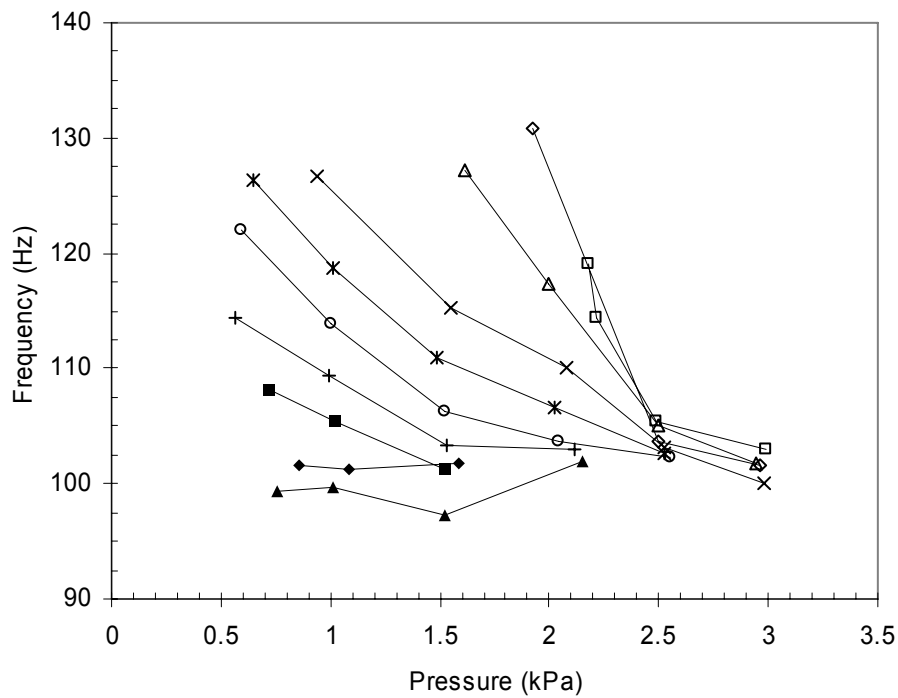
Figure 3-24 Frequency vs. pressure plotted for model M1 at the different lengths tested. (□ = 31.1 cm, ◇ = 36.2 cm, △ = 41.3 cm, × = 50.2 cm, ✳ = 55.2 cm, O = 60.3 cm, + = 65.4 cm, ■ = 70.5 cm, ● = 75.6 cm, ▲ = 80.6 cm).

At the shorter tracheal lengths, the model vibrated independently of the sub-glottal tube resonances. Real human tracheal lengths are much shorter than the 80 cm length at which the model seemed to fully align itself with the sub-glottal resonances. Therefore, the M1 model appears to offer promising independence from sub-glottal resonances at more realistic sub-glottal tube lengths.

The relationship between mean sub-glottal pressure and sub-glottal tube length is shown in Figure 3-25. The mean sub-glottal pressure required to induce vibration changes according to the sub-glottal tube length. While the particular pressure value changes according to the vocal fold model, the point at which the lowest PTP is found is

quite consistent. The results in Figure 3-25 are similar to those published in Zhang et al.

(2006a), which also used a one-layer version of this synthetic model.
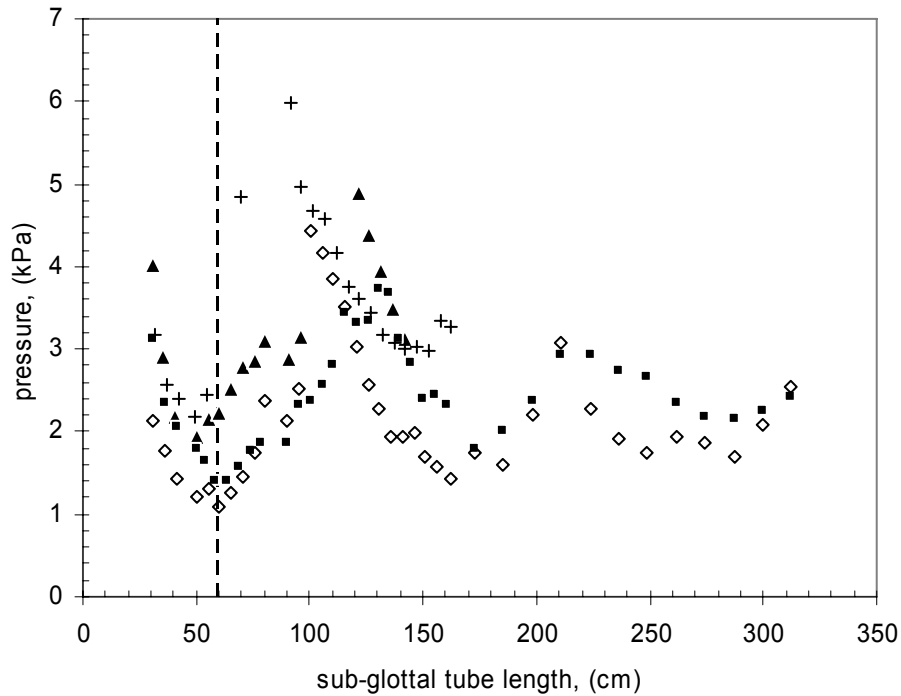
Figure 3-25   Relationship between mean sub-glottal pressure and sub-glottal tube length.   The dashed line at ~ 60 cm indicates the lowest PTP attainable for these experiments. (▲ = Model 28, ■ = Model 29, + = Model 31, ◇ = Model 37).

3.5   Summary

The frequency and pressure measurements contained in Chapter 3 show that

models with different material properties and geometries (e.g. cover layer thickness)

vibrated at different frequencies and required different onset pressures.   One model

(Model 34) displayed a PTP that was perhaps twice what would reasonably be expected

in normal human phonation. Three others (Models 31, 35, and 36) phonated at marginal

pressures. The remaining four models (Models 28, 29, 30, and 37) phonated at pressures consistent with human phonation. All of the models vibrated at frequencies consistent with human phonation. Frequency of vibration can be controlled by the selection of model mixing ratio and sub-glottal tube length.

The average flow rates required for the onset of phonation were higher than those seen in human speech. These high flow rates were attributed to several potential causes: oscillation patterns which differ from real vocal fold behavior (including larger than normal lateral glottal displacements) and higher than normal prephonatory glottal gaps.

Measured model consistency was good, varying by less than 1% over time and over varying driving pressures. However, part of the model's consistent frequency could be attributable to coupling with the sub-glottal acoustics (which can be complex, and are beyond the scope of this thesis). While the upstream system (shown in Figure 3-7) tube length was selected to be very long (in an attempt to minimize such acoustic interactions), additional tests should be performed to verify the results of this thesis. As testing progressed, additional models were manufactured; model PTP and accompanying flow rate values were lower, improving the models' match with real vocal fold physiology (see Section 4.4.1 for reporting of these improved synthetic vocal fold parameter values).

The two-layer synthetic model with the thickest cover (Model 37, see Table 3-3) did appear to vibrate over a relatively larger range of frequencies and pressures than did the other models. Model 30, which had a more compliant body layer than all other two-layer models, showed the lowest measured frequencies and pressures, even lower than the more compliant one-layer models (Models 28 and 29). This could be due to the inclusion

of the cover layer. Finally, the maximum lateral glottal gap of two-layer models during phonation showed less of a change with pressure at the beginning and end of the range of pressures tested, but a sharp increase in the amount of displacement in between, which resulted in a non-linear appearance. Both one-layer models tested displayed a linear relationship between maximum lateral glottal gap and mean sub-glottal pressure.

The results of the flow visualization experiments suggested a relationship between the excitation of multiple vibratory modes and glottal asymmetries. It was postulated that two-layer models may be less prone to the excitation of multiple modes of vibration, though further study is needed. The glottal jet of the different synthetic models was categorized as either symmetric or asymmetric. However, attempts to correlate model material properties and geometry with the degree of symmetry in the glottal jet were also inconclusive.

The importance of sub-glottal acoustics to model vibration was re-iterated. Previous studies (Zhang et al., 2006a, 2006b) had shown that the one-layer model frequency of vibration was dependent on sub-glottal tube length, unless the majority of each vocal fold was restrained in the superior direction. The new experiments in this thesis found that two-layer models also demonstrated a general dependence on sub-glottal acoustics for frequency of vibration. At certain sub-glottal tube lengths, both one- and two-layer models separately showed signs of potential independence from sub-glottal acoustics. The combination of pressures greater than PTP and the addition of acrylic fibers to a two-layer model (Model M1, see Table 3-3) resulted in model vibration independent of sub-glottal tube length. Further studies are necessary to see if the right combination of a stiff (i.e. restrained) body layer and a compliant cover layer can be

found for a two-layer model which will enable it to behave as Zhang's (Zhang et al, 2006b) restrained one-layer model did. Also, the effect of adding materials that demonstrate non-linear stress-strain behavior (e.g., acrylic fibers) to the synthetic model should be further explored.

4   Glottal Jet Measurements using PIV and High-Speed Flow Visualization

This chapter begins with a brief description of the importance of the glottal jet in speech production.   The experimental setups used in obtaining qualitative and quantitative flow measurements using a two-layer synthetic vocal fold model are then described. Specifically, the glottal jet evolution was visualized from various perspectives using high-speed imaging. Also, the glottal jet centerline was located and the average and RMS velocity fields were calculated using particle image velocimetry (PIV). The results of these measurements are finally presented and discussed.

4.1   Importance of the Glottal Jet in Speech Production

The glottal jet has been the subject of many vocal fold studies (see Chapter 2 for examples). As the vocal folds cyclically open and close, an orifice-modulated jet is formed. This time-varying glottal jet is the primary source of sound in speech. A better understanding of the glottal jet and its interactions with the surrounding tissues will yield insights into the complexity of the glottal sound source. For instance, it is known that the time-varying pressure fluctuations originating from vocal fold vibration is the main contributor to the glottal sound source. Less well understood are secondary sound sources such as the interaction between the glottal jet and supra-glottal boundaries (e.g.

vocal tract wall, false folds). Observation of the physical characteristics of the glottal jet can also lead to insight into general vocal fold behavior and can help improve analytical and computational vocal fold vibration models.

Most vocal fold studies of glottal jet velocity have used hot-wire anemometry (a point-wise measurement technique). A few recent studies have used PIV (Khosla et al., 2007; Erath and Plesniak 2006a, b, c; Neubauer et al., 2007; see Chapter 2 literature review), but none of these have considered the presence of the vocal tract with and without the false folds. The PIV research presented here includes these boundaries.

4.2   High-Speed Imaging

High-speed images of the vocal folds and of the glottal jet were acquired using a Photron FASTCAM-APX RS high-speed camera system.   The resolution varied depending on the view of interest. Three views were imaged, with resolutions as follows: 640×448 pixels (for top view of the vocal fold motion, described below), 896×624 pixels (flow visualization, side view), and 768×784 (flow visualization, front view), with corresponding frame rates of 10,000, 5,000, and 5,000 frames per second (fps), respectively.   High-intensity white LEDs (Visual Instrumentation Corporation, single-LED array, model #200800, controller model #200900) were used in a forward-scattering mode for jet illumination; LEDs were used to minimize heating of the vocal folds. The flow was seeded using a LaVision Aerosol Generator and DEHS oil (see Section 4.4.2 for oil details).
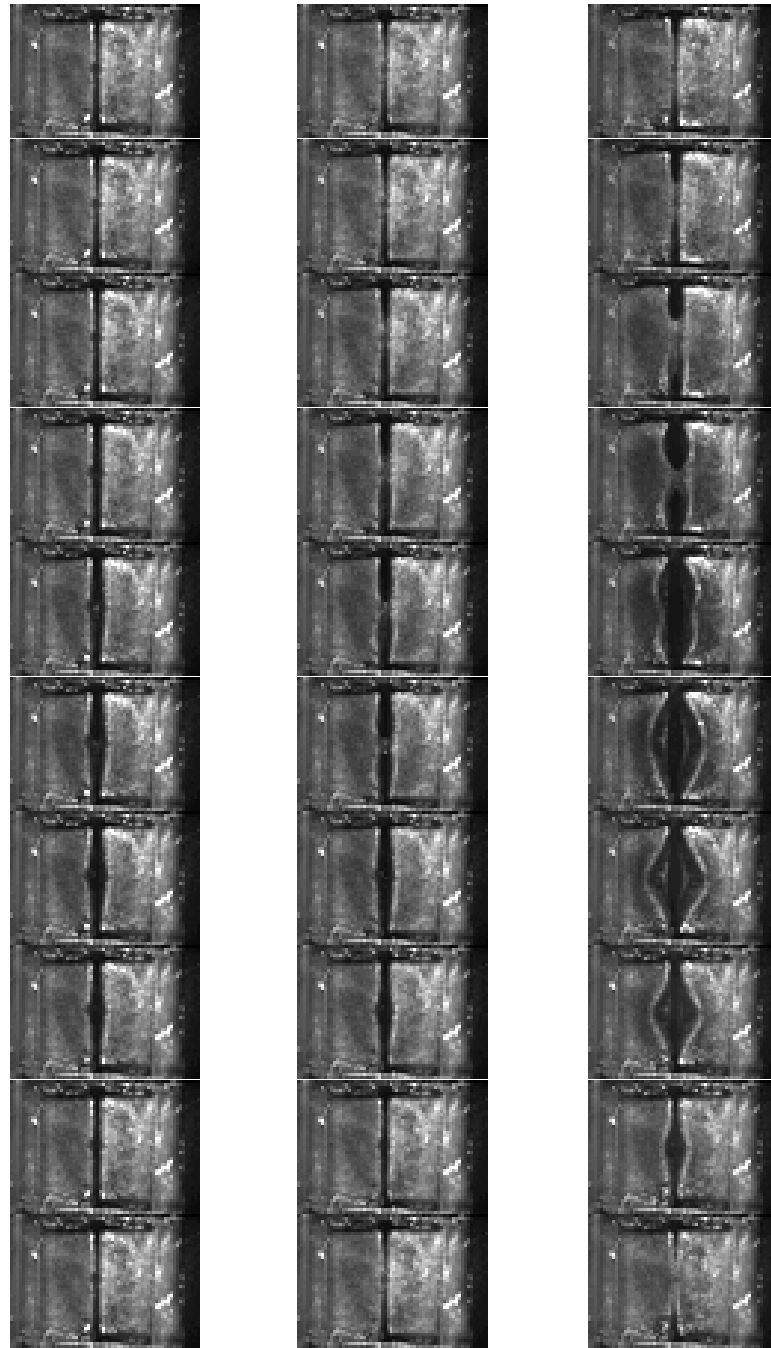
Figure 4-1 Top view of high-speed images of synthetic vocal fold model at 1.25 kPa (left), 1.5 kPa (center), and 1.9 kPa (right) mean sub-glottal pressure.

Figure 4-1 shows one cycle of a top view of the model vibration at three different

sub-glottal pressures. One two-layer model (labeled as M10; see Table 3-3) was used for

the flow experiments discussed in this chapter. The model was placed in the test fixture and not moved for the duration of the high-speed imaging measurements. Test Fixture B (discussed in Section 3.2.2) was used, with the mid-region of the medial surfaces of the vocal folds just touching.

A condition similar to the presence of a glottal posterior commissure can be seen at the top of each individual image in Figure 4-1 where the vocal folds did not completely collide. This resulted in a continuous jet emerging through this open region, as can be seen at the far left side of the side-view images in Figure 4-2.

The superior-inferior motion of the vocal folds at $p =1.25$ kPa was extremely small, and from Figure 4-1 it would appear that the entire glottis never fully opened. The side view of the glottal jet flow visualization in Figure 4-2 supports this observation. This behavior was caused by adhesion between the medial vocal fold surfaces resulting from surface tackiness. Similar adhesion is also evident in Figure 4-1 for the higher pressures, but the glottis fully opened in these cases. The glottal orifice first divided into two separate areas – anterior and posterior – during glottal opening for $p = 1.5$ and 1.9 kPa.

As a result of the collision and adhesion between the medial surfaces of the vocal fold models, it is possible that additional lateral excursion is created in the superior-coronal plane, acting the way a stretched rubber band might recoil. This motion could influence the glottal jet formation and evolution. The adhesion did not appear to extend far inferiorly. Even though collision between the model surfaces may have occurred over the majority of the medial surface, the lateral excursion just mentioned may only affect the extreme superior-medial edge. Experience with using these models agrees with this

view – damage to these synthetic vocal fold models nearly always occurred at the junction of the medial-sagittal and medial-coronal planes, or the point of greatest lateral displacement.
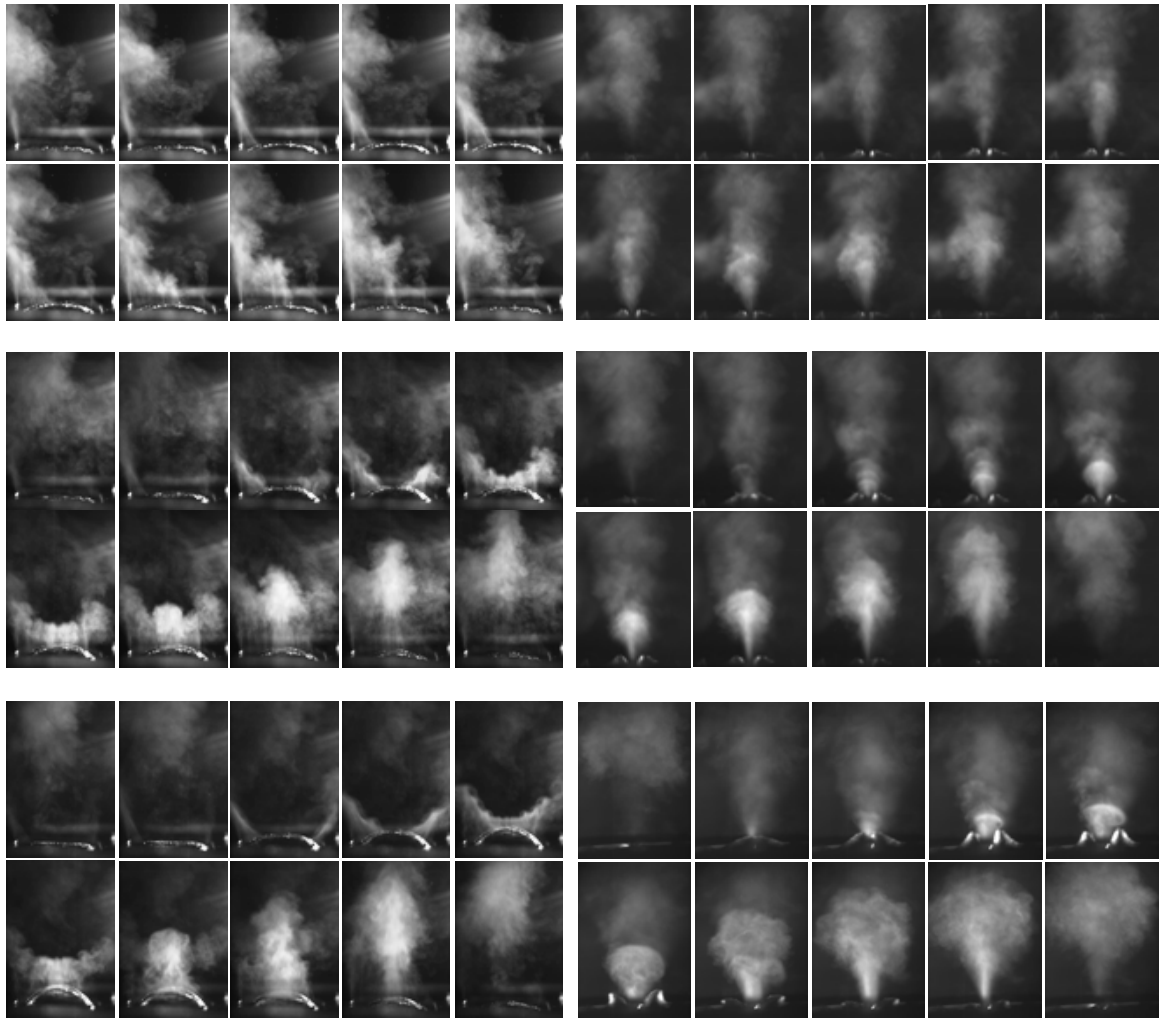
Figure 4-2 Side view (left columns) and front view (right columns) of high-speed flow visualization at sub-glottal pressures of 1.25 kPa (top), 1.5 kPa (center), and 1.9 kPa (bottom). Note that the side and front views were not obtained simultaneously and are only approximately phase-referenced.

A fairly coherent starting vortex is apparent at the two higher pressures (1.5 and 1.9 kPa). The starting vortex and the lateral motion both occur in the early part of the

cycle. The adhesion facilitates rapid lateral acceleration at the vocal fold midplane, which may in turn contribute to the impulsive development of the vortex. This vortex may contribute to the overall sound field. The jets visualized at all three pressures were roughly symmetric in the medial-lateral sense. Also of interest is the double-jet formation during glottal opening, followed by subsequent merging into a single jet, at the two higher pressures (Figure 4-2, side view).

4.3   Particle Image Velocimetry

Particle image velocimetry (PIV) is a flow velocity measurement technique capable of generating spatially resolved two- and three-dimensional quantitative velocity data. PIV requires neutrally buoyant seed particles immersed in the flow of interest, an imaging device, and an illumination source (visualized in Figure 4-3). The camera captures images of the illuminated seed particles; the illumination source is typically a laser sheet.

For the present research, two-dimensional PIV was used, employing the double-image/cross-correlation method (see www.lavision.de for more details), in which the camera captured two successive images separated by time dt. Cross-correlation was used to determine the direction and magnitude of the velocity of the seed particles. PIV assumes that the seed particles have negligible inertia with respect to the flow momentum and that the particles are primarily moving in the plane of the illumination source; this was satisfactorily verified for these experiments (see Appendix C). Compared to other velocity measurement techniques, PIV is relatively non-intrusive, is easily calibrated, and yields a significant quantity of flow information.
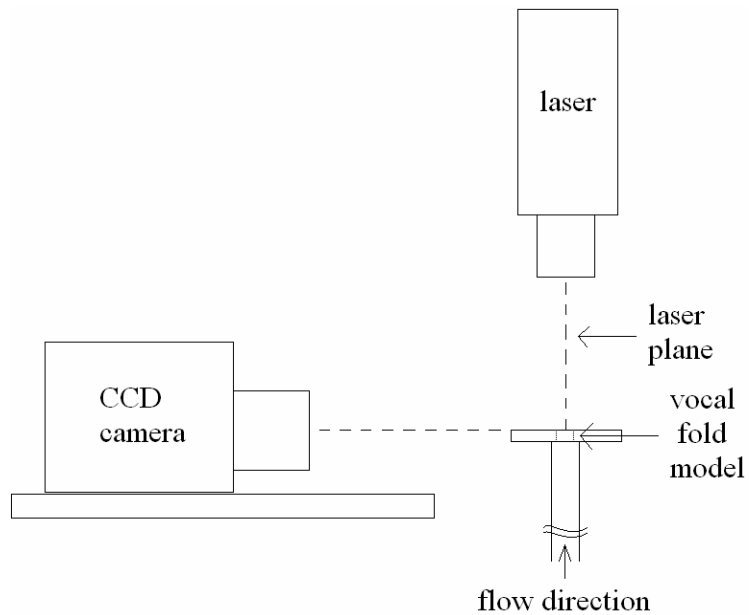
Figure 4-3 PIV system setup. The laser plane extends normal to the page.

4.4   PIV Methods

The following section describes the PIV test setup and the vocal fold model used in testing.

4.4.1   Model and Test Setup

The same two-layer model and test fixture were used for the PIV experiments as was used in the high-speed imaging work (M1, see Table 3-3). As seen previously in the high-speed images, the folds did not completely close, particularly at one end.   The average model vibration frequency during all PIV measurements was measured to be 132 Hz (standard deviation of 0.8 Hz) over the range of sub-glottal pressures of 1.25 kPa to 1.9 kPa. Time-averaged flow-rate was measured to be 103, 149.5, and 232.3 ml/s for sub-glottal pressures 1.25 (±0.57), 1.5 (±0.95), and 1.9 (±1.63) kPa, respectively.   The

fluctuating pressure just listed (in parentheses) varied sinusoidally for the two lower pressures; the waveform of the highest pressure was slightly more complex.

A 60 cm sub-glottal tube was used for these tests; this length was selected based on the data shown in Figure 3-25 to achieve a low model onset pressure. As in previous measurements, a differential pressure transducer was placed approximately 3 cm upstream of the glottis. This signal provided frequency information for triggering the PIV system.

The vocal tract was manufactured from 1.25 cm thick aluminum on three sides, with the fourth wall made of 0.32 cm thick glass (for optical access to the inside of the vocal tract). It measured 30.5 cm in length and had a square cross-sectional area of 5 cm^2 (same as that of the sub-glottal system). Drawings of the vocal tract can be found in Appendix A. The vocal tract was centered on top of the vocal fold model. A plastic-laminated grid placed near the assembled vocal fold model & vocal tract connection was used for lateral positioning of the vocal tract.

A portion of the PIV work included measurements with the false folds positioned in the vocal tract. A model of the false vocal folds was manufactured out of clear acrylic according to the mean values for an adult male reported in Agarwal et al. (2003); see Figure 4-4. The horizontal gap between the false folds was 0.63 cm; the height of the vertical gap between the top of the (non-vibrating) vocal folds and the bottom of the false folds was 0.5 cm. A schematic of the false folds themselves, manufactured according to the dimensions given in Agarwal et al. (2003), is provided in Appendix A. The false folds were polished to improve transmission of the laser sheet into the space between the vocal folds and false folds.
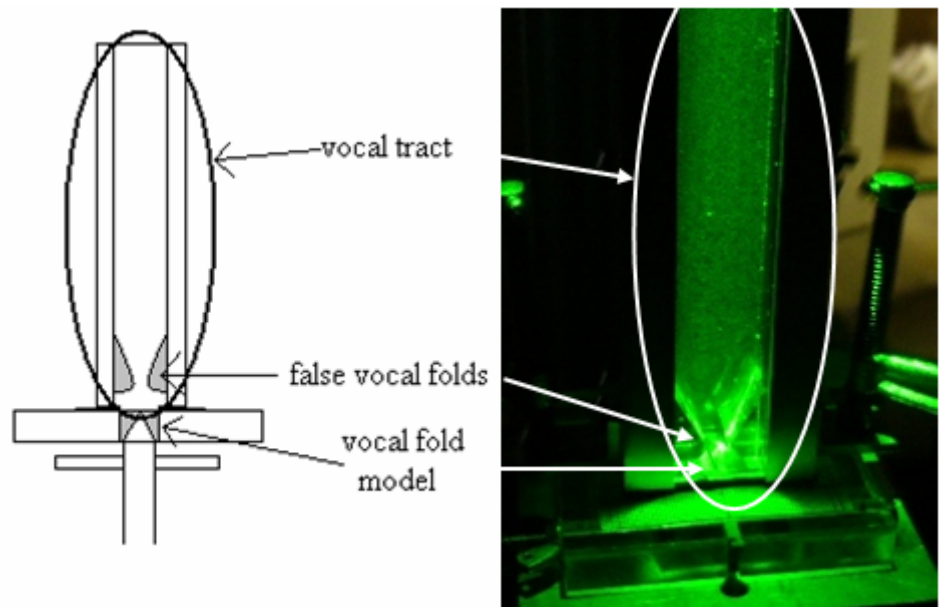
Figure 4-4 False folds positioned in vocal tract of Test Fixture B (shown with PIV laser illumination and seed particles).
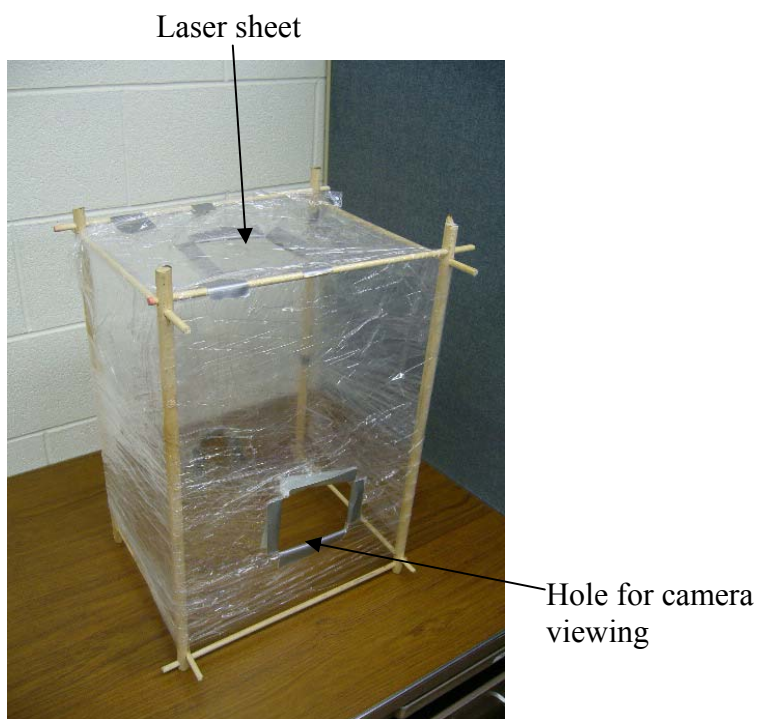
Figure 4-5 Shroud used to create a more uniform seed density for open jet PIV measurements.

A 32 cm × 40 cm × 57 cm shroud was used with the open jet configuration to increase seed particle density in the regions around the jet and thus enable velocity vector calculation (see Figure 4-5).

Three different supra-glottal configurations were tested, including an open jet (no vocal tract), with a vocal tract but without false folds, and with a vocal tract and false folds. These cases are shown in Figure 4-6.

For the vocal tract without false folds configuration, five different cases were studied: one with the duct centered over the vocal folds (symmetric case), and four positions in which the vocal tract was laterally offset from the vocal fold medial-sagittal plane (±1.5 mm and ±4 mm asymmetric cases). For the vocal tract with false folds, three cases were studied: one with the duct centered over the vocal folds (symmetric case), and two positions in which the vocal tract was laterally offset from the vocal fold medial-sagittal plane (±1.5 mm asymmetric cases). These configurations and cases were tested for the same three mean sub-glottal pressures as were used in the high-speed imaging experiments (1.25, 1.5, and 1.9 kPa).
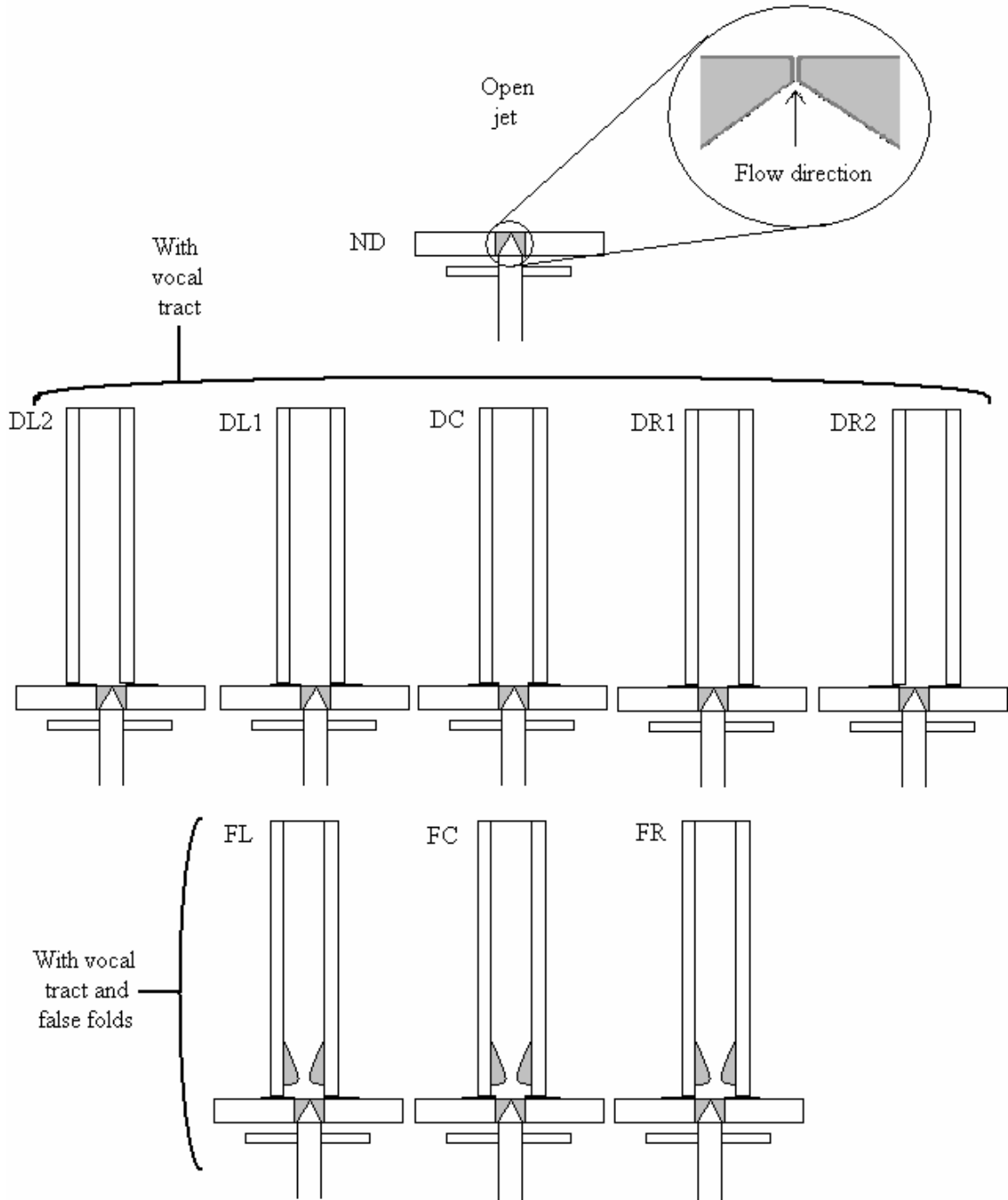
Figure 4-6 Different test arrangements for PIV measurements. ND denotes the no duct, or open jet, case. DL2 and DR2 denote the extreme left and right vocal tract offset cases (±4mm) without the false folds, respectively. DL1 and DR1 denote the left and right offset cases (±1.5mm), respectively, and DC denotes the symmetrically positioned vocal tract case, all without the false folds. FL, FC, and FR denote cases with false folds and the vocal tract positioned to the left (-1.5mm), center, and right (+1.5mm), respectively, relative to the vocal folds.

As mentioned earlier, one wall of the vocal tract was made of glass. This presented a potential problem when seed particles were introduced to the airflow. If either the seed density or the driving pressure were sufficiently high, oil would accumulate on the glass, inhibiting imaging. DEHS oil (see Section 4.4.2) replaced olive oil as the seed particle due to the fact that it accumulated less on the glass. Generally, as the pressure increased, the seed density could be reduced to minimize oil accumulation. However, oil accumulation persisted at the highest pressure used in this study (1.9 kPa), resulting in fewer images acquired.

Seed density was critical to enabling the acquisition of satisfactory PIV images. Seed density was controlled using two different valves (see Figure 4-7). The first was placed before the aerosol generator and controlled the initial amount of pressurized air from the pressure source which entered the aerosol generator. The second valve was placed between the aerosol generator and the plenum and controlled the amount of seeded air that reached the plenum. In order to substantially increase the seed density without increasing the pressure at the vocal fold model, the first valve was completely opened, the source pressure control valve was opened to increase the amount of flow going through the aerosol generator, and the second valve was also opened to bleed off the majority of the pressure upstream of the plenum. For flows that required relatively low seed density (e.g. high pressure measurements, or any measurement using the vocal tract), the second valve was closed and the first valve was carefully adjusted until the optimal seed density was reached. Figure 4-8 shows a sample PIV image obtained after adjusting seed density.
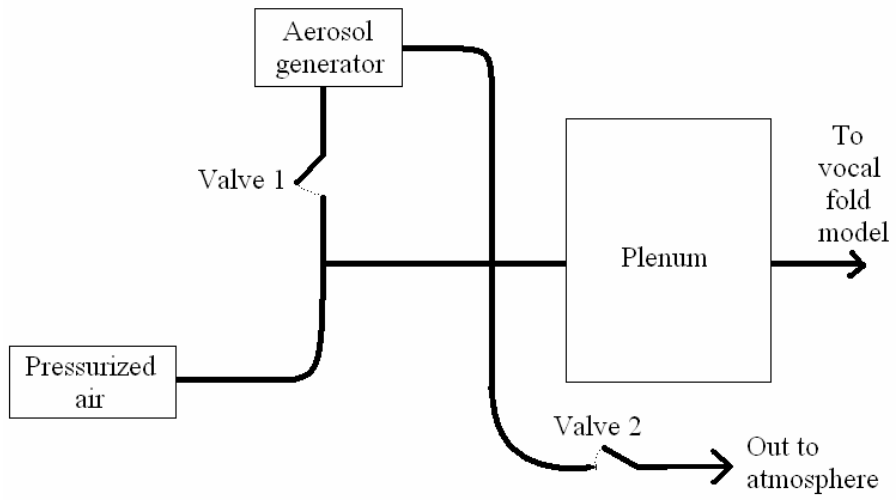
Figure 4-7 Seed density control network.
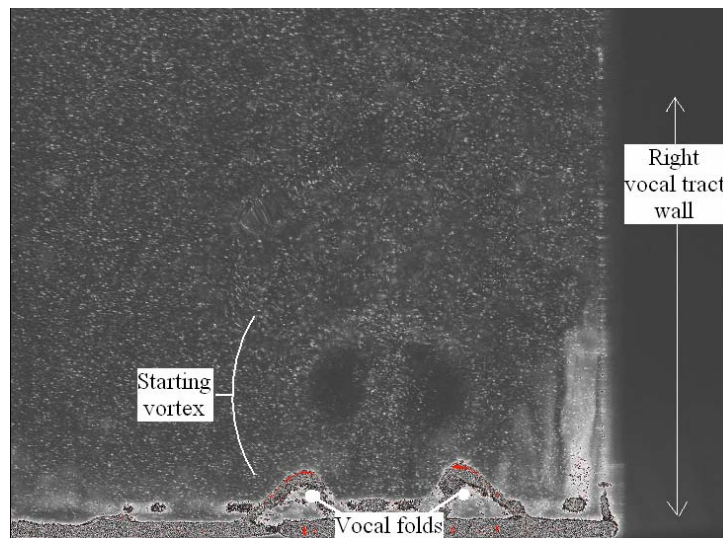
Figure 4-8 Example of PIV image.

4.4.2   PIV Setup

Figure 4-3 shows the PIV arrangement, where the laser sheet as shown extends normal to the page. A LaVision PIV system was used (including a LaVision Imager Intense CCD camera, LaVision Aerosol Generator, and a New Wave Research Solo II Nd:YAG laser). DEHS oil (di-ethyl-hexyl-sebacate, or bi(s)-ethyl-hexyl-sebacate, CAS.# 122-62-3, purchased from Sigma Aldrich, Product # 84822) was used for flow seeding. It is noted that olive oil had been attempted to be used previously, but DEHS oil demonstrated less accumulation on glass viewing surfaces (see Sec. 4.4.1). The LaVision software package, DaVis, was used for image acquisition and processing.

The laser was centered on the medial-coronal and the anterior-posterior planes of the model. The camera was positioned so that the top of the vocal fold model was just above the bottom of the field of view, with the glottal jet approximately centered left-to-right. Care was taken to make all surfaces in the field of view as dark as possible to minimize laser reflection into the camera. The vocal fold fixture was often checked to make sure that the model was correctly centered and level in the camera frame. The camera field of view was adjusted to extend to an area as wide as the inside of the vocal tract and just higher than the false folds, or about 22 mm (horizontal) × 16 mm (vertical). Calibration was accomplished by placing a ruler in the camera view. A typical calibration constant was approximately 54 pixels/mm.

Ensemble averaging was used to reduce noise and to calculate average and RMS velocity quantities; see Figure 4-9. It was first determined how many image pairs were necessary for convergence of these values. This was done for two points in the flow field. Point 1 was in the jet centerline, a short distance above the glottal exit. Point 2 was

located at the same vertical distance above the glottal exit, but was positioned in the jet shear layer. Figure 4-10 shows the results of this study.

According to Figure 4-10, the average velocity and RMS velocity appear to have nearly stabilized between 100 and 200 averages for both point locations, although some fluctuations persist. As the number of averages increases, so also do the time and computer storage requirements. Further, in cases with a vocal tract, more averages meant more time for oil to accumulate on the glass. As a compromise, 100 averages were used at the 1.25 and 1.5 kPa pressure studies, and 50 were used at the 1.9 kPa pressure.
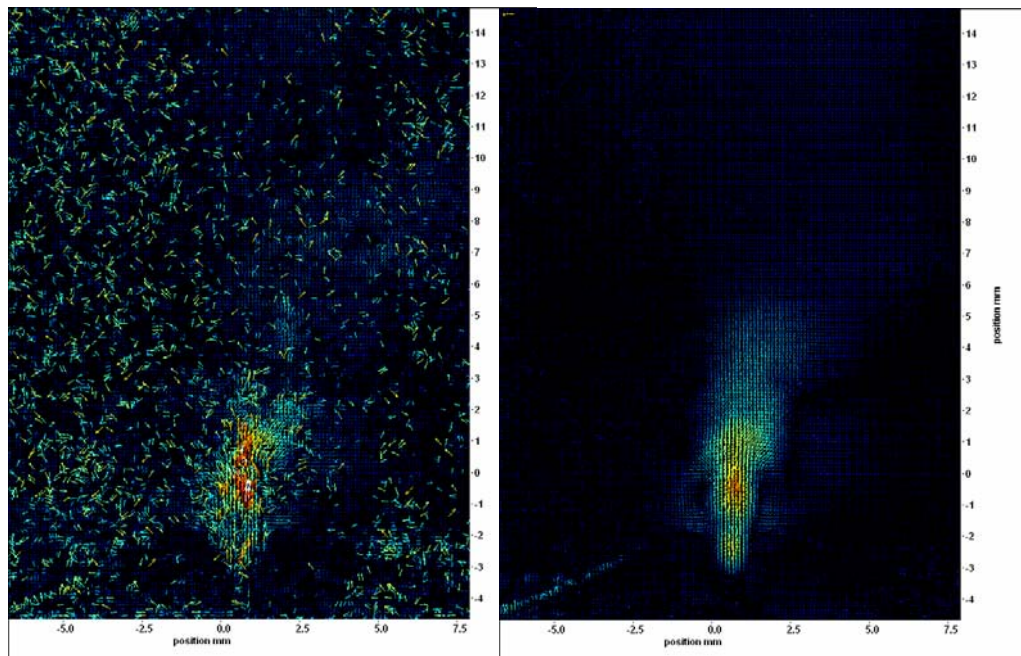
Figure 4-9 Instantaneous (left) and ensemble-averaged vector fields (right).

79
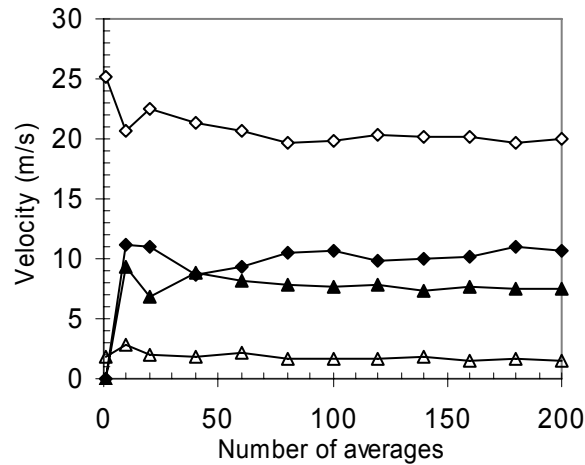
Figure 4-10 Convergence of measured velocities for increasing number of images used in ensemble averaging. ($\diamond$ = jet core average velocity, $\blacklozenge$ = jet core RMS velocity, $\triangle$ = shear layer average velocity, $\blacktriangle$ = shear layer RMS velocity).

As discussed in Section 3.4.4, the model frequency was fairly consistent. However, even small fluctuations in frequency would inhibit successful ensemble averaging based on a constant frequency of data acquisition. Therefore, a phase-locking circuit was constructed to trigger the PIV image acquisition using the sub-glottal pressure sensor. This active circuit was very successful at phase-locking the image acquisition with the vocal fold vibration; a schematic is contained in Appendix A. The PIV software allowed for adjusting the time delay after receiving a trigger input. Using this feature, 30 phases of vocal fold oscillation were interrogated, with either 100 or 50 image pairs (see preceding paragraph) collected at each phase. These image pairs were analyzed using a cross-correlation with a non-weighted, double-pass, decreasing window size (32×32 to 16×16 pixels), 50% overlap, cross-correlation algorithm. The vector fields were then ensemble-averaged and the RMS velocity fields were calculated. Data for the three sets

consumed more than 150 GB of hard drive space, and vector processing took approximately five days using two desktop computers.

Each case took approximately 10 minutes to record the data. The nine separate cases repeated at three different pressures therefore required approximately 4.5 hours of nearly continuous synthetic model vibration. Considering the additional time involved in experiment preparation, the model was actually run for many hours more than the time required for the final data sets. This is much longer than that which is capable using excised larynx models.

4.5   PIV Results

This section reports the following quantitative PIV data: average velocity, jet centerline angle, and RMS velocity. Because the velocities of the p = 1.5 kPa case were similar to the p = 1.25 kPa case, the average and RMS velocity plots of the p = 1.5 kPa case are not presented.

4.5.1   Average Velocity

For all three pressures, jet core average velocities calculated using PIV agreed with the predicted values using the simplified Bernoulli equation,

$$V = \sqrt{\frac{2\Delta P}{\rho}}$$,

(4.1)

where ΔP is the measured time-averaged sub-glottal pressure and ρ is the ambient density of air (1.03 kg/m^3). The velocities calculated using Equation 4.1 were in the range of

49.8 to 61.4 m/s, based on the pressures tested (1.25, 1.5, and 1.9 kPa). The PIV-measured average velocity values were obtained from visual inspection of the calculated PIV vector fields and their resulting color bar scaling. The PIV-measured average velocities are similar to those measured by Alipour and Scherer (1995) using excised canine larynges, and to those calculated using Equation 4.1.

Estimates of Reynolds numbers and Strouhal numbers, shown as Equations 4.2 and 4.3, respectively, for the three pressure values used were calculated based on a method described in Alipour and Scherer (2006),

$$\text{Re} = \frac{U_m D_h}{\nu},$$ **(4.2)**

$$St = \frac{f D_h}{U_m},$$ **(4.3)**

where U_m is the mean velocity through the glottis (Equation 4.4), D_h is the hydraulic diameter (Equation 4.5), ν is the kinematic viscosity of the fluid, and f is the frequency of vocal fold oscillation.

$$U_m = \frac{Q}{A_g}$$ **(4.4)**

$$D_h = \frac{4 A_g}{G_p}$$ **(4.5)**

For Equations 4.4 and 4.5, Q is the time-averaged flow rate (see Section 4.4.1 for flow rate values), A_g is the maximum glottal area, and G_p is the corresponding measured glottal perimeter. The glottal area and perimeter were calculated based on expressions for the area and perimeter of an ellipse,

$$A_{ellipse} = \pi(length)(width),\tag{4.6}$$

$$P_{ellipse} = 2\pi\sqrt{\frac{(length^2 + width^2)}{2}},\tag{4.7}$$

where $P_{ellipse}$ is an approximate formula. Four points were required to measure the length and width of the glottal area. These points were measured using the high-speed images shown in Figure 4-1 and a modified version of the MATLAB script mentioned in Section 3.4.3 and shown in Appendix B.

Table 4-1 shows the results of the calculations just described. These values are in the same range as data from excised canine larynges reported in Alipour and Scherer (2006), and support the conclusion that the jet flow exiting the glottis should be laminar (based on a transitional Reynolds number of 2300).

Table 4-1 Estimated values of Reynolds and Strouhal numbers for PIV-experiments.

P (kPa)	Re	St
1.25	727	0.008
1.5	1054	0.010
1.9	1621	0.077

Figures 4-11 through 4-14 show ensemble-averaged velocity plots for the $p = 1.25$ and p = 1.9 kPa cases; descriptions of the plot labels can be found in Figure 4-6, as well as in the geometric icons on the outer edges of each figure. For all pressures and all cases, a starting vortex was observed (as seen in Figure 4-8). The vortex appeared to last for more than half of the jet lifetime in most of the test cases. This starting vortex included points of low velocity near the center of fluid rotation on each side of the jet centerline; this low velocity zone tended to grow laterally as the jet developed. It is noted that early in test preparation, the model showed less of a tendency to adhere to itself, and in these cases the vortex was less obvious; a vortex street was more common. It is conjectured that the adhesion (observed during the high-speed imaging experiments, see Section 4.2) delayed the opening of the center of the glottis, causing a delay in jet formation, thereby resulting in a more impulsive jet than might otherwise have developed.

Concerning whether or not the presence of the vocal tract delayed jet growth (as was hypothesized by Shadle et al., 1991), it is difficult to determine from these experiments. Assuming the range of frequencies expected from the model (132 ± 0.8 Hz), there could be variability in the comparison of jet cycles as much as 92 μs. The time for one phase to occur is the period ($1/f$) multiplied by the inverse of the number of phases (1/30), which equals 253 μs. Because the frequency variability is a large percentage of the phase spacing time, it was difficult to precisely phase-match each case.
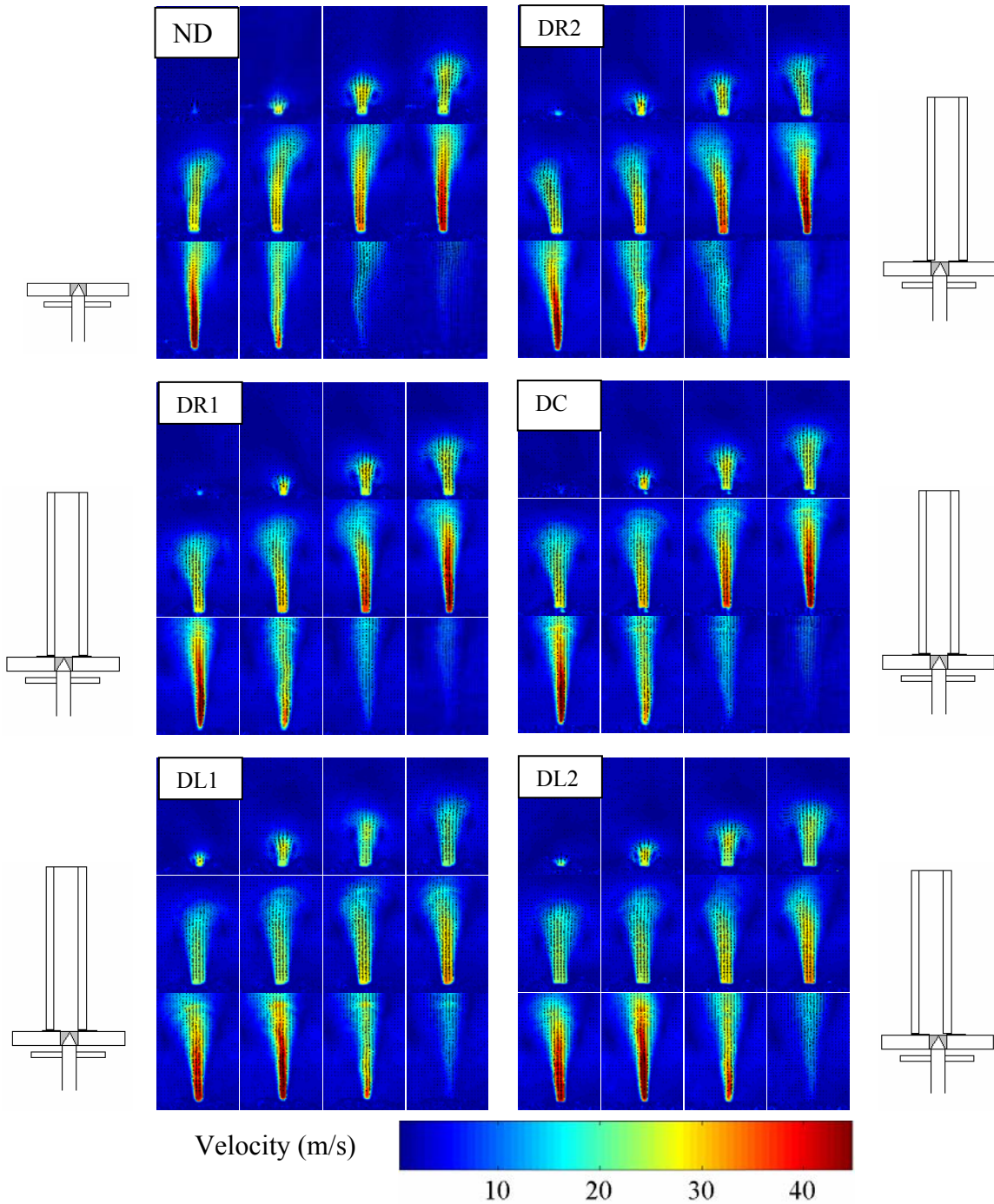
Figure 4-11 Average velocity plots for duct and open cases at different phases (*p*=1.25 kPa). The icons on the outside of each plot show the respective test geometry. The cycle proceeds from left to right and from top to bottom for each set of images.
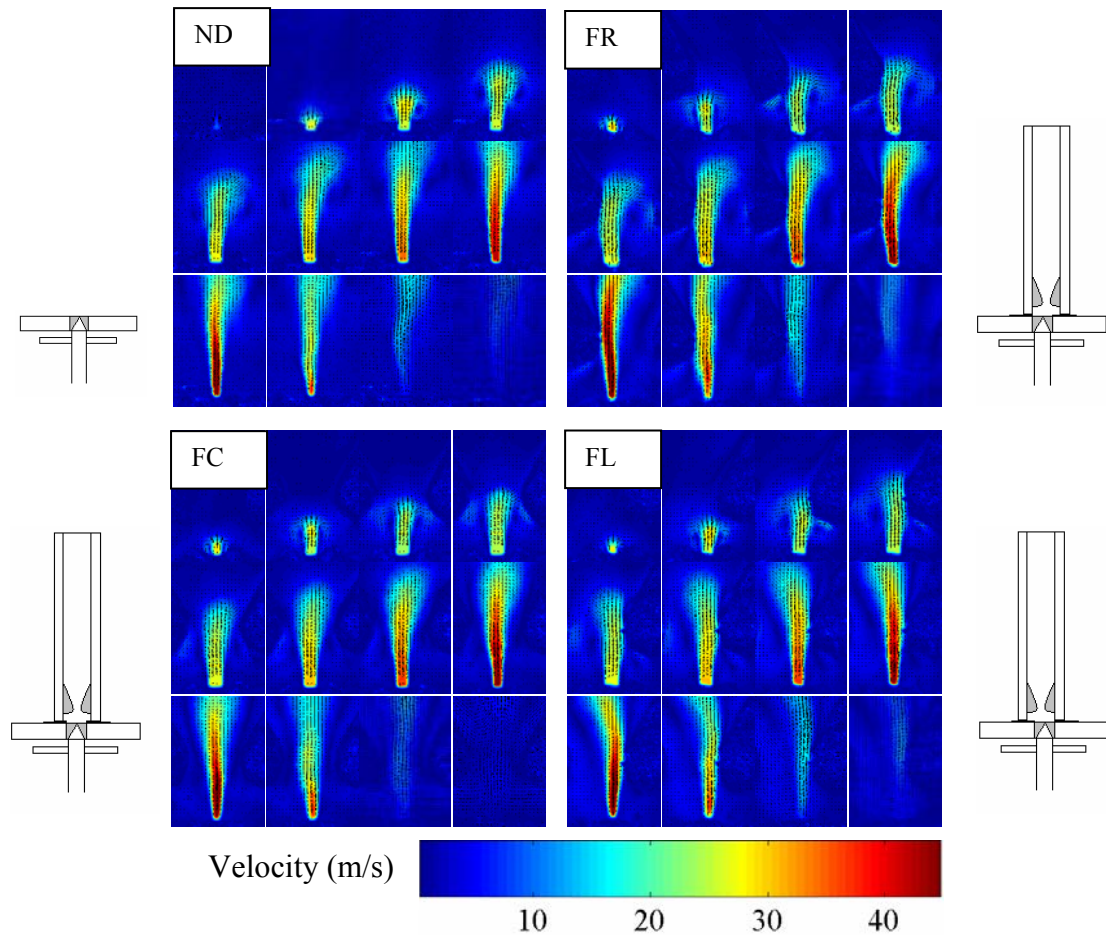
Figure 4-12 Average velocity plots for false folds and open cases at different phases (*p*=1.25 kPa). The icons on the outside of each plot show the respective test geometry. The cycle proceeds from left to right and from top to bottom for each set of images.

Figure 4-12 compares the false fold cases with the open jet case for *p* = 1.25 kPa. For the symmetric false fold case, the false folds clearly interfered with the starting vortex. This effect was repeated for both asymmetrical false fold cases, with the vortex nearest to the vocal tract center persisting longer than that nearest to the false folds. A small vortex can also be seen in the laryngeal ventricle on the false fold side. This jet interaction with the false folds may contribute to the overall sound production through a fluid-solid interaction. Further, the "grazing" of the jet over the laryngeal ventricle could

act as a kind of acoustic (Helmholtz) resonator. It also appears that in the asymmetric cases, the jet tended to deflect away from the nearest false fold after the jet had reached the false fold. This deflection could be due to either the jet impingement or to the vortex interaction, or a combination of the two.

The jet in the $p = 1.9$ kPa vocal tract cases of Figure 4-13 appeared to be narrower than the open jet case, taking more of an inverted wedge shape than the constant jet width open jet. This effect may not reflect reality, due to the thinning at the base likely being attributed to poor visibility due to oil accumulation on the vocal tract glass wall. In any case, the starting vortices are still visible.

The false fold cases at 1.9 kPa are shown in Figure 4-14. The FR and FL cases show the jet deflecting away from the nearest false fold as the jet path is interrupted by the presence of the false folds. The FR case shows a second vortex shed from the downstream side of the false fold as the jet passes the false fold. This was not seen in the 1.25 kPa cases, and it is not clear whether it occurs in the FL case. However, it is possible that this occurrence was related to the higher pressure. Also, the jet width is wider for the false fold cases than for the vocal tract or open jet cases. The jet width variations may have been due to adhesion of the vocal fold surfaces.

The PIV-measured velocities were generally lower for the vocal tract cases than for the open jet case, and the jet seemed to decay more quickly at the extreme asymmetry positions than for the middle three positions.

Figure 4-13 Average velocity plots for duct and open jet cases at different phases (*p*=1.9kPa). The icons on the outside of each plot show the respective test geometry. The cycle proceeds from left to right and from top to bottom for each set of images.
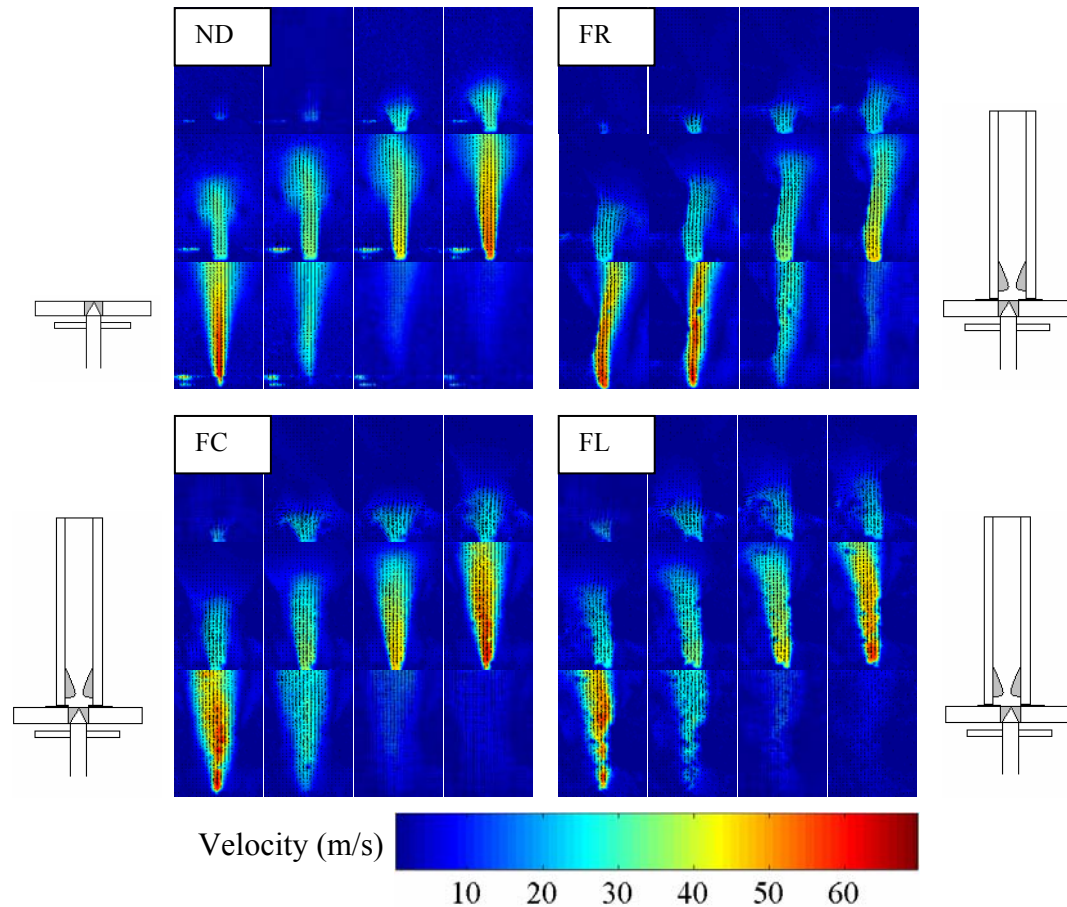
Figure 4-14 Average velocity plots for false folds and open jet cases at different phases (*p*=1.9kPa). The icons on the outside of each plot show the respective test geometry. The cycle proceeds from left to right and from top to bottom for each set of images.

As mentioned in Chapter 2, some PIV vocal fold experiments have demonstrated bi-modal ("flapping") jet behavior. It is noted that examination of the instantaneous PIV velocity data in this study did not show any of this behavior. Erath and Plesniak (2006b) stated that the flapping behavior was never observed for divergent glottal profiles of 40° or greater. While the glottal profile was not measured as part of this thesis, it is possible that the exit profiles for these experiments reached angles near or greater than 40°. Another possible explanation is that the self-oscillating setup used here is fundamentally different from the Erath test setup. Recall that their model was driven by a set of rotating

shutters downstream of a static vocal fold model with a divergent profile. The rotating shutters constitute a fluctuating downstream boundary geometry, which is not to be expected in real phonation.

4.5.2   Jet Centerline Plots

Erath and Plesniak (2006a) described a method for determining the jet deflection angle at a given point downstream of the glottis. Based on his approach, the following procedure was developed to identify the entire jet core centerline over a complete cycle of oscillation at n discrete phases ($n = 30$ for this experiment, as mentioned in Section 4.4.2).

The jet centerline was located using the average velocity data and a MATLAB script as follows (see Appendix B for the code). Spurious vectors along the right and left edges of each average velocity image were set to a value of zero (e.g., in the duct walls). The following steps were performed at each vertical position above the glottal exit:

1. A minimum velocity threshold was determined based on evaluations of the jet growth, and this threshold was used to determine when the jet began and when it decayed (7 m/s was used in these experiments).

2. Smoothing was accomplished along the horizontal line by averaging each vector and its six neighboring vectors (±3 on each side).

3. The maximum jet velocity was identified using the smoothed velocity profiles.

4. The jet core was defined as all vectors that had a value of greater than 80% of the maximum jet velocity.

5. The jet center was defined to be located at the geometric center of all
vectors within one standard deviation of the jet core mean value.

The jet centerline was constructed from the individual jet centers combined over the entire range of vertical positions above the glottis, and this "rough" centerline was then smoothed in the vertical direction using an average of the individual centerline point and four (±2) of its neighboring centerline points. Figure 4-15 shows the examples of the jet centerline finding algorithm. To facilitate the identification of trends in the skewing of the jet centerline, the jets horizontal motion was scaled to be approximately 2× the vertical scaling, as seen in Figures 4-16 through 4-19.
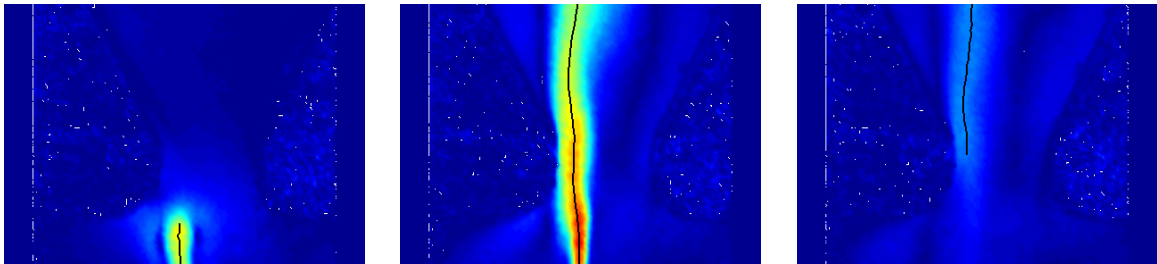
Figure 4-15 Sample of selected phases from jet centerline calculation algorithm applied to FR case with p = 1.25 kPa. Times of initial jet growth (left), full jet (center), and decaying jet (right) are shown. The extreme right and left sides of each image (areas of potentially spurious vectors) have been removed.

As in the average velocity measurements, see Figure 4-6 for descriptions of the plot labels used in the following jet centerline figures, or use the geometric icons shown at left of the figures. For the open jet cases at p = 1.25 kPa (see Figure 4-16), the model has a tendency to skew to the right. However, the initial stages of jet development skew towards the nearer wall in the vocal tract cases (this can be confirmed in Figure 4-11). Eventually the jet in the open and the vocal tract cases generally straightens out.

The extreme right duct position (see Figure 4-11 and Figure 4-16, DR2) clearly skewed the jet to the left towards the nearest wall. This behavior was the most significant change from the open jet case.

The false fold cases for p = 1.25 kPa (shown in Figure 4-17) shows the opposite behavior as that seen in Figure 4-16. The jet skews *away* from the nearer wall and from the nearest false fold towards the duct centerline. The symmetric false folds case and the open jet case are very similar.

When the false folds are offset with respect to the vocal fold model, the jet has an initial tendency away from the nearer wall, then straightens, and then is further skewed by the continued presence of the false folds.

For the vocal tract and open jet cases at the highest pressure (p =1.9 kPa, see Figure 4-18), the closer the jet was to the wall, the more it tended to skew towards the wall in its initial development. This tendency appears to be a function of the sub-glottal pressure, as the lower pressure cases did not show the same degree of skewing. As the portion of the cycle for which the jet is present reached its halfway point, the jet centerline had generally straightened out.
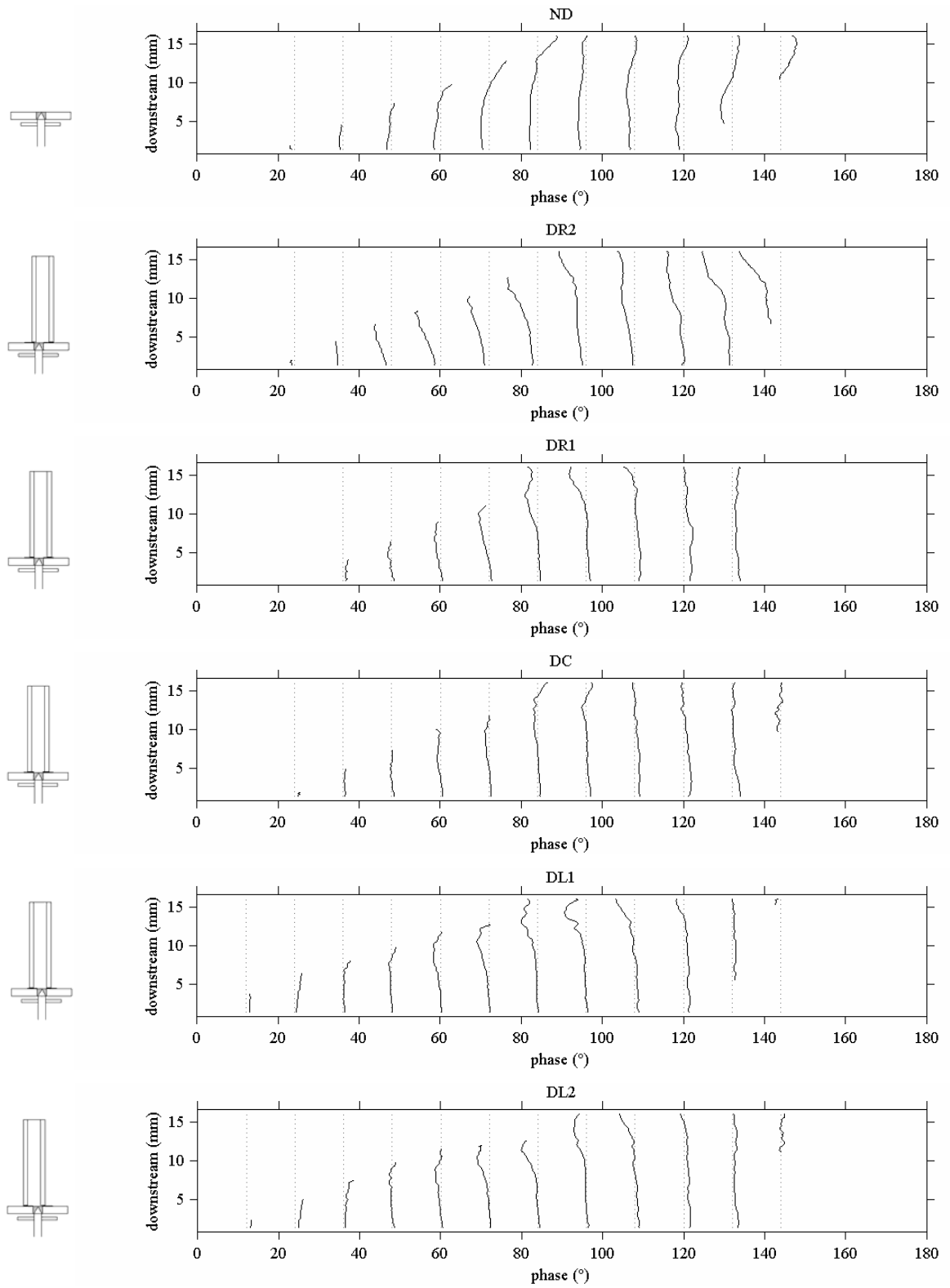
Figure 4-16 Jet centerline plots for duct cases at *p*=1.25 kPa. The respective label for each plot is listed at top of plot.
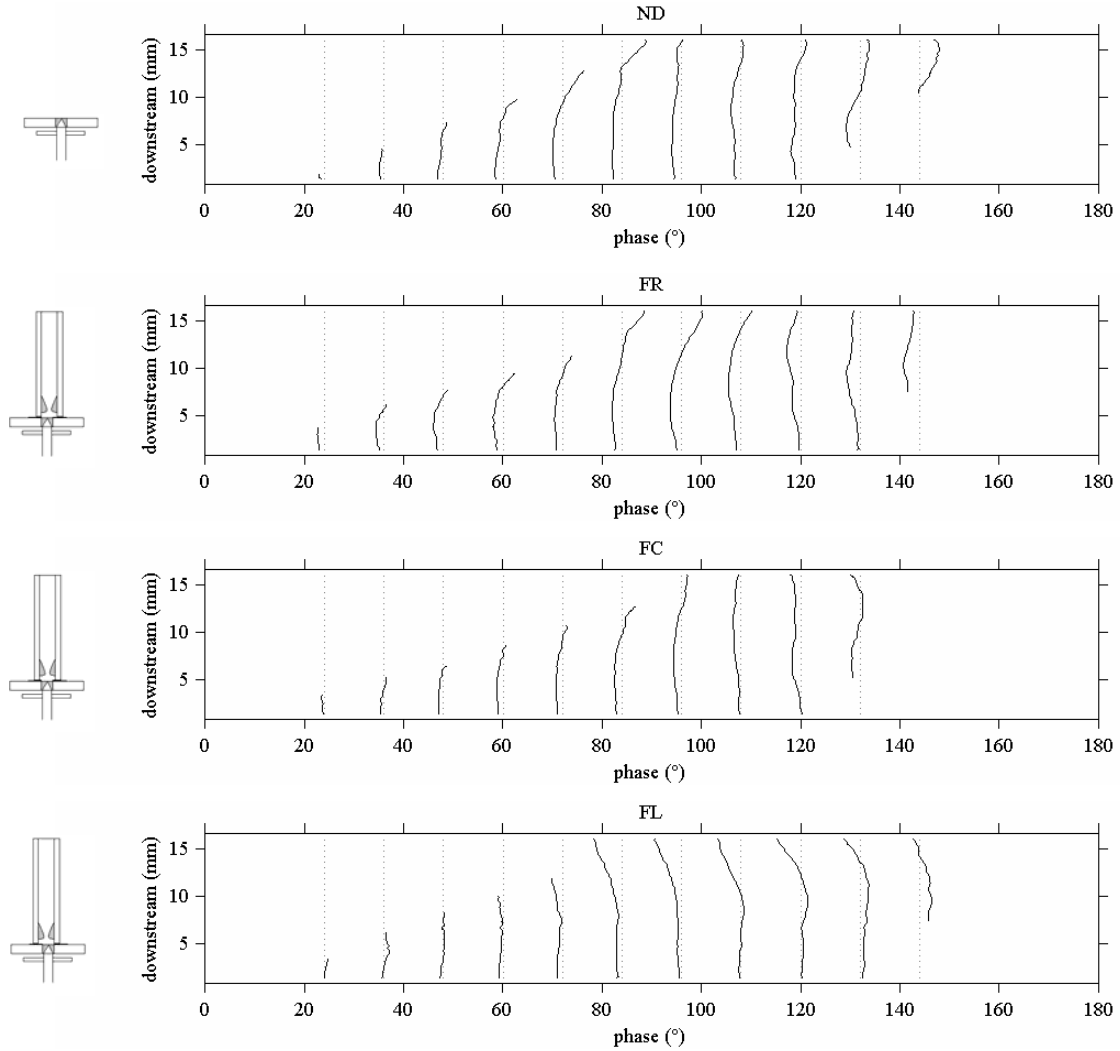
Figure 4-17 Jet centerline plots for false folds at *p*=1.25 kPa. The respective label for each plot is listed at top of plot.

Wiggles in the centerlines shown here represent a decaying jet, which is characterized by decreasing velocities that more closely match the velocity of the ambient duct air. These can also be due to oil accumulation on the glass viewing surface when the data was recorded, somewhat reducing the quality of the plot.

94
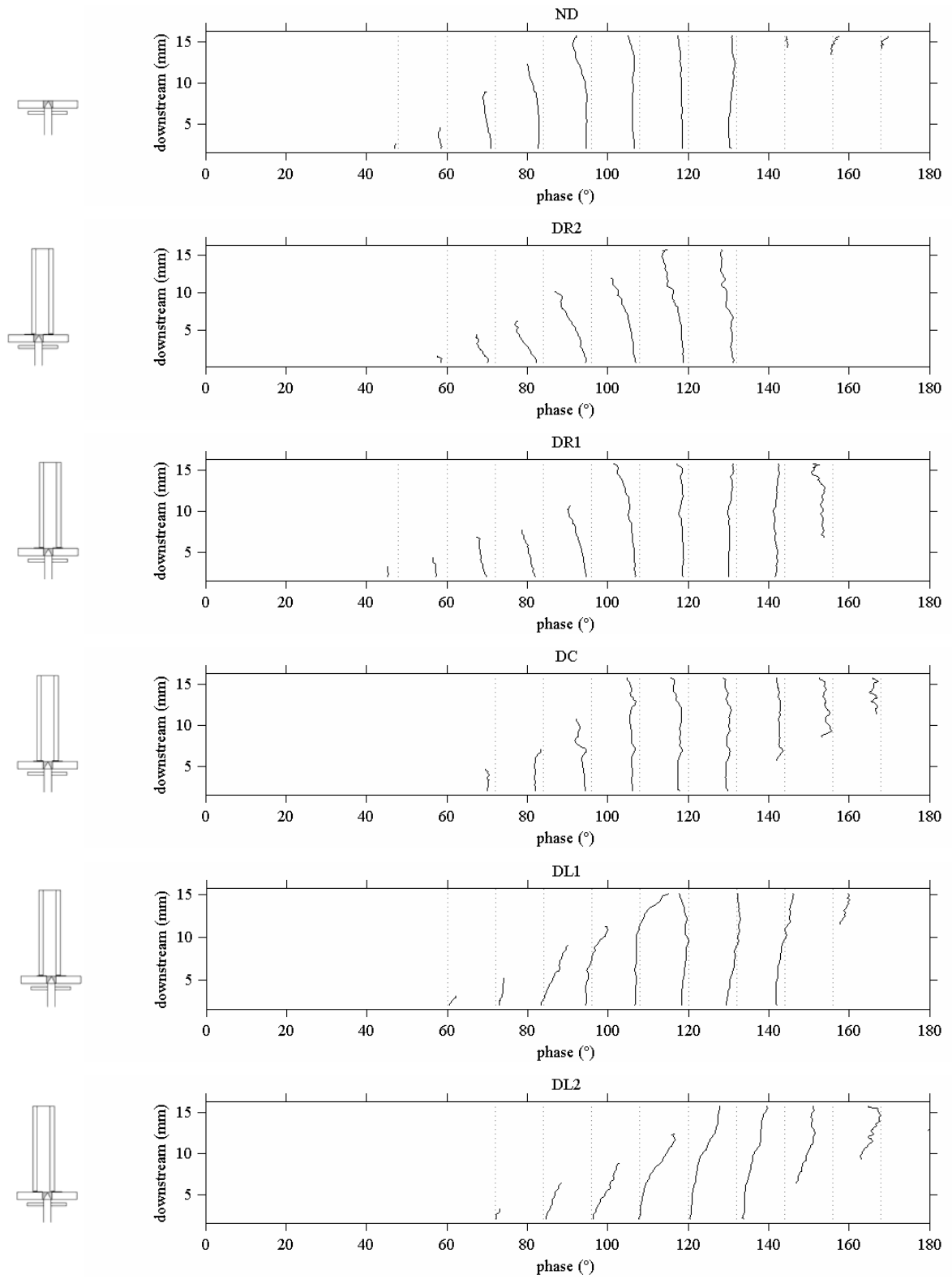
Figure 4-18 Jet centerline plots for duct cases at *p*=1.9 kPa. The respective label for each plot is listed at top of plot.

The presence of the false folds in Figure 4-19 forced the jet away from the nearest wall towards the vocal tract centerline and between the medial surfaces of the false folds. This trend was most evident at the beginning of the jet cycle; the jet straightened somewhat as the cycle proceeded.
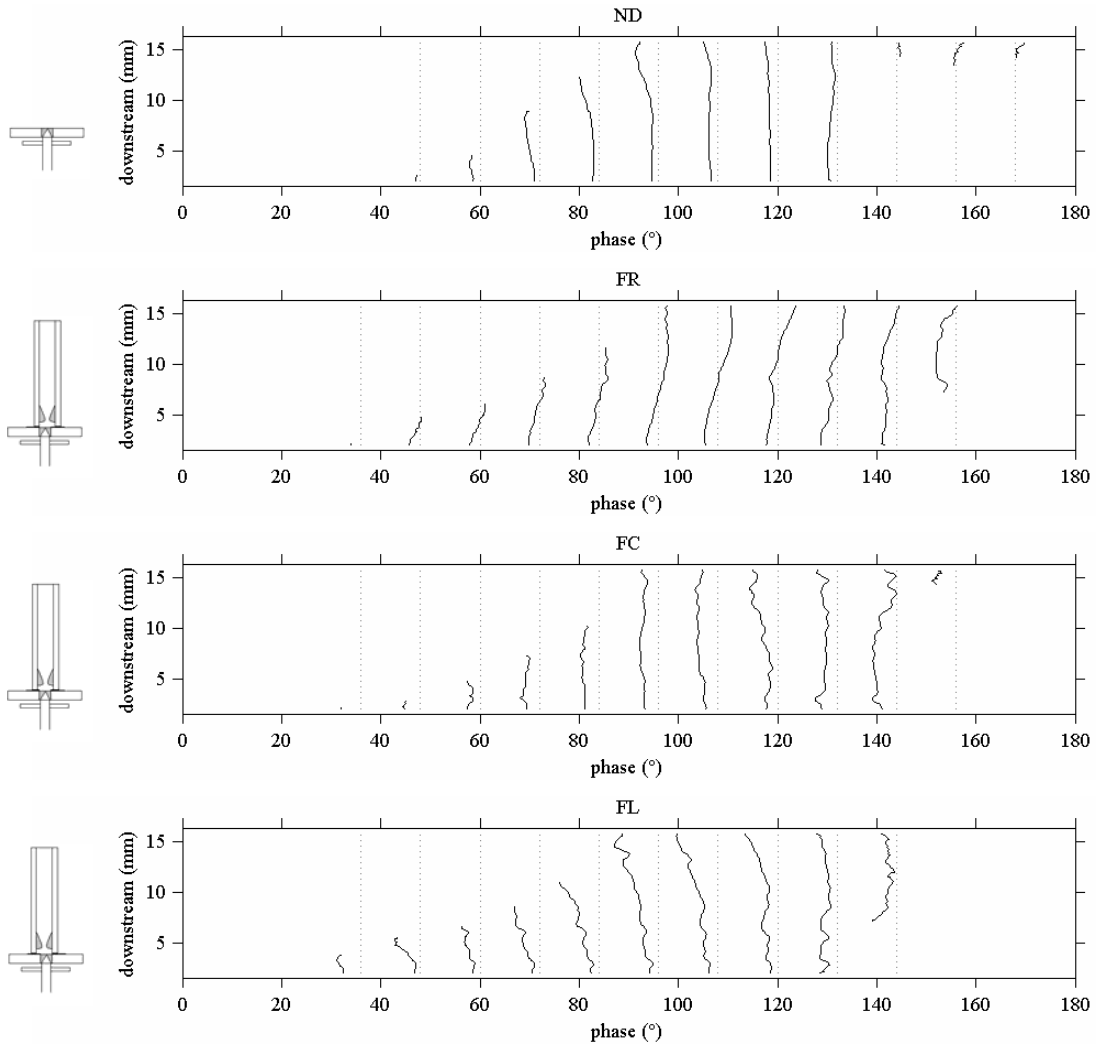
Figure 4-19 Jet centerline plots for false folds at *p*=1.9 kPa. The respective label for each plot is listed at top of plot.

There was some variability in the asymmetrical duct placement (as much as 0.5 mm), which was the reason for selecting fewer offset positions. This variability will certainly influence the resulting measurements. However, the trends of a duct case skewing towards the nearer wall and a false fold case skewing away from the nearer wall were consistent.

4.5.3 RMS Velocity

The RMS (root mean square) of the velocity is a measure of the fluctuation of the instantaneous velocity fields, and is calculated according to Equations 4.8 – 4.10:

$$RMS_X = \sqrt{\frac{1}{n-1}\sum_i (u_i - \bar{u})^2} \; , \tag{4.8}$$

$$RMS_Y = \sqrt{\frac{1}{n-1}\sum_i (v_i - \bar{v})^2} \; , \tag{4.9}$$

$$|RMS| = \sqrt{\left(RMS_X^2 + RMS_Y^2\right)}, \tag{4.10}$$

where n is the number of averaged image-pairs at a given phase, u_i and v_i are the x- and y-components of the instantaneous velocity of the ith image pair, and $\bar{u}$ and $\bar{v}$ are the local average x- and y- velocity components. Calculation of the RMS velocity field is useful because it identifies the jet shear layer (and the corresponding jet core) and the local jet fluctuations (which can indicate areas of more intense mixing). The results of |RMS| from Equation 4.10 are shown in Figs. 4-20 through 4-23.

In these plots, the colors denote differing velocity fluctuations. In general, most of the |RMS| velocities appeared to be in the range of 5 − 10 m/s. The higher |RMS| velocities were in the 10-15 m/s range. As would be expected, the |RMS| values were highest along the jet shear layer and lowest in regions of the jet core. In some regions of some cases, the |RMS| values were particularly high because of issues such as low seed particle density outside of the open jet, reduced laser illumination in the laryngeal ventricle, and spurious vectors in no-flow regions (such as through the false folds).

The duct case results in Figure 4-20 uniformly show higher |RMS| values in the leading vortex than the open jet case, suggesting that the leading vortex may emerge more consistently (in terms of velocity and perhaps bearing) in the open case than in the confined case. In all of these cases (duct and open jet), a laminar core that persisted a short distance downstream of the glottis is evident over most of the cycle. This laminar core disappeared during glottal closing; this is consistent with observations of Mongeau et al. (1997) and Zhang et al. (2002) that the quasi-steady assumption begins to break down during glottal closing due to jet turbulence. They also indicated that this assumption is not as good during opening, and the results here suggest the possibility that it may be more due to fluctuations or unsteadiness in the starting vortex rather than to jet turbulence. Asymmetry in the vocal tract position did not seem to noticeably influence the |RMS| values.
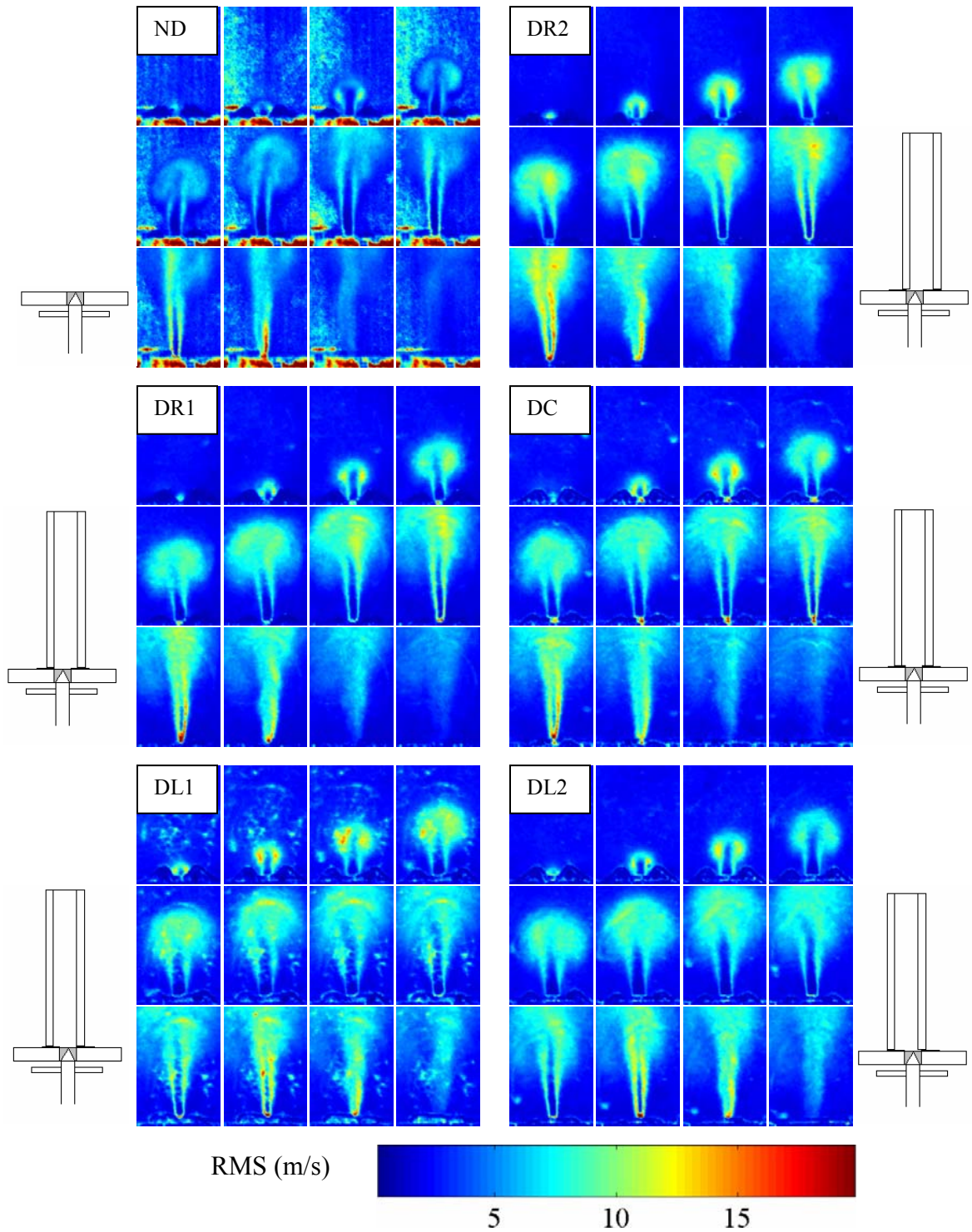
Figure 4-20 |RMS| velocity plots for duct and open jet cases at different phases (*p*=1.25kPa). The icons on the outside of each plot show the respective test geometry. The cycle proceeds from left to right and from top to bottom for each set of images.
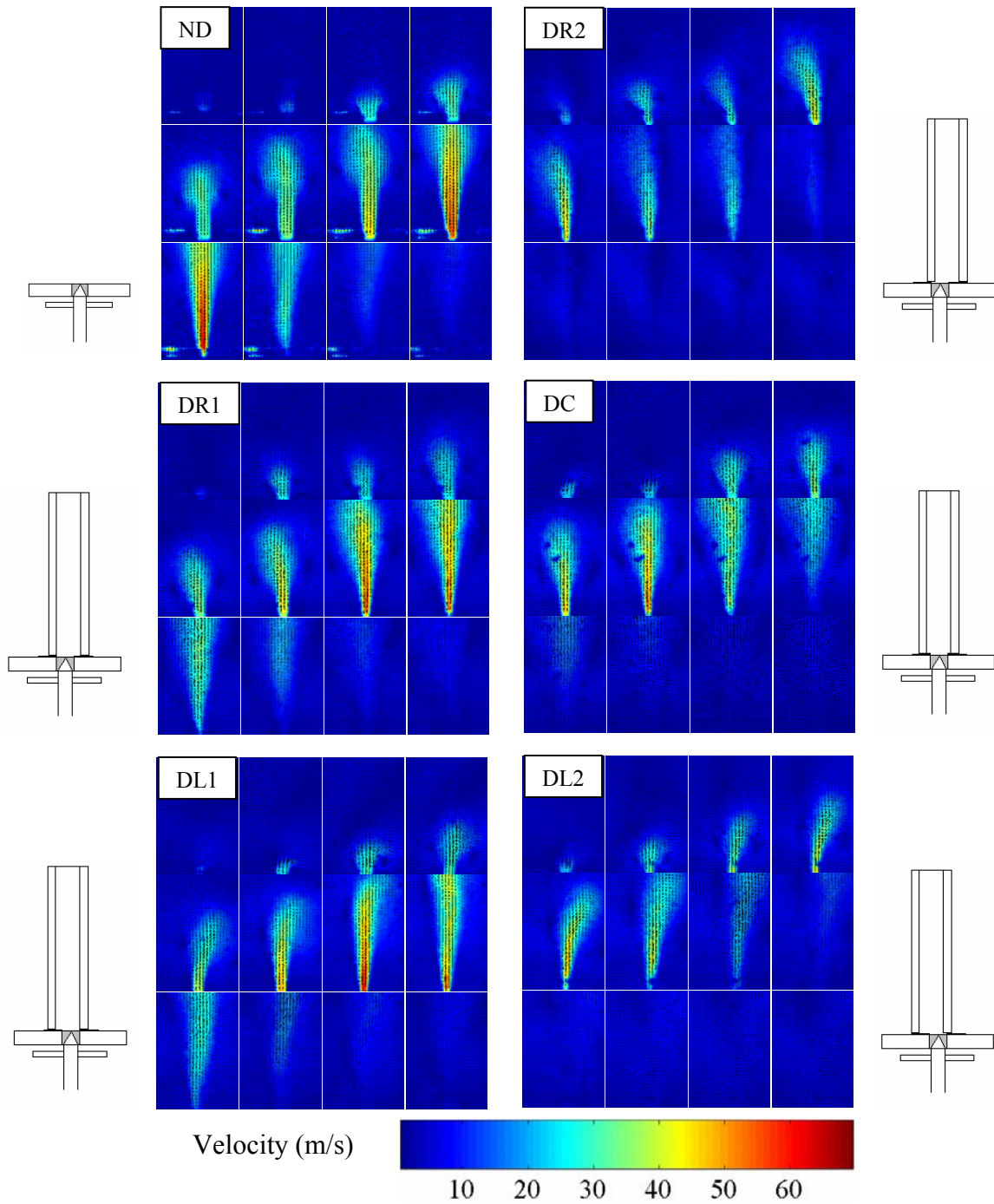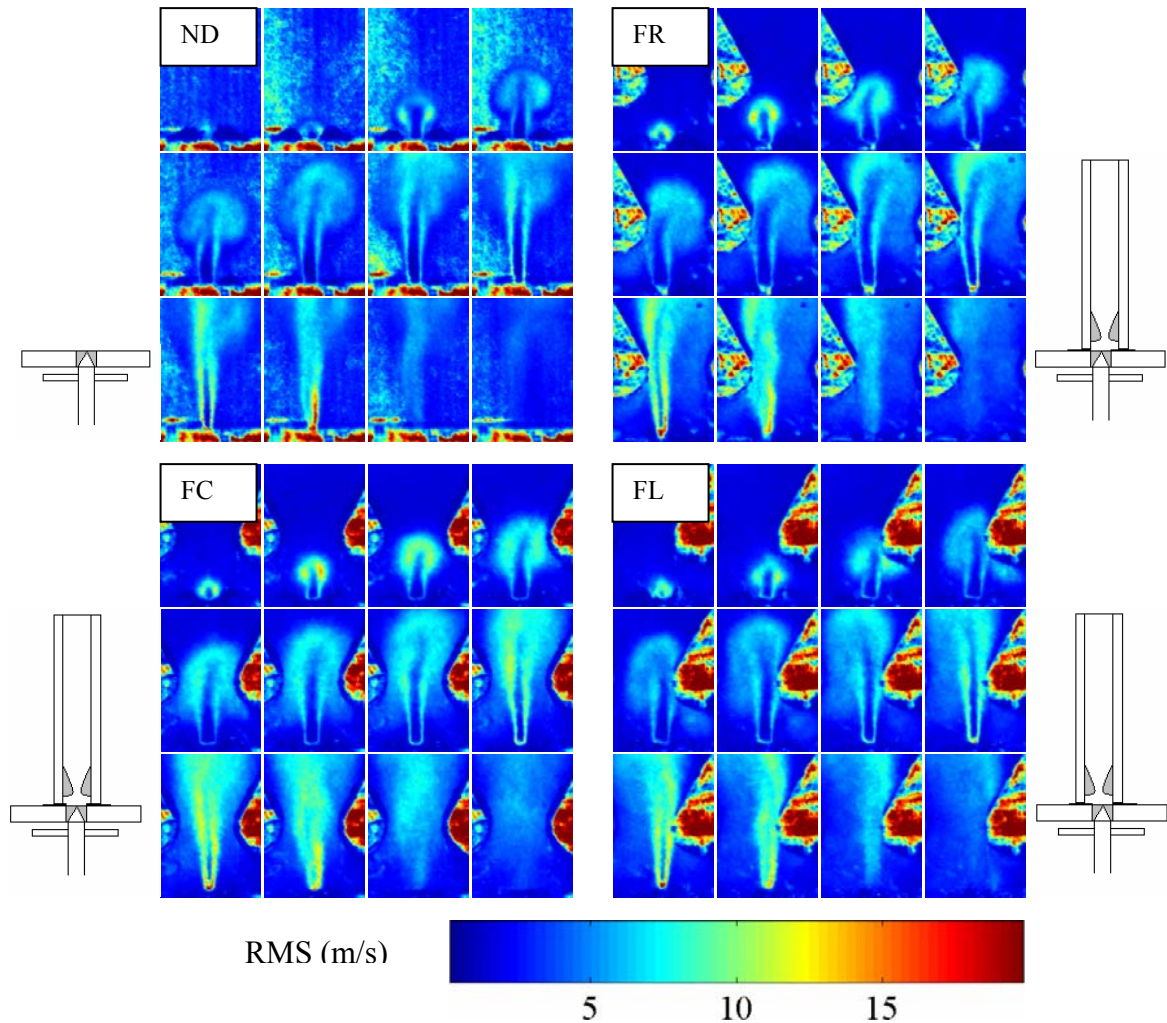
Figure 4-21 |RMS| velocity plots for false folds and open jet cases at different phases (*p*=1.25kPa). The icons on the outside of each plot show the respective test geometry. The cycle proceeds from left to right and from top to bottom for each set of images. The darker red areas are the tip of the right false fold, or the base of the vocal fold model in the open jet case.

The |RMS| plots assist in visualizing the interaction with the false folds. Comparison of the FL, FC, and FR cases suggests that the vortex interaction with the false folds (see Figure 4-21 and Figure 4-23) may have reduced the overall |RMS| values in the starting vortex, suggesting a potentially stabilizing influence of the false folds. Other features of the jet, such as laminar core characteristics, do not seem to be significantly altered.
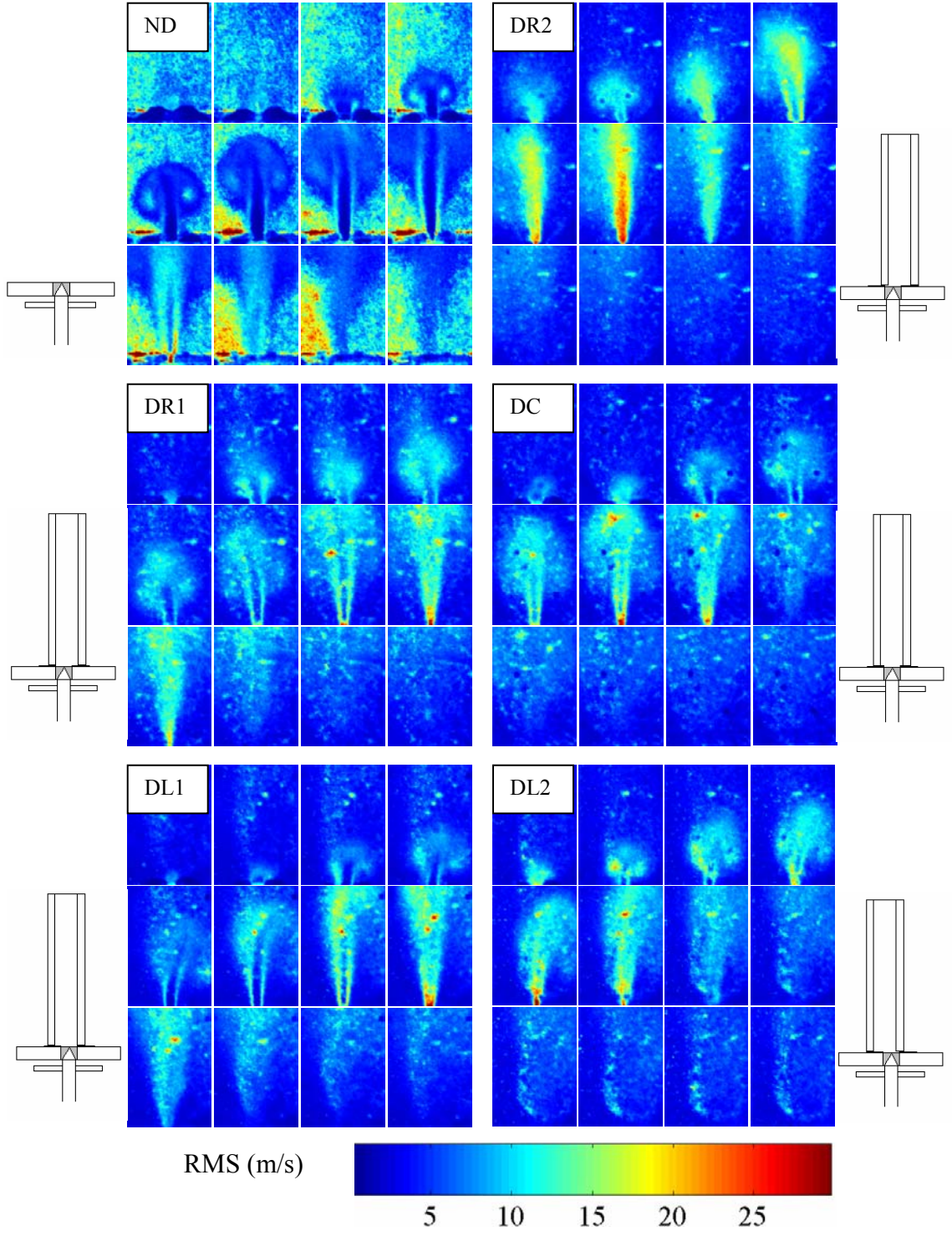
Figure 4-22 |RMS| velocity plots for duct and open jet cases at different phases (*p*=1.9kPa). The icons on the outside of each plot show the respective test geometry. The cycle proceeds from left to right and from top to bottom for each set of images.

Figure 4-22 shows the |RMS| velocity for the vocal tract case at p = 1.9 kPa. The laminar core is nearly non-existent when the jet was nearest the duct walls (DR2 and DL2 cases). The less asymmetric cases (DR1, DL1) did show a distinct laminar core. The symmetric case showed a smaller laminar core than the DR1 and DL1 cases. With the presence of the false folds (seen in Figure 4-23), the laminar core is evident over some parts of the cycle, although the jet is again very turbulent during closing.

RMS (m/s)

5   10   15   20   25
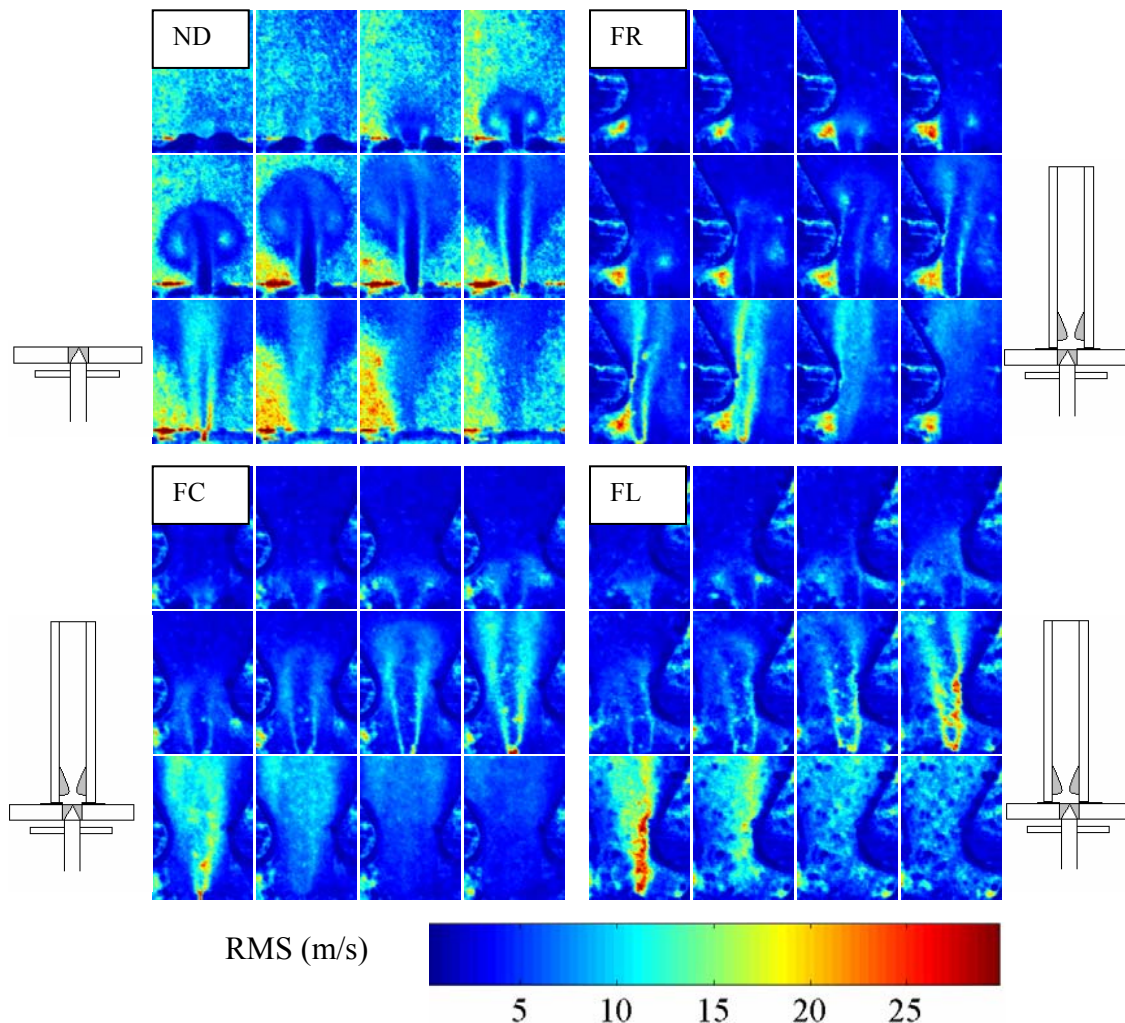
Figure 4-23 |RMS| velocity plots for false folds and open jet cases at different phases (p=1.9kPa). The icons on the outside of each plot show the respective test geometry. The cycle proceeds from left to right and from top to bottom for each set of images. Region of red near the bottom left corner of FR is attributed to problems with oil accumulation on the glass under the left false fold.

4.6   Summary

A single two-layer model was measured using high-speed imaging and particle image velocimetry (PIV). These measurements were performed while the model vibrated at three different pressures: 1.25, 1.5, and 1.9 kPa. High-speed imaging of the superior view of the vocal fold model showed that the glottis only opened about half-way at the lowest pressure. This was confirmed by the sagittal view at the same pressure. As the pressure was increased, the glottis fully opened, and a starting vortex was observed in the coronal view for the two highest pressures.

Adhesion between the medial surfaces of the vocal fold model was apparent. This adhesion created a double-orifice for a portion of the cycle, and appeared to delay the jet formation, which contributed to the impulsive nature of the starting vortex. The lateral and inferior-superior motion of the vocal fold model was dramatic; in particular, the medial-superior surfaces were seen to collide with one another prior to adhesion and then rebound.

A physical condition known as a posterior commissure, seen in real vocal fold vibration, was observed in the model and highlights the potential for synthetic models to replicate real vocal fold phenomena for parametric studies. At the lowest pressure, a constant jet exited from this seam, while a medial-sagittal jet formed for a small portion of the oscillation cycle. As the pressure increased, the scale of the medial-sagittal jet grew substantially and the jet at the posterior commissure was barely visible in comparison.

PIV measurements of average glottal jet velocity agreed with velocities measured using excised larynges and with predictions from the simplified Bernoulli equation. The

average velocity fields were measured for nine different vocal tract configurations, which included an open jet, five cases of varying vocal tract symmetry without the false folds present, and three cases of varying vocal tract symmetry with the false folds present. These experiments were repeated for the same three pressures as in the high-speed imaging. A starting vortex was observed in all cases. In the false fold cases, the presence of the false folds in the vocal tract obstructed the downstream convection of the starting vortex lobes. For example, in asymmetrical false fold cases, the side of the vortex nearest a false fold was prevented from developing with the rest of the jet farther downstream. And in the symmetric case, the false folds applied equal obstructive influence, effectively squeezing both sides of the starting vortex. In one case, a new vortex structure was seen to be shed from the surface of the false folds themselves.

The jet core centerline was calculated using a MATLAB algorithm and the average velocity data. The two primary results of these experiments were that when the vocal tract was asymmetrically positioned with respect to the vocal fold model, the resulting jet centerline skewed towards the nearest wall in the vocal tract cases, but away from the nearest wall (and towards the vocal tract centerline) in the false fold cases. In the vocal tract cases, as the gap between the jet and the nearest wall decreases, the fluid available to be entrained into the jet flow decreases. If there is less fluid to be entrained, then the fluid that is entrained is going faster, which leads to a decrease in pressure. This pressure imbalance between the far and near walls forces the jet to initially tend towards the nearer wall. In the false fold cases, the flow between the jet and the nearest vocal tract wall is theorized to be substantially slower than in the vocal tract cases. Due to the obstructing influence of the inferior false fold surface, there is no outlet for the flow

towards the nearest wall. As the velocity decreases in this region, a corresponding increase in pressure is predicted; this would tend to force the jet away from the wall toward the vocal tract midplane. An interesting experiment would be to see at what value of vertical gap between the inferior false fold surface and the glottal exit the jet transitions from skewing towards the nearest wall to skewing away from the nearer wall. Symmetric positioning of the vocal tract, with and without false folds, created jet centerline patterns that were generally similar to the open jet case.

Finally, the magnitude of the RMS velocity was calculated from PIV measurements. Distinct regions of jet core (with relatively low |RMS| values) and shear layer (with relatively high |RMS| values) were evident close to the glottal exit. Farther downstream, the |RMS| values increased and the jet core disappeared. The vocal tract cases showed higher |RMS| values than the open jet case, and at higher pressures were less likely to display distinct shear layers. When the false folds were included in the vocal tract, the |RMS| values decreased to more closely match the open jet case. This suggests that the false folds have a stabilizing influence on the fluctuating glottal jet velocities in the vocal tract. This could be either due to direct stabilization of the jet, or indirectly by possible stabilization of the glottal geometry during vibration (since it is possible that fluctuations seen in the jet arose due to slight variations in the vocal fold model position).

5 Discussion and Conclusions

The synthetic vocal fold model introduced by Thomson (2004) was tested to determine its behavior under a variety of different test conditions. The model's material properties were measured, as were relationships between frequency, time-averaged flow rate and mean sub-glottal pressure. The influence of sub-glottal tube length on model behavior was evaluated. The glottal jet of a two-layer model was characterized using high-speed imaging and particle image velocimetry (PIV) for three distinct physical arrangements: an open jet, a vocal tract without false folds, and a vocal tract with false folds. In addition to the physical insight gained using these synthetic models, the results of these measurements have also provided insight as to how to refine the synthetic model for future experiments.

5.1 Main Contributions

Two-layer synthetic vocal fold models with fibers added to the silicone matrix were observed to vibrate at frequencies independent of sub-glottal acoustics. This effect was still correlated with sub-glottal tube length. However, the presence of fibers in the model matrix dramatically increased the degree of independence.

Concerning the glottal jet, this thesis research offers three contributions:

- The presence of the false folds obstructed convection of starting vortex lobes farther downstream than the inferior surface of the false folds. This was observed in the symmetric case as obstruction (or possibly squeezing) of the starting vortex side lobes into the jet core, and in asymmetric cases as restraining of the side lobe nearest a false fold. While these vortex velocities were small, the vortices are nevertheless coherent structures which interact with the surrounding boundaries and influence the glottal sound source.

- In the presence of asymmetry in the positioning of the vocal tract without false folds with respect to the vocal fold model, the resulting glottal jet skewed towards the nearest vocal tract wall, particularly as the jet initially developed. However, when the false folds were added to the vocal tract, this trend was reversed and the glottal jet skewed away from the nearest wall and towards the vocal tract centerline.

- The magnitudes of the RMS velocities (|RMS|) were higher for the vocal tract cases than for the open jet case. The |RMS| values decreased when the false folds were included in the vocal tract, suggesting that the false folds may have a stabilizing influence on the fluctuating velocities in the glottal jet.

5.2   One-layer Model vs. Two-layer Model

The current one-layer model was compared to the new two-layer model. The addition of a second "cover" layer was thought to more closely match real vocal fold physiology and would better support the propagation of a mucosal surface wave from the inferior to the superior direction of the medial surfaces. The two-layer model displayed differences in its relationship between maximum lateral glottal displacement and sub-glottal pressure when compared to the one-layer model. Synthetic model materials (see Chapter 3, Sections 3.1.1 and 3.4.6) with the presence of fibers can introduce non-linear stress-strain behavior to the model. Further studies on the influence of fibers in the model body layer on model vibration should be pursued.

Zhang et al. (2006b) found that a restraining plate placed over the superior surface of the vocal fold model, except near the edge of the medial surface, enabled the development of medial surface wave in the inferior-superior direction. New experiments might explore the possibility of increasing the body layer modulus, effectively restraining its vertical motion, while using a much softer cover layer modulus (e.g. 1:1:4 or 5). The cover layer may need to be thickened to prevent accidental damage to the model as pressures are increased.

The addition of acrylic fibers to the body layer may have the same restraining effect, which enabled model M1 (see Table 3-3) to vibrate at frequencies independent of sub-glottal resonances. This should be further studied with a larger number of models and over more realistic phonation conditions such as shorter tube lengths and including the additional acoustic resonators of the vocal tract and false folds.

It is curious that the M1 model converged to a particular frequency value (~100 Hz) as pressure was increased for a variety of sub-glottal tube lengths (see Figure 3-24). It may be that the acoustics of the sub-glottal system influence a kind of frequency boundary condition.

Cross modes (e.g., modes based on dimensions on the order of tube diameter) of the sub-glottal tube system are more likely as the sub-glottal tube length gets shorter and shorter. This would complicate the upstream acoustic system. Tests were performed for a realistic length human trachea (17 cm), and the pressures were very high to get the models tested to phonate. Zhang et al. (2006a) also found this to be case. Further investigation of optimal model material properties that would facilitate self-oscillation at more realistic sub-glottal pressures and tube lengths is recommended.

5.3   Glottal Jet Measurements

The lateral and inferior-superior motion of the vocal fold model viewed using high-speed imaging should be compared with real vocal fold motion. In particular, the changing profile of the uppermost vocal fold surface as viewed from the sagittal view, as well as the collision and rebound of the medial vocal fold surfaces as viewed from the superior view, should be investigated. Also, the extent to which adhesion plays a role in normal use of the real vocal folds is not well understood.

The presence of the vocal tract enhances mixing, particularly as the jet gets closer to tract walls. Studies on the possible acoustic consequences of vortex suppression by the false folds should be examined. Also, the new vortices formed off the leading edge of the

false folds and the recirculation patterns near the glottal exit could be included in the analysis.

Perhaps the false vocal folds act to restrain the real vocal folds in some way. Experiments need to be done to see if a model fixtured with a set of false folds is in any way less acoustically dependent on sub-glottal geometry, or if the false folds influence the model vibration. Also, acoustic studies should be conducted to measure the general difference in sound generation between the three test arrangements (i.e. open jet, vocal tract, false folds).

The models tested in this thesis do not appear to display any bi-modal flapping behavior. It is suggested that this is due to a large divergent exit profile ($>= 40°$), which Erath and Plesniak (2006b) stated never reattached to a wall. The models glottal exit profile is so divergent that the flow separates out of view of the camera and never/rarely reattaches.

6   References

Agarwal, M., Scherer, R., and Hollien , H. (**2003**). "The False Vocal Folds: Shape and Size in Frontal View During Phonation Based on Laminagraphic Tracings," J. Voice **17** (2), 97-113.

Alipour, F., and Scherer, R. (**1995**). "Pulsatile airflow during phonation: An excised larynx model," J. Acoust. Soc. Am. **97**, 1241-1248.

Alipour, F., Scherer, R., and Knowles, J. (**1996**). ''Velocity distributions in glottal models,'' J. Voice **10** (1), 50–58.

Alipour, F., and Scherer, R. (**2001**). "Effects of oscillation of a mechanical hemilarynx model on mean transglottal pressure and flows," J. Acoust. Soc. Am. **110**, 1562-1569.

Alipour, F., and Scherer, R. (**2006**). "Characterizing glottal jet turbulence," J. Acoust. Soc. Am. **119**, 1063-1073.

Barney, A., Shadle, C., and Davies, P. (**1999**). "Fluid flow in a dynamic mechanical model of the vocal folds and tract. I. Measurements and theory," J. Acoust. Soc. Am. **105**, 444-455.

Chan, R., and Titze, I. (**1997**). "Further studies of phonation threshold pressure in a physical model of the vocal fold mucosa," J. Acoust. Soc. Am. **101**, 3722-3727.

Chan, R., and Titze, I. (**2006**). "Dependence of phonation threshold pressure on vocal tract acoustics and vocal fold tissue mechanics," J. Acoust. Soc. Am. **119**, 2351-2362.

Doellinger, M., Berry, D., and Berke, G. (**2005**). "Medial surface dynamics of an *in-vivo* canine vocal fold during phonation," J. Acoust. Soc. Am. **117**, 3174-3183.

113

Drechsel, J., Munger, J., Pulsipher, A., and Thomson, S. (**2007a)**. "Development and response of materially-nonlinear, multi-layer synthetic models of the human vocal folds," technical presentation, *ASME 2007 Summer Bioengineering Conference*, June 20-24 2007, Keystone, CO.

Drechsel, J., Hamilton, B., Jepsen, A., Munger, J., Pickup, B., Pulsipher, A., and Thomson, S. (**2007b**). "Multi-component synthetic model of the human larynx for investigating laryngeal fluid-structure interactions," technical presentation, *153rd Meeting of the Acoustical Society of America*, June 4-8 2007, Salt Lake City, UT.

Erath, B., and Plesniak, M. (**2006a**). "An investigation of bimodal jet trajectory in flow through scaled models of the human vocal tract," Exp. Fluids. **40**, 683-696.

Erath, B., and Plesniak, M. (**2006b**). "The occurrence of the Coanda effect in pulsatile flow through static models of the human vocal folds," J. Acoust. Soc. Am. **120**, 1000-1011.

Erath, B., and Plesniak, M. (**2006c**). "An investigation of jet trajectory in flow through scaled vocal fold models with asymmetric glottal passages," Exp. Fluids. **41**, 735-748.

Fishbane, P., Gasiorowicz, S., and Thornton, S. (**1993**). *Physics for Scientists and Engineers*, extended version, 1st printing, Prentice-Hall.

Hirano, M., and Kakita, Y. (**1985**). "Cover-body theory of vocal fold vibration," in *Speech Science: Recent Advances*, edited by R. G. Daniloff, College-Hill Press, San Diego, **pp. 1–46**.

Kaiser, J. (**1983**). "Some Observations on Vocal Tract Operation from a Fluid Point of View," *Vocal Fold Physiology: Biomechanics, Acoustics, and Phonatory Control*, edited by I. Titze & R. Scherer, Denver Center for the Performing Arts, Denver CO, **pp. 358**.

Khosla, S., Muruguppan, S., Gutmark, E., and Scherer, R. (**2007**). "Vortical flow field during phonation in an excised canine larynx model," Annals of Otology, Rhinology & Laryngology, **116** (3), 217-228.

Lucero, J. (**1996**). "Relationship between the phonation threshold pressure and the prephonatory glottal width in a rectangular glottis*,"* J. Acoust. Soc. Am. **100**, 2551-2554.

Lucero, J. (**1998**). "Optimal glottal configuration for ease of phonation," J. Voice **12** (2), 151-158.

Mongeau, L., Franchek, N., Coker, C., and Kubli, R. (**1997**). "Characteristics of a pulsating jet through a small modulated orifice, with application to voice production*,"* J. Acoust. Soc. Am. **102**, 1121-1133.

Neubauer, J., Zhang, Z., Miraghaie, R., and Berry, D. (**2007**). "Coherent structures of the near field flow in a self-oscillating physical model of the vocal folds*,"* J. Acoust. Soc. Am. **121**, 1102-1118.

Riede, T., Tokuda, I., Munger, J., and Thomson, S. "On the potential acoustic role of mammalian laryngeal air sacs," in review, J. Exp. Bio.

Scherer, R. C. (**1981**). ''Laryngeal fluid mechanics: steady flow considerations using static models,'' Ph.D. Thesis, University of Iowa, Iowa City.

Scherer, R., Titze, I., and Curtis, J. (**1983**). "Pressure-flow relationships in two models of the larynx having rectangular glottal shapes," J. Acoust. Soc. Am. **73**, 668–676.

Scherer, R., Shinwari, D., De Witt, K., Zhang, C., Kucinschi B., and Afjeh, A. (**2001**). "Intraglottal pressure profiles for a symmetric and oblique glottis with a divergence angle of 10 degrees," J. Acoust. Soc. Am. **109**, 1616–1630.

Shadle, C., Barney, A., and Thomas, D. (**1991**). "An Investigation into the Acoustics and Aerodynamics of the Larynx," *Vocal Fold Physiology: Acoustic, Perceptual, and Physiological Aspects of Voice Mechanisms*, edited by J. Gauffin & B. Hammarberg, Singular Publishing Group, Inc., San Diego CA, **pp. 78-80**.

Shadle, C., Barney, A., and Davies, P. (**1999**). "Fluid flow in a dynamic mechanical model of the vocal folds and tract. II. Implications for speech production studies," J. Acoust. Soc. Am. **105**, 456-466.

Shaw, H., and Deliyski, D. "Mucosal Wave: A Normophonic Study Across Visualization Techniques," in press, J. Voice.

Shinwari, D., Scherer, R., DeWitt, K., and Afjeh, A. (**2003**). "Flow visualization and pressure distributions in a model of the glottis with a symmetric and oblique divergent angle of 10 degrees," J. Acoust. Soc. Am. **113**, 487-497.

Thomson, S. (**2004**). "Fluid-structure interactions within the human larynx," Ph.D. dissertation, Purdue University, West Lafayette, Indiana.

Thomson, S., Mongeau, L., and Frankel, S. (**2005**). "Aerodynamic transfer of energy to the vocal folds*,"* J. Acoust. Soc. Am. **118**, 1689-1700.

Titze, I., Schmidt, S., and Titze, M. (**1995**). "Phonation threshold pressure in a physical model of the vocal fold mucosa," J. Acoust. Soc. Am. **97**, 3080-3084.

Verdolini-Marston, K., Titze, I., and Druker, D. (**1990**). "Changes in phonation threshold pressure with induced conditions of hydration," J. Voice **4** (2), 142-151.

Verdolini-Marston, K., Sandage, M., and Titze, I. (**1994**). "Effect of hydration treatments on laryngeal nodules and polyps and related voice measures," J. Voice **8** (1), 30-47.

Zhang, Z., Mongeau, L., and Frankel, S. (**2002**). "Experimental verification of the quasi-steady approximation for aerodynamic sound generation by pulsating jets in tubes," J. Acoust. Soc. Am. **112**, 1652-1663.

Zhang, Z., Mongeau, L., Frankel, S., Thomson, S., and Park, J. (**2004**). "Sound generation by steady flow through glottis-shaped orifices," J. Acoust. Soc. Am. **116**, 1720-1728.

Zhang, Z., Neubauer, J., and Berry, D. (**2006a**). "The influence of subglottal acoustics on laboratory models of phonation," J. Acoust. Soc. Am. **120,** 1558-1569.

Zhang, Z., Neubauer, J., and Berry, D. (**2006b**). "Aerodynamically and acoustically driven modes of vibration in a physical model of the vocal folds," J. Acoust. Soc. Am. **120,** 2841-2849.

APPENDICES

A.   Drawings and Schematics

This appendix contains pertinent drawings and schematics of test setup components and test-related equipment that was developed specifically for this thesis research. In particular, the inexpensive phase-locking triggering circuit built for this thesis research has proven to work extremely well, and replaced equipment that cost thousands of dollars.

Triggering:

Figure A-1   Triggering circuit built to phase-lock PIV measurements with model vibration.

Triggering: (continued)
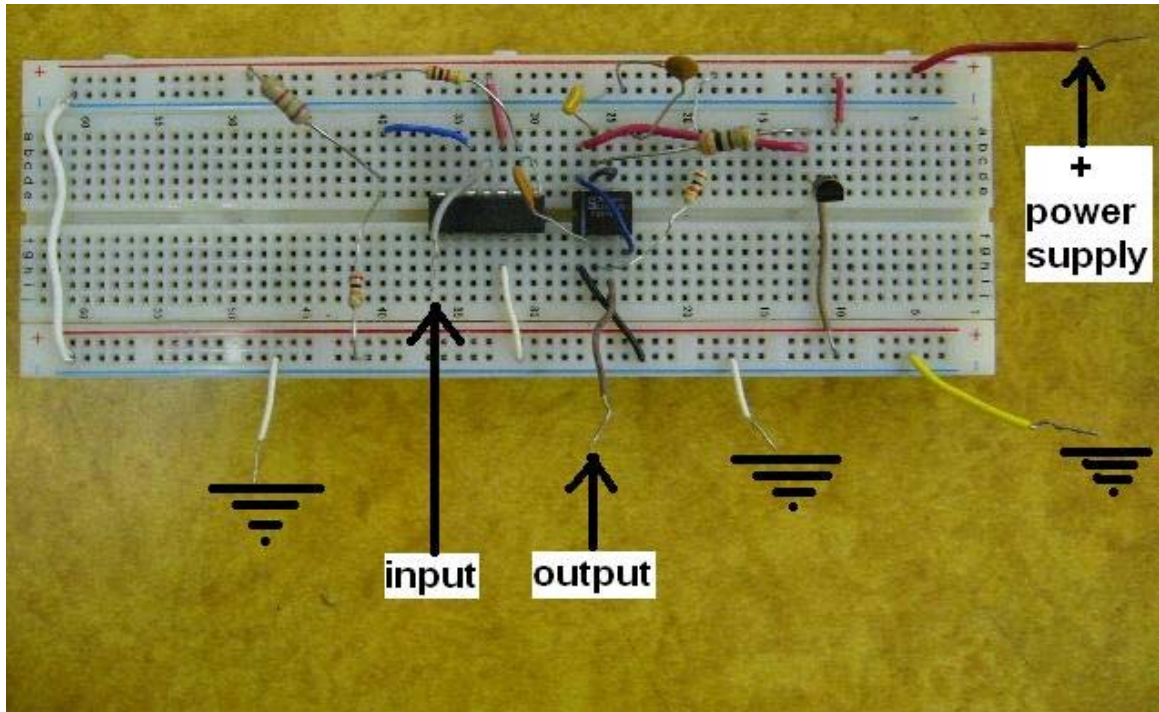
Figure A-2 Phase-locked triggering circuit used in PIV measurements.
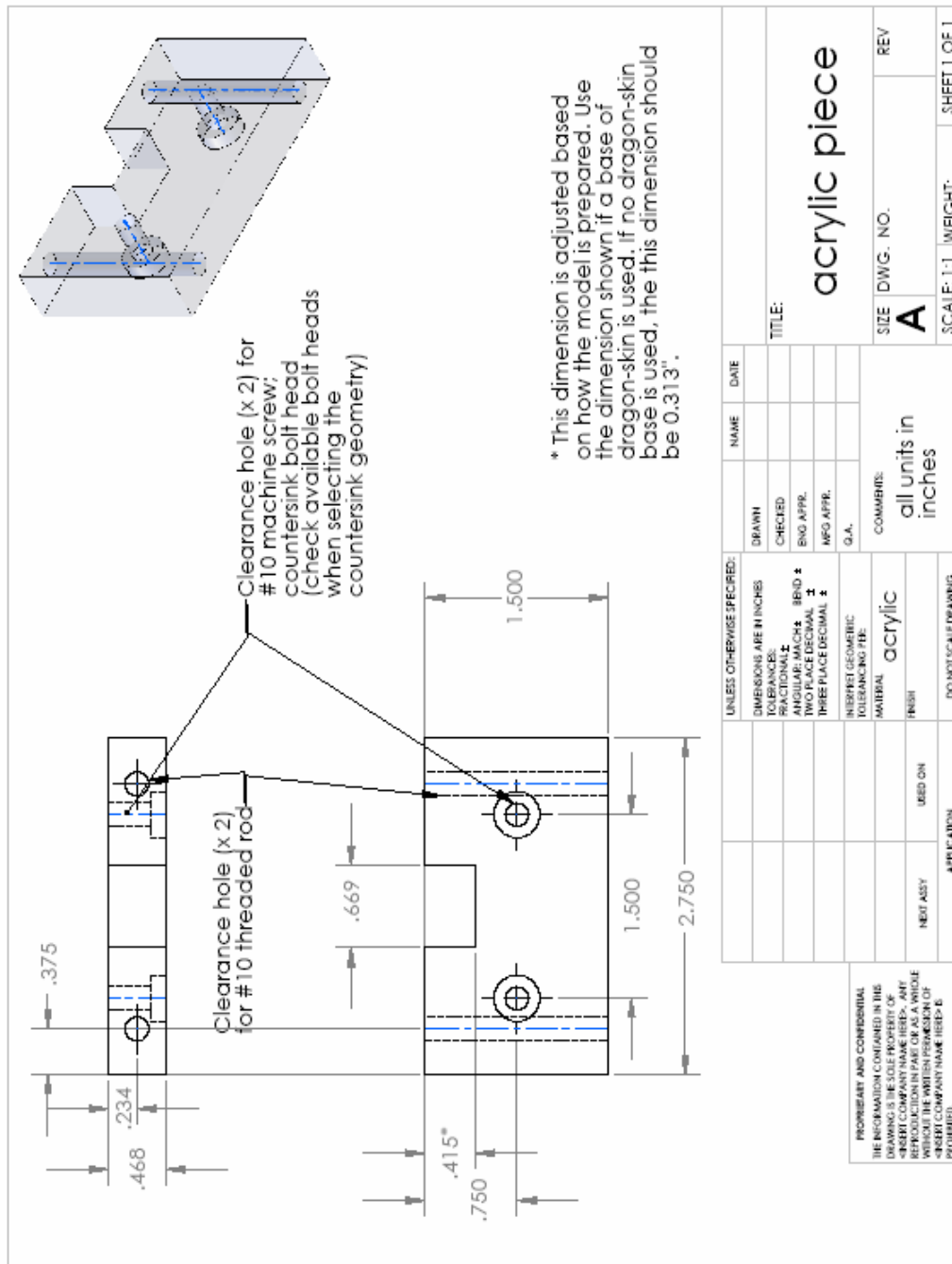
Figure A-3 Drawing of acrylic piece used in Test Fixture B to fixture synthetic vocal fold model.
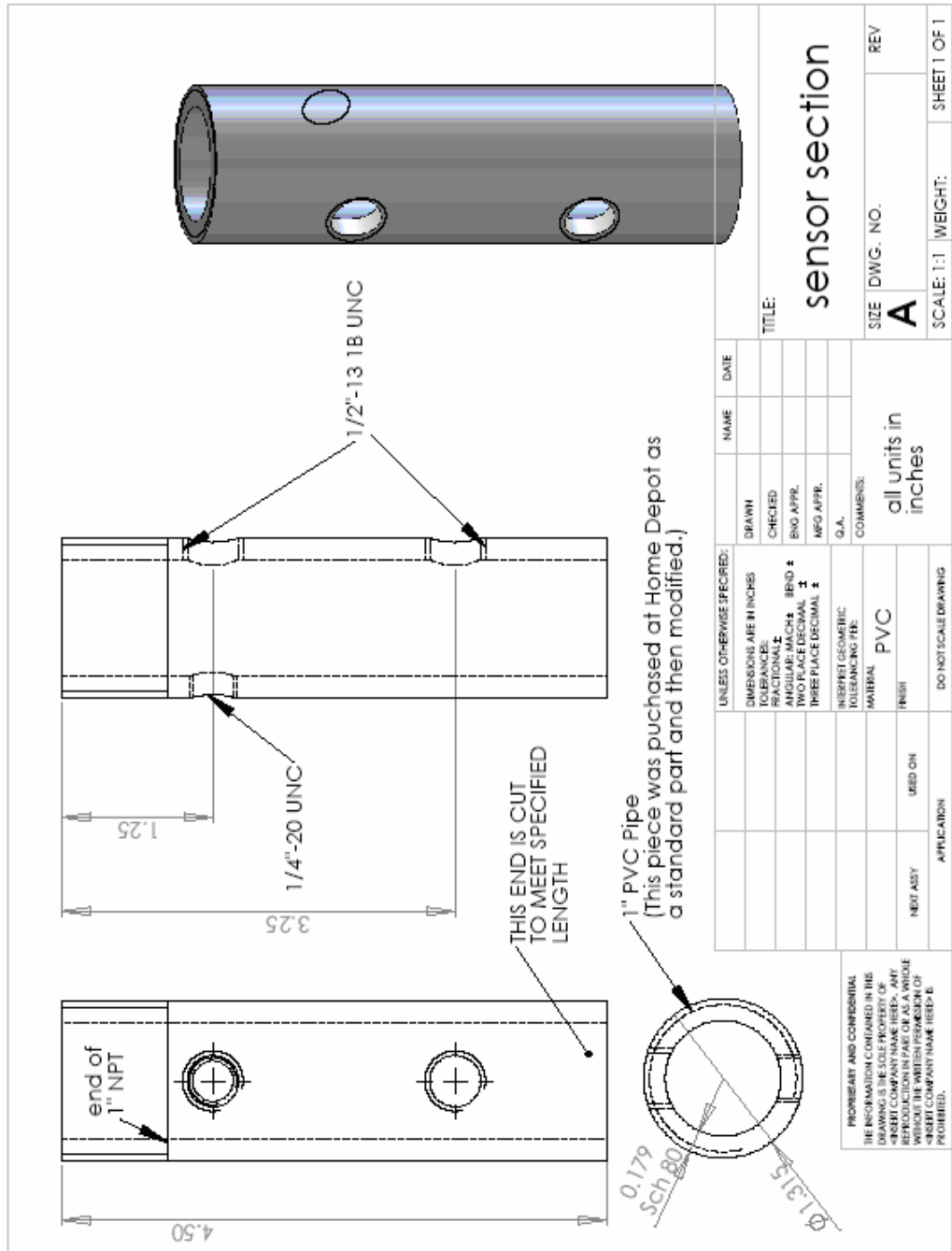
Figure A-4 Drawing of cylindrical sub-glottal duct used in Test Fixture B.
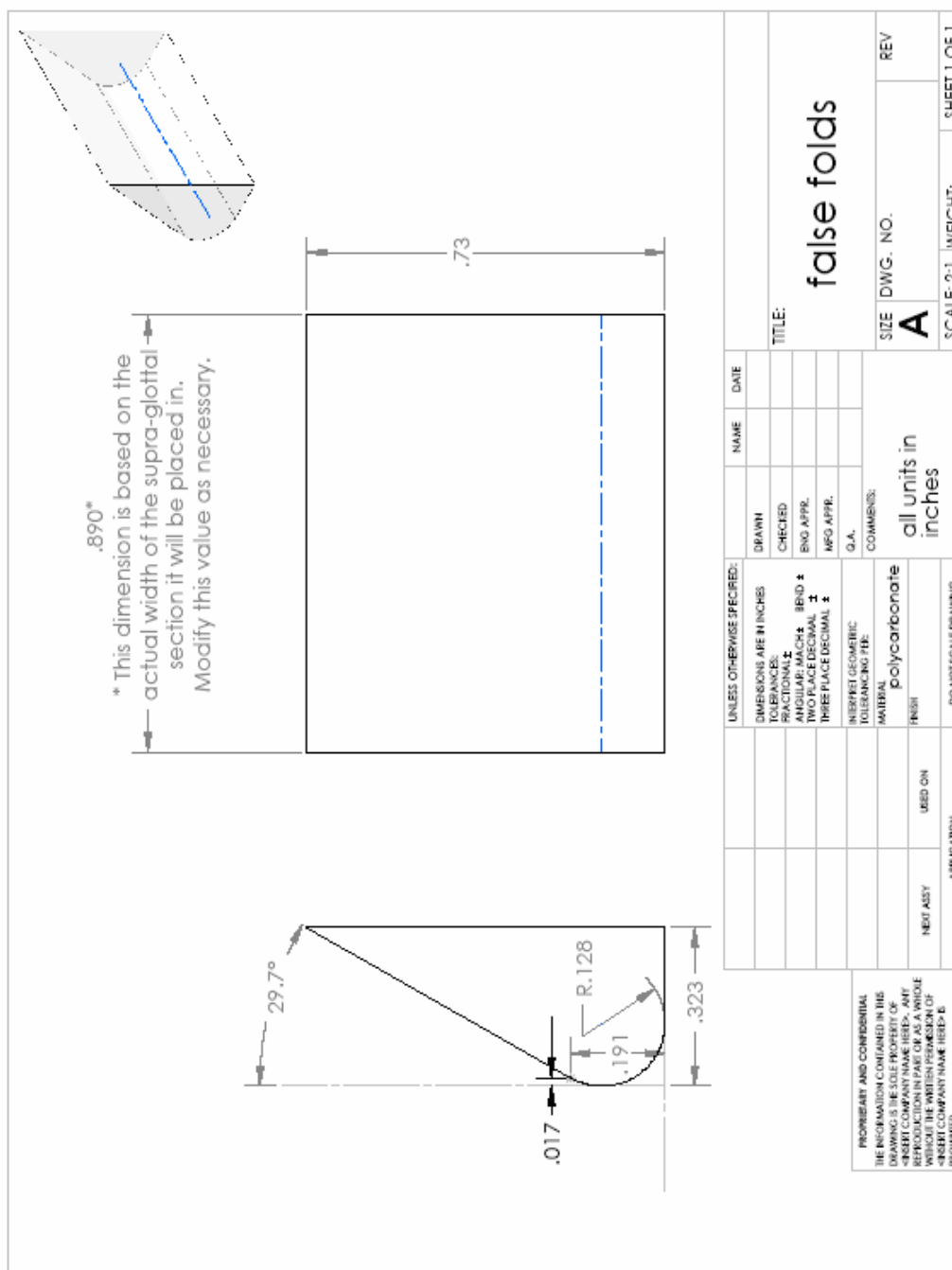
Figure A-5 Drawing of false vocal fold model used in Chapter 4.
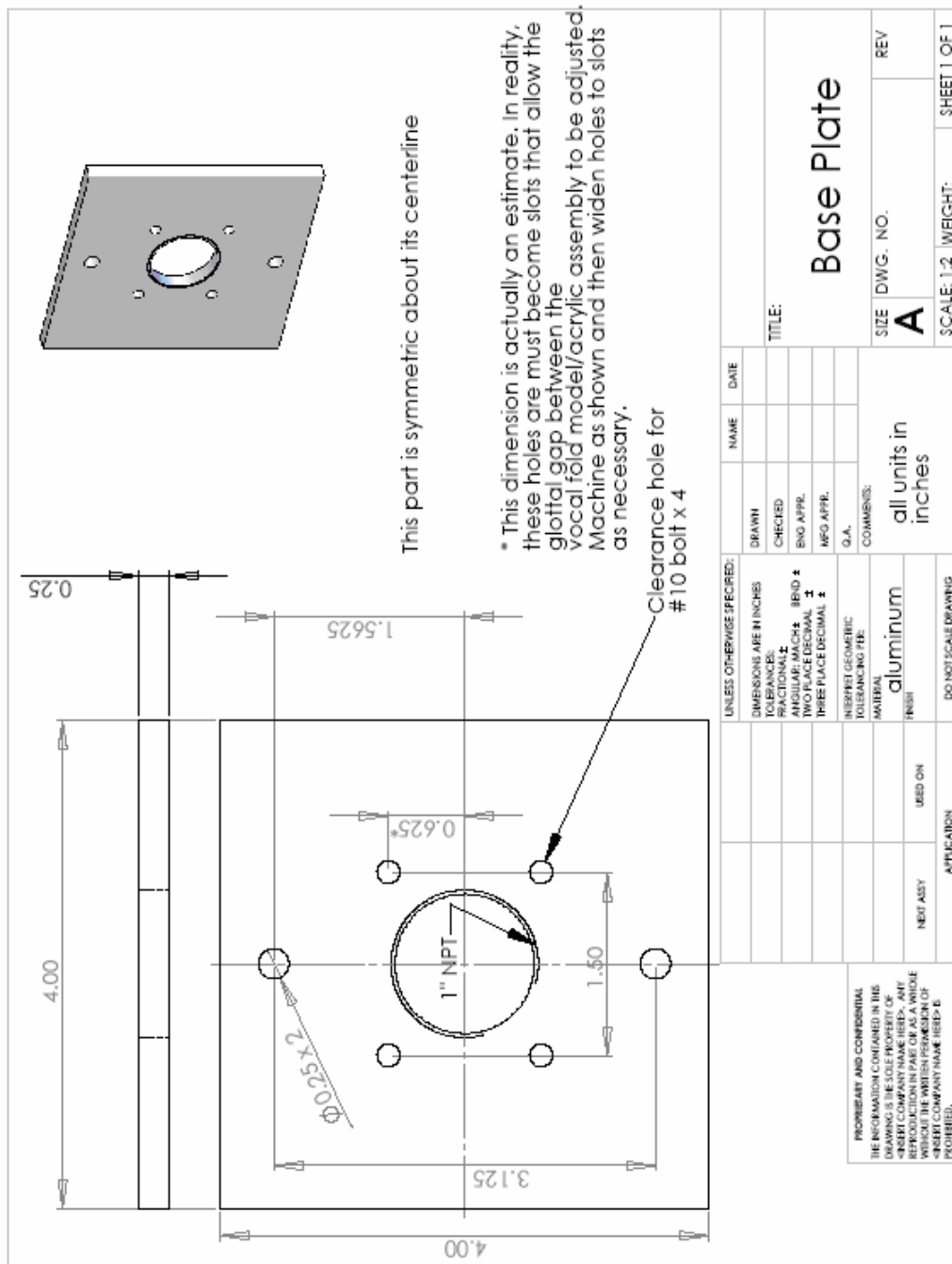
Figure A-6 Drawing of base plate used in Test Fixture B.
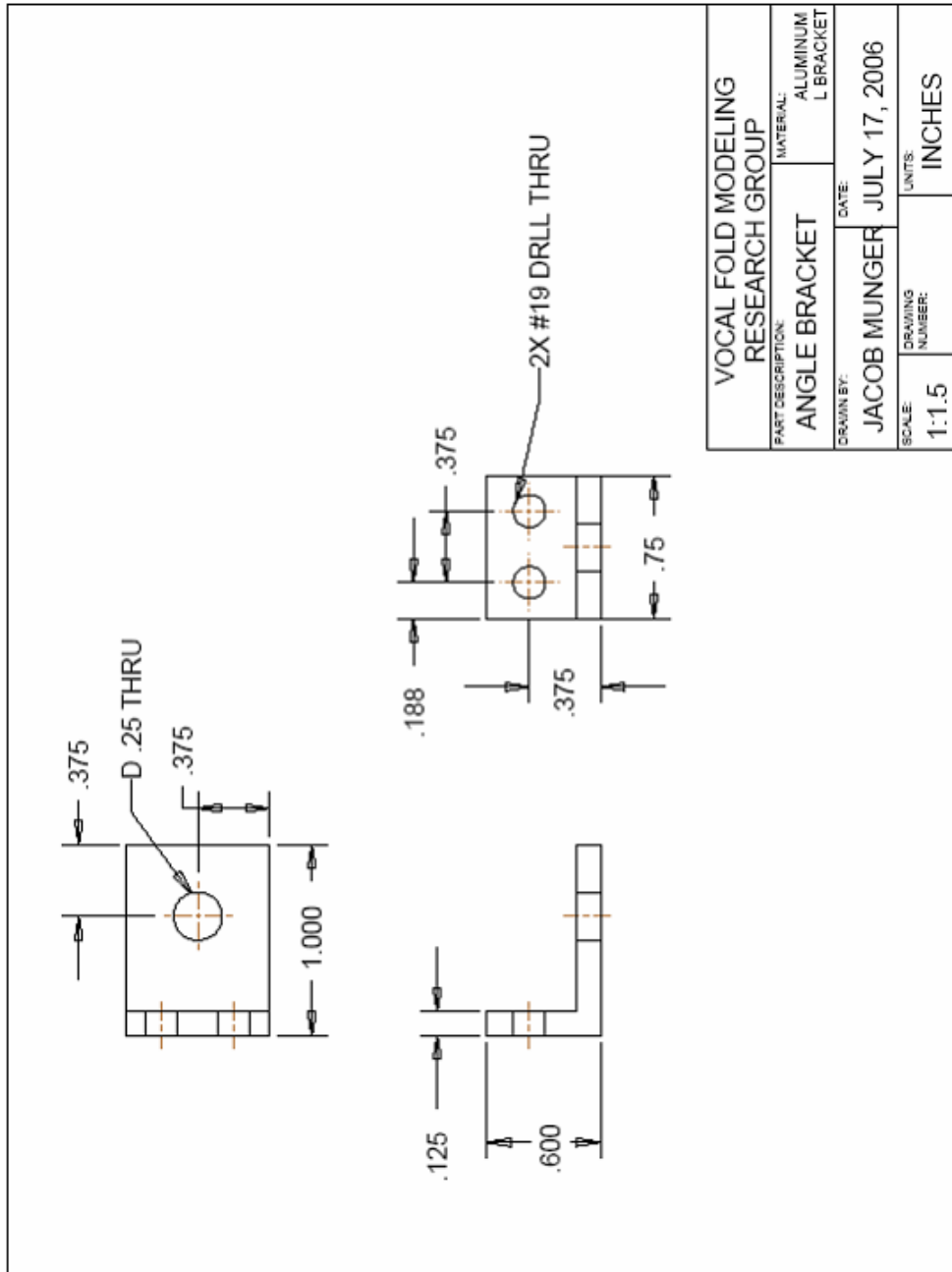
Figure A-7 Angle bracket used on vocal tract model.
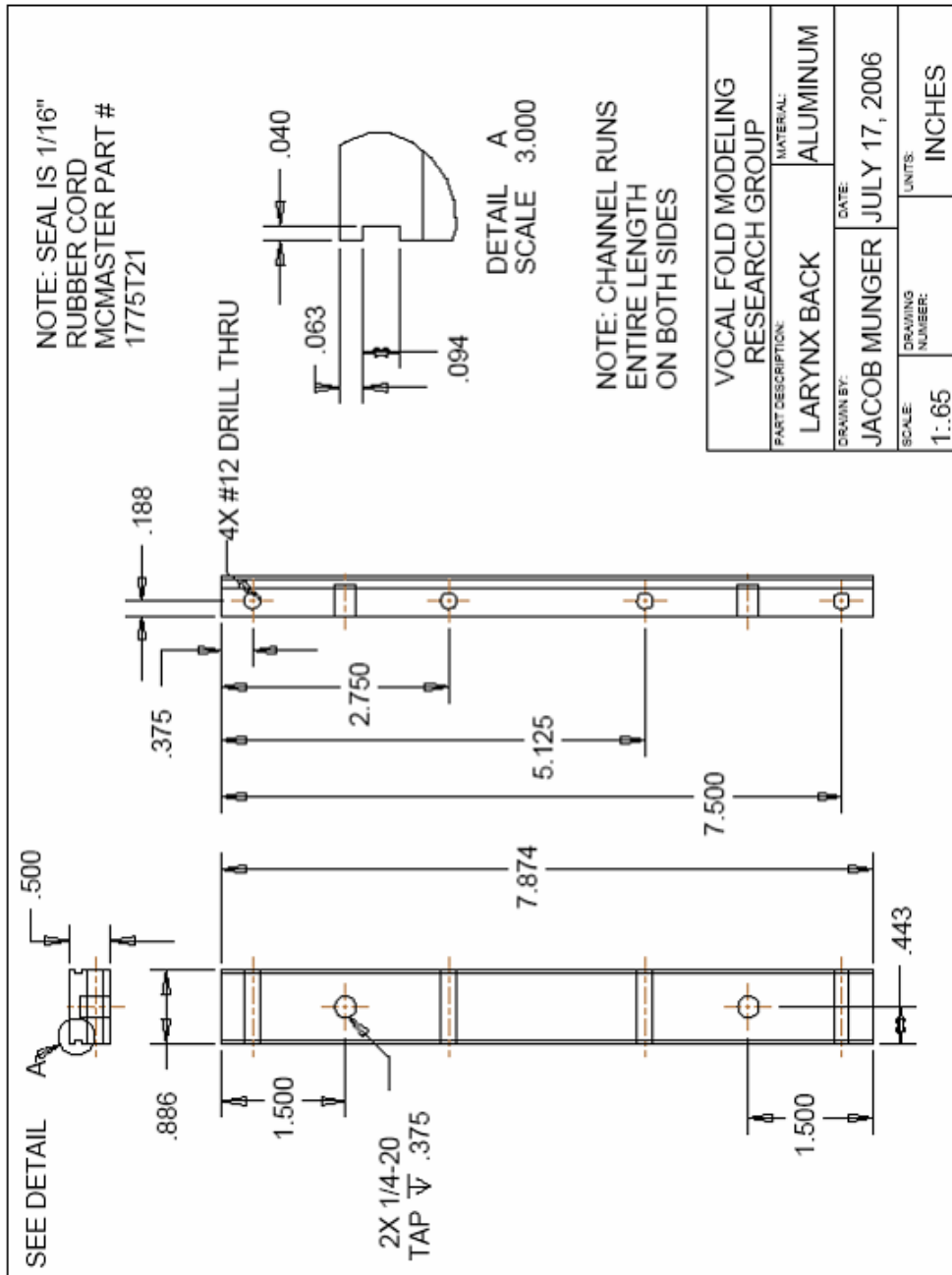
Figure A-8 Back (opposite of glass side) of vocal tract.
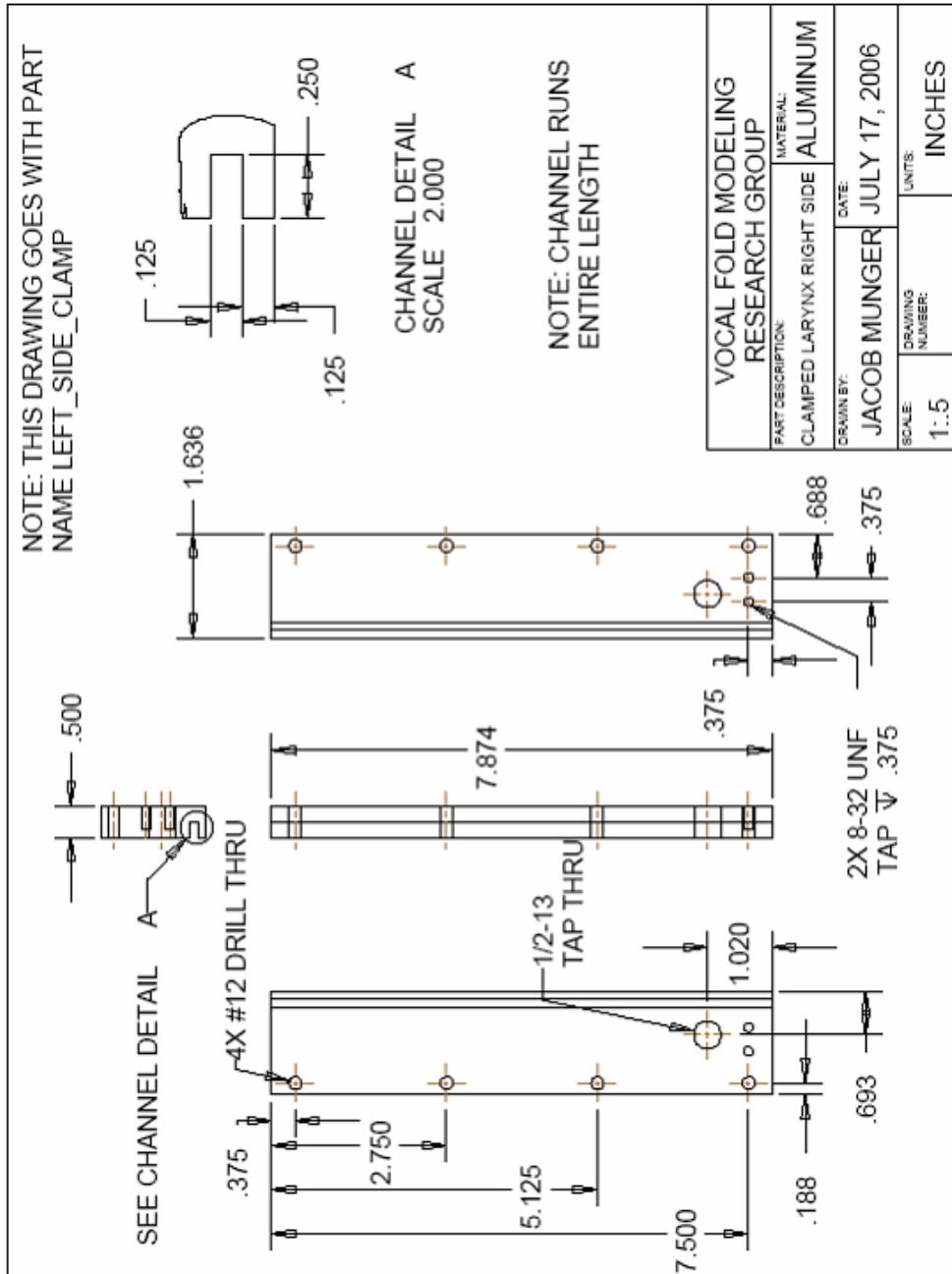
Figure A-9 Right side of vocal tract.
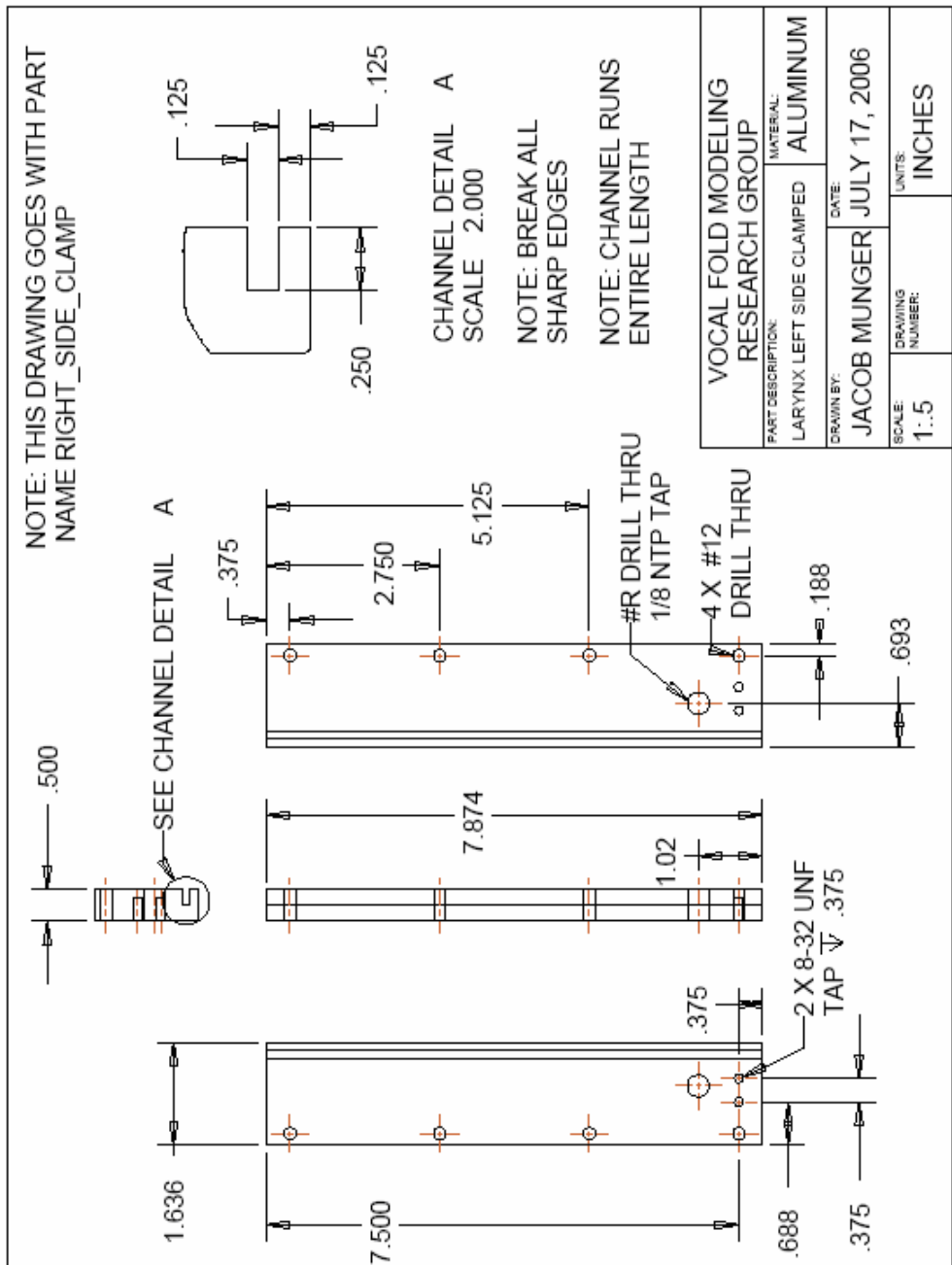
Figure A-10 Left side of vocal tract.
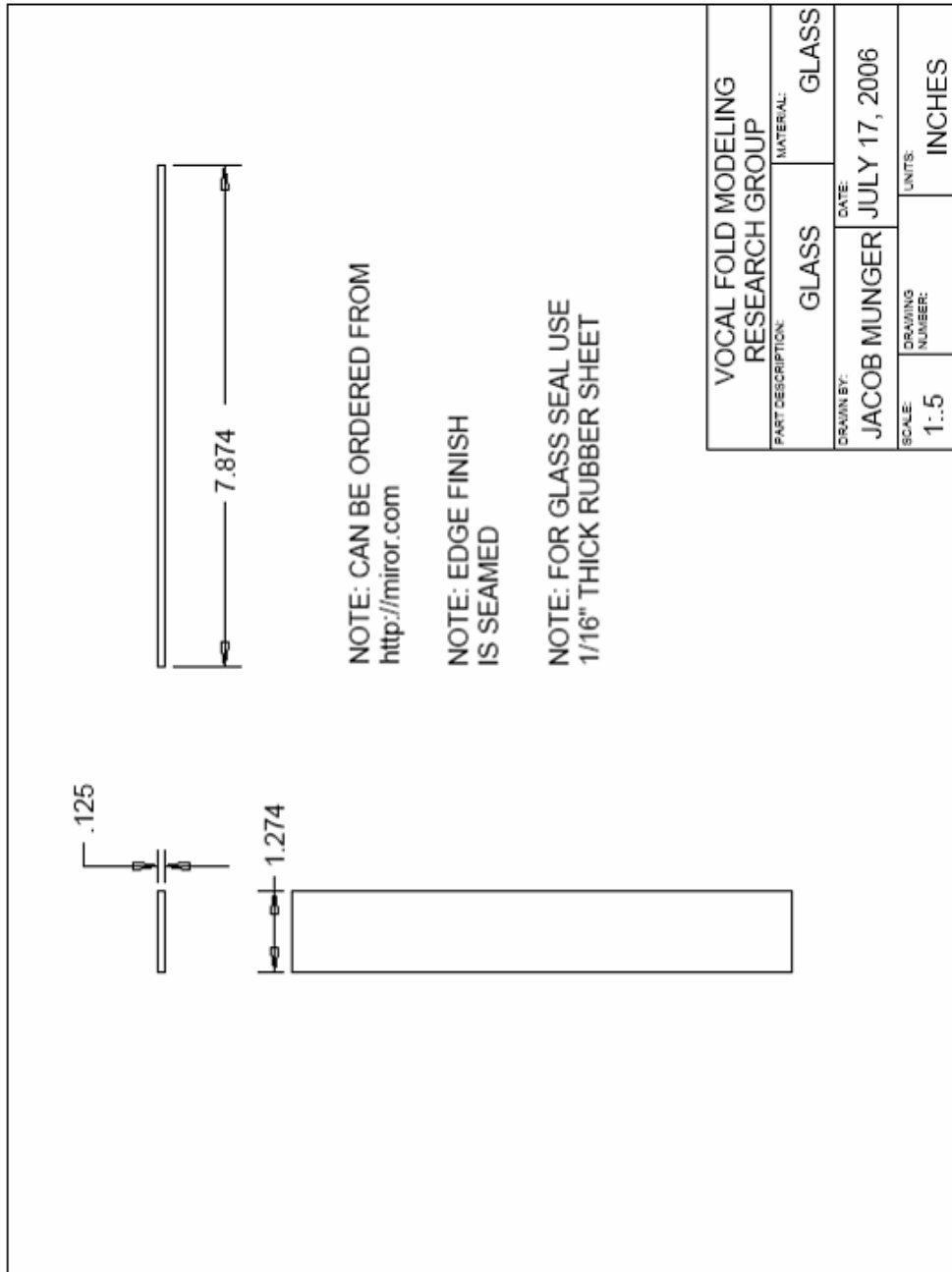
Figure A-11 Glass used as front side of vocal tract.

B.   MATLAB and LabVIEW Code

This appendix contains three MATLAB codes. Two of them are used in conjunction to identify the jet core centerline of PIV-measured velocity fields: PIVthesis.m, and PRmod.m. PIVthesis.m is the primary user interface, and all required inputs for running the analysis are controlled in this m-file. PRmod.m contains the actual jet centerline-finding algorithm (described in Chapter 4, Section 4.5.2). The third MATLAB code is a sample used to extract length information from .avi and image files. Finally, two LabVIEW VI's developed for this research to monitor and acquire the pressure and frequency data are included. The first was used to measure frequency and pressure data used in Chapter 3. The second was used to monitor model frequency, sub-glottal pressure, and the corresponding phase-locking trigger signal sent to the PIV hardware during PIV measurements presented in Chapter 4.

B.1 MATLAB Code for Calculating Jet Core Centerline (see Section 4.5.2)

B.1.1 PIVthesis.m

```
%   PIVthesis.m
%
%   For Sets 6-8
%
%   1-  loads PIV data
%   2-  creates a various plots based on the PIV data. Uses MATLAB
curve fitting tools
%       to improve the velocity vector info that is used to find the
jet angle.
%   3-  calls on PIVmod.m to do most of these operations.
%
%   By:     Dr. Thomson & James Drechsel
%   Date:   17May07
%

clc;
clf;
clear all;
warning on

% one time inputs for Set info...
S={'7'};            % INPUT: Set # (for loading file)
name={'ave'};       % INPUT: Set type
nameRMS={'rms'};
nameTKE={'tke'};
f=270;              % INPUT: # of different files
ph=30;              % INPUT: # of phases
P=[1.25 1.5 1.9];   % INPUT: different pressures used, [kPa]
yp=1:110;           % INPUT: y-plane array value at which to perform
analysis, [index] (1 = farthest away from VF model, 172 = nearest VF
model)
jc_crit=1;          % INPUT: criteria for changing the turb. intensity
comparison point
                    % select "1" for point to always be above glottal jet
origin
if jc_crit==1
    jc=ones(f/ph)*172/2;    % INPUT: location of center of jet, [x-
index]
else
    posi=[86-30 86-15 86 86+15 86+30];     % INPUT: fixed position in
duct, regardless of how the duct is positioned, [index]
end
js=ones(1,f/ph)*12; % possible INPUT: phase at which jet starts...
caseS=1;            % INPUT: starting case #
caseE=9;            % INPUT: ending case #
s_ave=5;            % INPUT: ±index value to look around a selected point
(e.g. tip, or max V)
hori=15;            % INPUT: ±index value to calculate average t.i.
```

```
ALIPOUR=0;           % INPUT: determines how turbulent intensity is
averaged

% select "1" to average over a ±s_ave square around "tip"
                     % select "0" to average along each vertical row of
vectors
tip=s_ave+min(yp):max(yp)-s_ave;% INPUT: y-point (vertical distance) to
evaluate turbulent intensity


% changing parameters for Set evaluation
Percent=0.8;         % INPUT: % of max V; use velocities above this value
to find jet core, [0->1]
Thresh=7;            % INPUT: cut-off velocity value, below which to
ignore velocities, [m/s]
buf=10;              % INPUT: buffer to improve resample() function
results, [index]
BadLim=20;           % INPUT: # of acceptable bad jet center values for
simple deletion (keep this number kind of small), [#]
sca=0.50;            % INPUT: when G==2, scaling value for 2-D plots to
prevent overlap (lower#=>less overlap)


% inputs to change plotting and other outputs
L=0;                 % INPUT: select "1" to see each jet individually
Pau=0;               % INPUT: select "1" to pause between different phases
when using L
L2=0;                % INPUT: select "1" to see how many cases remain
displayed
G=2;                 % INPUT: select "1" to see mesh plot output
                     %   "    select "2" to see jet angle plots (jc_crit
must = 1)
                     %   "    select "3" to see velocity field and jet
centerline with select velocity profile plots
                     %   "    select "4" to see max velocity surface plot
                     %   "    select "5" to see turbulent intensity plots
                     %   "    select "6" to see jet centerline velocity
surface plots
ExPlot=2;            % INPUT: select "1" to export velocity field and with
jet centerline overlaid
                     %       : select "2" to export 2D phase vs. jet angle
plots
                     %       : select "3" to export both
                     %       : select "4" to export turbulence intensity
images: downstream vs. phase
                     %       : select "5" to export turbulence intensity
images: spatial distribution
                     %       : select "6" to export jet centerline velocity
plots

bufx=ones(1,f/ph);% buffer to exclude far left x values, [index]
if str2num(char(S))==6
    bufx(1)=15;          % duct, L1
    bufx(2)=30;          % duct, L2
    bufx(4)=15;          % duct, R1
    bufx(5)=30;          % duct, R2
    bufx(6)=20;          % false, L
    bufx(8)=15;          % false, R
```

```
        tab=[6,1,9;
             7,3,9;
             8,4,9];
        tab_duct=[2,1,3,4,5];
        tab_fvf=[6,7,8];
        if jc_crit~=1
            jc=[posi(2) posi(1) posi(3) posi(4) posi(5) posi(2) posi(3)
posi(4) posi(3)];
        end
        ord={'DL1' 'DL2' 'DC' 'DR1' 'DR2' 'FL' 'FC' 'FR' 'ND'};
elseif str2num(char(S))==7
        bufx(1)=15;         % false, L
        bufx(2)=5;          % false, C
        bufx(3)=19;         % false, R
        bufx(4)=30;         % duct, L2
        bufx(5)=15;         % duct, L1
        bufx(6)=10;
        bufx(7)=15;         % duct, R1
        bufx(8)=30;         % duct, R2
        tab=[1,5,9;
             2,6,9;
             3,7,9];
        tab_duct=[4,5,6,7,8];
        tab_fvf=[1,2,3];
        if jc_crit~=1
            jc=[posi(2) posi(3) posi(4) posi(1) posi(2) posi(3) posi(4)
posi(5) posi(3)];
        end
        ord={'FL' 'FC' 'FR' 'DL2' 'DL1' 'DC' 'DR1' 'DR2' 'ND'};
elseif str2num(char(S))==8
        bufx(1)=15;         % false, L
        bufx(3)=15;         % false, R
        bufx(5)=5;          % duct, C
        bufx(6)=15;         % duct, L1
        bufx(7)=15;         % duct, R1
        bufx(8)=30;         % duct, R2
        bufx(9)=35;         % duct, L2
        tab=[1,6,4;
             2,5,4;
             3,7,4];
        tab_duct=[9,6,5,7,8];
        tab_fvf=[1,2,3];
        if jc_crit~=1
            jc=[posi(2) posi(3) posi(4) posi(3) posi(3) posi(2) posi(4)
posi(5) posi(1)];
        end
        ord={'FL' 'FC' 'FR' 'ND' 'DC' 'DL1' 'DR1' 'DR2' 'DL2'};
end


% flow-rate, frequency, and measured pressure
fvf_data=[0.16527   133.2   1.14;       % [time-averaged flow rate,
[scfm]
          0.21824   132.3   1.29;       % frequency, [Hz]
          0.31660   132.8   1.55;       % sub-glottal pressure, [kPa]]
          0.49229   135     1.95];
```

```matlab
% non-dimensional parameters
nu=1.5e-5;                              % kinematic viscosity of air @ STP,
[m^2/s]
Ag=[.078686 .10068 .3552];           % max. glottal area, [cm^2]
Um=((fvf_data(2:end,1)*.000471947)./(Ag'/10000))';   % mean glottal
velocity, [m/s]
Gp=[3.7787 3.7802 3.8225];           % glottal perimeter @ max area,
[cm]
Dh=4.*Ag./Gp;                           % hydraulic diameter, [cm]
Re=Um.*(Dh/100)./nu;                 % Reynolds #
St=fvf_data(2:end,2)'.*(Dh/100)./Um;% Strouhal #


C=f/ph;             % TOTAL # of repetitions of the test procedure (i.e.
cases)
NUM=caseS:caseE;


N1 = 1;
for j = 1:C
    N1(j) = N1(j);              % starting file #
    N2(j) = N1(j)+ph-1;        % ending file #
    if j < C
        N1(j+1) = N2(j)+1;      % starting file # update
    end
end


tT = (1:ph)/ph;     % non-dimensional phase position
TIvalue2=zeros(130,ph,C);


for j = caseS:caseE
    count = 1;


    for i = N1(j):N2(j)
        %   load Average velocity field
        if i > 99 & i < 1000
            A = readimx(['Set' char(S)  '_' char(name) '/B00'
num2str(i) '.VC7']);
            B = readimx(['Set' char(S)  '_' char(nameRMS) '/B00'
num2str(i) '.VC7']);
            TKE = readimx(['Set' char(S)  '_' char(nameTKE) '/B00'
num2str(i) '.IM7']);
        elseif i >9 & i < 100
            A = readimx(['Set' char(S)  '_' char(name) '/B000'
num2str(i) '.VC7']);
            B = readimx(['Set' char(S)  '_' char(nameRMS) '/B000'
num2str(i) '.VC7']);
            TKE = readimx(['Set' char(S)  '_' char(nameTKE) '/B000'
num2str(i) '.IM7']);
        elseif i < 10
            A = readimx(['Set' char(S)  '_' char(name) '/B0000'
num2str(i) '.VC7']);
            B = readimx(['Set' char(S)  '_' char(nameRMS) '/B0000'
num2str(i) '.VC7']);
            TKE = readimx(['Set' char(S)  '_' char(nameTKE) '/B0000'
num2str(i) '.IM7']);
        end
        %_____
```

```matlab
        %    Spatially-averaged velocity data (vector)

[xx,yy,u,v] = showimxJ(A);      % extracting the position & velocity
components calculated by the DaVis PIV software
        Vinst = sqrt(u.^2+v.^2);           % calculating |V|, which has
been spatially averaged in DaVis

        VP(:,:,count) = double(Vinst(:,yp));      % velocities along
each of the yp selected (for PRmod.m)
%         Vmax(count,j)=max(max(VP(:,:,count))); % this is not used
anymore...

        %    1. local average of max velocity, excluding the sides by ±
"buf_Vmax" indices
        buf_Vmax=45;
        Vinst_buf=Vinst;                   % these four lines set the
"sides" to zero
        Vinst_buf(1:buf_Vmax,:)=0;
        Vinst_buf(size(Vinst,1)-buf_Vmax:size(Vinst,1),:)=0;
        Vinst_buf(:,max(yp)+1:end)=0;
        [mag1 ind1]=max(Vinst_buf);     % x-index
        tab_m=[mag1' ind1'];
        [mag2 ind2]=max(mag1);          % y-index
        if ind2>s_ave && ind2<(max(yp)-s_ave)
            Vmax(count,j)=mean(mean(Vinst_buf(tab_m(ind2,2)-
s_ave:tab_m(ind2,2)+s_ave,ind2-s_ave:ind2+s_ave)));
        elseif ind2<=s_ave
            Vmax(count,j)=mean(mean(Vinst_buf(tab_m(ind2,2)-
s_ave:tab_m(ind2,2)+s_ave,1:ind2+s_ave)));
        elseif ind2>=max(yp)-s_ave
            Vmax(count,j)=mean(mean(Vinst_buf(tab_m(ind2,2)-
s_ave:tab_m(ind2,2)+s_ave,ind2-s_ave:max(yp))));
        end

        %    2. instantaneous max velocity, based on reduced-size
velocity field
        Vmax2(count,j)=max(max(Vinst_buf));

        %    3. local average velocity at the point Alipour measured...
        Vtip(j,count)=mean(mean(Vinst(jc(j)-s_ave:jc(j)+s_ave,tip-
s_ave:tip+s_ave)));

        %_____
        %    RMS velocity data (vector)
        [xrms,yrms,urms,vrms] = showimxJ(B); % pulling out the position
& RMS components calculated by the DaVis PIV software
        Vrms = sqrt(urms.^2+vrms.^2);       % calculating |Vrms|

        %_____
        %    Turbulent kinetic energy data (scalar)
        [xtke,ytke,tke] = showimxJ(TKE);    % pulling out the position
& turbulent kinetic energy values calculated by the DaVis PIV software
        tke=tke';                           % inverting matrix so it's
x-y orientation matches the velocity data
        uprime=sqrt((2/3).*tke);
```

136

```matlab
%        TI=uprime'./(Vinst-Vrms);         % INPUT: normalized
turbulent intensity
        TI=sqrt(uprime.^2);                 % INPUT: Alipour t.i.
formulation

        if ExPlot==5
            for aa=1:length(ytke)
                Xtke(:,aa)=xtke;
            end
            for aa=1:length(xtke)
                Ytke(aa,:)=ytke;
            end
            figure(1)
            surf(Xtke,Ytke,double(TI))
            shading interp
            set(gca,'View',[0 90])
            xlabel('x, [mm]')
            ylabel('y, [mm]')
            grid off
            hold off
            axis image

            %% Resize for importing into word.  When importing into
word, reduce the
            %% image size by 50% to get a font size of 10 points and a
figure size of
            %% 3" x 4"
            FS=20;
            FigureHeight=8;
            FigureWidth=6;
            set(gcf, 'PaperPositionMode', 'manual');
            set(gcf, 'PaperUnits', 'inches');
            set(gcf, 'PaperPosition', [0 0 FigureWidth FigureHeight]);
            set(gcf, 'PaperSize', [FigureWidth FigureHeight]);
            set(gca,'FontSize',FS,'FontName','Times')
%             xlabel('\phase [°]')
%             ylabel('\downstream [mm]')
            if i<1000
                ImageName=['Set' char(S) '_' char(name) num2str(i)];
            end
            if i<100
                ImageName=['Set' char(S) '_' char(name) '0'
num2str(i)];
            end
            if i<10
                ImageName=['Set' char(S) '_' char(name) '00'
num2str(i)];
            end
            print(gcf,'-dtiff',ImageName)
            clf;
        end

        %   1. local average of turbulent intensity at point Alipour
measured...
        for q=1:length(tip)
            if ALIPOUR==1
```

137

```matlab
                TIvalue(j,count,q)=mean(mean(TI(jc(j)-
s_ave:jc(j)+s_ave,tip(q)-s_ave:tip(q)+s_ave)));
                TIvalue2(q,count,j)=mean(mean(TI(jc(j)-
s_ave:jc(j)+s_ave,tip(q)-s_ave:tip(q)+s_ave)));
            else
                TIvalue(j,count,q)=mean(TI(jc(j)-
hori:jc(j)+hori,tip(q)));

                TIvalue2(tip(q),count,j)=mean(TI(jc(j)-
hori:jc(j)+hori,tip(q)));
            end
        end

        count = count + 1;
    end

    if 0<G<3

PRmod(xx,yy,Thresh,Percent,VP,ph,yp,S,L,L2,NUM,j,buf,G,BadLim,bufx,...
        sca,ExPlot,Pau,js,jc,ord);
        sprintf('%g Case(s) remaining',caseE-j)
    end

end

for i=1:ph
    NN(i,:)=1:max(NUM);
end
HH=zeros(ph,max(NUM));
for i=1:max(NUM)
    HH(:,i)=1:ph;
end

if G==4
    if length(NUM)==1
        plot(H,Vmax,'o-')
        title(sprintf('Set %s, Case %g',char(S),j))
        ylabel('max velocity, [m/s]')
        xlabel('phase')
    else
        surf(HH,NN,double(Vmax))
        shading interp
        title(sprintf('Set %s',char(S)))
        zlabel('max velocity, [m/s]')
        xlabel('phase')
        ylabel('case')
    end
end

if G==5
    figure(1)
        plot((1:ph)*360/ph,TIvalue(tab(1,:),:,34),'o-')
        legend('false','duct','open')
        title('Left comparison')
        xlabel('phase')
```

```matlab
    ylabel('turbulent intensity')
    xlim([0 360])
    ylim([-2 12])
figure(2)
    plot((1:ph)*360/ph,TIvalue(tab(2,:),:,34),'o-')
    legend('false','duct','open')
    title('Center comparison')
    xlabel('phase')
    ylabel('turbulent intensity')
    xlim([0 360])
    ylim([-2 12])
figure(3)
    plot((1:ph)*360/ph,TIvalue(tab(3,:),:,34),'o-')
    legend('false','duct','open')
    title('Right comparison')
    xlabel('phase')
    ylabel('turbulent intensity')
    xlim([0 360])
    ylim([-2 12])
figure(4)
    plot((1:ph)*360/ph,TIvalue(tab_duct,:,34),'o-')
    legend('duct,L2','L1','C','R1','R2')
    title('duct')
    xlabel('phase')
    ylabel('turbulent intensity')
    xlim([0 360])
    ylim([-2 12])
figure(5)
    plot((1:ph)*360/ph,TIvalue(tab_fvf,:,34),'o-')
    legend('false,L','C','R')
    title('fvf')
    xlabel('phase')
    ylabel('turbulent intensity')
    xlim([0 360])
    ylim([-2 12])

figure(6)
    subplot(3,1,1)
    plot((1:ph)*360/ph,Vmax,'o-')
    title('local average')
    ylabel('max. velocity, [m/s]')
    xlabel('phase, [°]')
    legend(char(ord))
    ylim([0 80])

    subplot(3,1,2)
    plot((1:ph)*360/ph,Vmax2,'o-')
    title('instantaneous')
    ylabel('max. velocity, [m/s]')
    xlabel('phase, [°]')
    ylim([0 80])

    subplot(3,1,3)
    plot((1:ph)*360/ph,Vtip)
    title('local average @ Alipours point')
    ylabel('velocity, [m/s]')
```

```matlab
        xlabel('phase, [°]')

    figure(7)
        plot(fvf_data(2:end,1)*.000471947,Dh,'o')
        xlabel('t.a. flow rate, [m^3/s]')
        ylabel('Hydraulic diameter, [cm]')

    figure(8)
        plot(Re,St,'o')
        ylabel('Strouhal #')
        xlabel('Reynolds #')

%     figure(9)
%         plot(fvf_data(2:end,3),TI)
%         xlabel('sub-glottal pressure, [kPa]')
%         ylabel('turbulent intensity')
%
%     figure(10)
%         plot(St,TI)
%         xlabel('Strouhal #')
%         ylabel('turbulent intensity')
%
%     figure(11)
%         plot(Re,TI)
%         ylabel('turbulent intensity')
%         xlabel('Reynolds #')

    figure(9)
    for i=1:C
      subplot(3,3,i)
      surf(double(TIvalue2(:,:,i)))
      axis([1 ph 0 size(Vinst,2) 0 8])
      title(sprintf('%s',char(ord(i))))
%       set(gca,'View',[0 270])
      zlabel('turbulent intensity')
      ylabel('downstream location')
      xlabel('phase')
    end

%     figure(10)
    for i=1:C
%         subplot(3,3,i)
      figure(i+9)
      contourf(double(TIvalue2(:,:,i)))
      title(sprintf('%s',char(ord(i))))
      caxis([0 15])
      axis off
      set(gca,'View',[0 270])
%         colorbar
      zlabel('turbulent intensity')
      ylabel('downstream location')
      xlabel('phase')

      if ExPlot==4
          %% Resize for importing into word.  When importing into
word, reduce the
```

```matlab
                %% image size by 50% to get a font size of 10 points and a
figure size of
                %% 3" x 4"
                FS=20;
                FigureHeight=2*1.333;
                FigureWidth=2;
                set(gcf, 'PaperPositionMode', 'manual');
                set(gcf, 'PaperUnits', 'inches');
                set(gcf, 'PaperPosition', [0 0 FigureWidth FigureHeight]);
                set(gcf, 'PaperSize', [FigureWidth FigureHeight]);
                set(gca,'FontSize',FS,'FontName','Times')
                xlabel('\phase [°]')
                ylabel('\downstream [mm]')
                if i<1000
                    ImageName=['Set' char(S) '_' char(name) num2str(i)];
                end
                if i<100
                    ImageName=['Set' char(S) '_' char(name) '0'
num2str(i)];
                end
                if i<10
                    ImageName=['Set' char(S) '_' char(name) '00'
num2str(i)];
                end
                print(gcf,'-dtiff',ImageName)
                clf;
            end
        end
end

% figure(10);A=readimx('Set8_ave/B00035.VC7');[x,y,u,v]=showimx(A);
```

B.1.2   PRmod.m

```
%   PR.m
%
%   INPUTS:
%   1- Thresh:  threshold velocity value, below which velocity values
are
%               not used in search for jet core
%   2- Percent: % of maximum velocity to use as basis for defining jet
core
%   3- VPav:    imported PIV data file(s)
%
%   Finds the jet centerline using processed PIV vector fields.
%   1- Thresh:      finds all points of the velocity profile > Thresh
%   2- Smth:        smooths the actual velocity profile points
%   3- Smth2:       reduces Smth to only those points > Percent of max
V;
%                   all other values are set to zero
%   4- MeanSmth:    finds mean V value of non-zero Smth2 values
%   5- StdSmth:     finds std. dev. of non-zero Smth2 V values
%   6- xCenter:     finds x-value corresponding to MeanSmth; if V is
below
%                   Thresh, sets xCenter to far right
%   7- SmthCntr:    smooths the calculated jet centerline
%
%   by Dr. Thomson (modified by James Drechsel)
%   17May2007


% function [H]=PRmod(xx,yy,Thresh,Percent,VP,ph,yp,S,L,L2,NUM,j,buf,...
%               G,BadLim,bufx,sca,ExPlot,Pau,js,jc)
function PRmod(xx,yy,Thresh,Percent,VP,ph,yp,S,L,L2,NUM,j,buf,...
                G,BadLim,bufx,sca,ExPlot,Pau,js,jc,ord)


CaseNum = j;
LookAtEachJet = L;
Descrip = L2;


%   UNFREEZE THE VALUES MARKED BETWEEN (>>>>>) TO RUN PR.m
ALONE!!!!!!!!!!!
%   %>>>>>>>>>>>>>>>>>>>>>>>>>
% clc;
% clear all
%
% % INPUTS
% f=158;
% Thresh=2;
% Percent=0.8;
% yp=100:300;
% jc=134;
% S={'2_refined'};
% name={'ave'};
% ph=20;
% LookAtEachJet=0;
% Descrip=0;
% CaseNum=2;
% NUM=[1 1];
```

142

```matlab
% buf=0;
% G=2;
% bufx=ones(1,f/ph);% buffer to exclude far left x values, [index]
% bufx(5)=15;        % INPUT (case with wall in view)
% bufx(11)=15;       % INPUT (" ")
% bufx(17)=15;       % INPUT (" ")
% bufx(6)=30;        % INPUT (" ")
% bufx(12)=30;       % INPUT (" ")
% bufx(18)=30;       % INPUT (" ")
% BadLim=75;
% sca=0.25;
% ExPlot=0;
% Pau=0;
% js=[8 10 11 12 12 12 13 13 13 13 13 13];
%   %>>>>>>>>>>>>>>>>>>>>>>>>>

%   Initializing variables for mesh plot at end of code
Z = zeros(ph,length(yp));
y = zeros(ph,length(yp));
Center=zeros(ph,length(yp));
for m = 1:ph
    % Populating mesh plot variables
    for j=1:length(yp)
        Z(m,j)=j;
        y(m,j)=m;
    end

%   %>>>>>>>>>>>>>>>>>>>>>>>>>>>>
%     %   load Average velocity field
%     if m > 99 & m < 1000
%         A = readimx(['Set' char(S)  '_' char(name) '/B00' num2str(m)
'.VC7']);
%     elseif m >9 & m < 100
%         A = readimx(['Set' char(S)  '_' char(name) '/B000' num2str(m)
'.VC7']);
%     elseif m < 10
%         A = readimx(['Set' char(S)  '_' char(name) '/B0000'
num2str(m) '.VC7']);
%     end
%     [xx,yy,u,v] = showimxJ(A);     % pulling out the position &
velocity components calculted by the DaVis PIV software
%     V = sqrt(u.^2+v.^2);          % calculating |V|
%
%     VP(:,:,m) = double(V(:,yp));    % velocities along each of the
yp selected
%   %>>>>>>>>>>>>>>>>>>>>>>>>>>>>

    VPav = VP(:,:,m);
    VPav(1:bufx(CaseNum),:)=0;
    VPav(size(VP,1)-bufx(CaseNum):size(VP,1),:)=0;
    Vmax(m)=max(max(VP(:,:,m)));

    x=1:size(VPav,1);
    bad=ones(1);
    co=1;
    for i=1:size(VPav,2)
```

143

```matlab
        % Smooth velocity profile @ each yp selection using NSmth
points
        NSmth=7;
        Smth2=zeros(length(x),i);
        for j=1:length(x)
            if bufx<j<size(VPav,1)-bufx
                if (j<(NSmth+1)/2 || j>(length(x)-(NSmth-1)/2))
                    Smth(j,i)=VPav(x(j),i);
                else
                    Smth(j,i)=mean(VPav(x(j)-(NSmth-1)/2:j+(NSmth-
1)/2,i));
                end
            end
        end

        % Find maximum of smoothed jet
        [VMax,I]=max(Smth(:,i));

        % Define jet core by finding values where velocity is within
80% of VMax
        for j=1:length(x)
            if bufx<j<size(VPav,1)-bufx
                if Smth(j,i)>=Percent*VMax
                    Smth2(j,i)=Smth(j,i);
                end
            end
        end

        % Go along profile and find edges of jet core
        edge=0;
        for j=1:length(x)
            if bufx<j<size(VPav,1)-bufx
                if (Smth2(j,i)>0 && edge==0)
                    jMin=j;
                    edge=1;
                end
            end
        end
        edge=0;
        for j=length(x):-1:1
            if bufx<j<size(VPav,1)-bufx
                if (Smth2(j,i)>0 && edge==0)
                    jMax=j;
                    edge=1;
                end
            end
        end

        % Find where jet velocity is within one std. dev of core mean
        MeanSmth(i)=mean(Smth(jMin:jMax,i));
        StdSmth=1*std(Smth(jMin:jMax,i));        % INPUT: the "1"
indicates use of 1 standard deviation...
        edge=0;
        for j=1:length(x)
            if bufx<j<size(VPav,1)-bufx
```

```matlab
                if (Smth(j,i)>=(MeanSmth(i)-StdSmth) && edge==0)
                    jStdMin=j;
                    edge=1;
                end
            end
        end
        edge=0;
        for j=length(x):-1:1
            if bufx<j<size(VPav,1)-bufx
                if (Smth(j,i)>=(MeanSmth(i)-StdSmth) && edge==0)
                    jStdMax=j;
                    edge=1;
                end
            end
        end

        % Find center of points within one std dev of core mean
        xCenterBad(i)=mean(jStdMin:jStdMax);
        if MeanSmth(i)<Thresh
            xCenterBad(i)=size(VPav,1);
            bad(co)=i;
            co=co+1;
        end
        LB=length(bad);
    end

%     if LookAtEachJet == 1 && Descrip==1
%         figure(2)
%         plot(yp,MeanSmth,'k-',yp,Thresh,'r-')
%         title('MeanSmth & Thresh')
%         axis([min(yp) max(yp) 0 max(max(VPav))])
%     end

    % parameter of MATLAB function "resample()"; n=0 is best (nearest
neighbor interpolation)
    n = 0;
    % looks to see if "bad" jet angle values are a problem:
    % if there are no jet angles where MeanSmth<Thresh...
    if max(xCenterBad) < size(VPav,1)
        xCenter=xCenterBad;
        ch=0;
        if Descrip == 1
            disp('OK')
        end
    else
        % if at least one centerline point is "bad",then...
        % find index of max velocity values
        II=mean(max(Smth(:,1:5)));                          % "top"
half
        III=mean(max(Smth(:,length(yp)-5:length(yp))));     % "bottom"
half
        % if the max is on the top half...
        if II>III
            q = 1:length(yp);
            ch=1;
            if Descrip == 1
```

```matlab
                    disp('top')
                end
        else
            % if the max is on the bottom half...
            q = length(yp):-1:1;
            ch=2;
            if Descrip == 1
                disp('bottom')
            end
        end
        % create new arrays that run from either the top down to the
first
        % "bad" jet centerline point, or from the bottom up to the
first "bad"
        % jet centerline point. Curve fit these new smaller sections of
jet centerline
        % points and then increase the number of elements to match
length(yp)
        edge=0;
        for i=q
            if xCenterBad(i) == size(VPav,1) && edge==0
                if Descrip == 1
                    sprintf('i=%g\nlengthBad=%g',i,LB);
                end
                % if the jet is calculated to be too near the top or
bottom...
                if (i<=(2+buf) || i>=length(yp)-(1+buf))
                    % AND if there are a lot of bad center values
                    if LB>BadLim
                        edge=1;
                        ch=3;
                    % AND if there are NOT a lot of bad center values
                    elseif LB<BadLim
                        xChange=xCenterBad;
                        xChange(bad)=[];

xCenter=resample(xChange,length(yp),length(xChange),n);
                        edge=1;
                        if Descrip==1
                            disp('curve fit with FEW BAD points');
                        end
                    end
                % regardless of # of bad center values AND the jet is
                % NOT calculated to be too near the top or bottom...
                else
                    if ch==1
                        ys=1:(i-2-buf)/(length(yp)-1):i-1-buf;
                        Short=resample(xCenterBad(1:i-1-
buf),length(yp),length(xCenterBad(1:i-1-buf)),n);
                    elseif ch==2
                        ys=i+1+buf:(length(yp)-(i+1+buf))/(length(yp)-
1):length(yp);

Short=resample(xCenterBad(i+1+buf:length(yp)),length(yp),length(xCenter
Bad(i+1+buf:length(yp))),n);
                    end
```

146

```matlab
                        % correct for "resample()" error which references
output to zero
                        for bb=1:length(Short)
                            if Short(bb)==0
                                Short(bb)=Short(bb-1);
                            end
                        end

                        Z(m,:)=ys;              % replaced original Z values
with the new, shorter ones from resample() function
                        xCenter=Short;
                        edge=1;
                    end
                end
            end
    end

    if ch~=3
        % Smooth center curve
        for i=1:size(VPav,2)
            if (i<3 || i>size(VPav,2)-2)
                SmthCntr(i)=xCenter(i);
            else
                SmthCntr(i)=mean(xCenter(i-2:i+2));
            end
        end

        Center(m,:)=SmthCntr(:);

    end

    if Descrip==1
        sprintf('%g phases remaining',ph-m)
    end

    % Surface plot & velocity profile
    if LookAtEachJet==1
        figure(1)
        % I EXCLUDED THE PLOTTING CODE BELOW BECAUSE I DON'T NEED TO
SEE THE JET ANGLE
        % CALCULATION METHOD ANYMORE.
        % REINSERT IT IF YOU'RE UNSURE HOW THE METHOD WORKS...
%    %>>>>>>>>>>>>>>>>>>>>>>>>>>>>>>>>>>>>
        if G==3
            subplot(211)
            plot(x,VPav(:,i))
            hold on
%         plot(x,Smth(:,i),'r',x(I),VMax,'go',[0 128],[Thresh
Thresh],':k',...
%              x(jStdMin:jStdMax),Smth(jStdMin:jStdMax,i),'g.',...
%              [jMin jMax],[MeanSmth MeanSmth],...
%              [64 xCenter(i)],[0 MeanSmth]); ylim([0 40]);
%              title('Sample velocity profile & improvements')
%              xlabel('x, [index]')
%              ylabel('velocity, [m/s]')
%              hold off
```

147

```matlab
%               legend('profile','Smth')
              subplot(212)
              surf(VPav)
              ylabel('x, [index]')
              xlabel('y, [index]')
              title(sprintf('Jet angle\nSet %s, Case # %g, phase %g of
%g',char(S),CaseNum,m,ph))
              shading interp
              set(gca,'View',[90 90],'CLim',[0 70])
              axis equal
              axis tight
              zlim([0 80])
              colorbar
          else
%     %>>>>>>>>>>>>>>>>>>>>>>>>>>>>>>>>>>>>>>>
              surf(VPav)
              ylabel('x, [index]')
              xlabel('y, [index]')
              title(sprintf('Jet angle\nSet %s, Case # %g, phase %g of
%g',char(S),CaseNum,m,ph))
              shading interp
              set(gca,'View',[90 90],'CLim',[0 45])
              axis equal
              axis tight
              zlim([0 80])
              colorbar
          end

          if ch~=3
              hold on
              z=zeros(size(xCenter))+79;
              plot3(Z(m,:),xCenter,z,'g');
              plot3(Z(m,:),SmthCntr,z,'k','LineWidth',2);
              hold off
          end

          if Pau==1
              pause;
          end

          % to export/save image to file
          if ExPlot==1 || ExPlot==3
              ImageName=['VECTOR_Set' char(S) '_Case' num2str(CaseNum)
...
                  '_Thresh' num2str(Thresh) '_phase' num2str(m)];
              print(gcf,'-dtiff',ImageName)
          end

      end

      % changing the scale of Z from (yp, [index]) to (y, [mm])
      calib=(max(yy(1,:))-min(yy(1,:)))/size(yy,2);       % conversion
from index to mm, [mm/index]
      for i=1:length(yp)
          Z(m,i)=(Z(m,i)+min(yp)-1)*calib;
      end
```

```matlab
    if G==6
        hold on
        Center(m,:)
        SSS=round(Center(m,:));
        surf(VPav(SSS,:),'g');
        hold off
    end

end

% automating numbering of plots
if G~=3
    if length(NUM)==1
        figure(1)
    else
        if NUM(1)==NUM(2) || LookAtEachJet==1
            figure(1)
        else
            figure(NUM(CaseNum-min(NUM)+1))
        end
    end
end

% reordering the phase plots so start of jet growth is first...
H=[js(CaseNum):ph 1:js(CaseNum)-1];
CenAd=Center(H,:);
ZAd=Z(H,:);

% mesh plotting code
if G==1
    % removing the phases with no visible jet...
    cou=1;
    if min(min(CenAd))==0
        for i=1:ph
            if mean(CenAd(i,:))==0
                Zer(cou)=i;
                cou=cou+1;
            end
        end
        CenAd(Zer,:)=[];
        y(Zer,:)=[];
        ZAd(Zer,:)=[];
    end

    mesh(y,CenAd,-ZAd); xlabel('phase'); ylabel('Center, [index]');
zlabel('downstream');
    title(sprintf('Set %s, Case # %g',char(S),CaseNum))
%       ylim([0 size(VPav,2)]); xlim([0 380]); zlim([min(min(yy)) 0]);

% 2-D line plotting code
elseif G==2

    for i=1:ph
```

```matlab
        % removing the phases with no visible jet...
        if mean(CenAd(i,:))==0
            continue
        end

        clineh=[i i]*(360/ph);
        clinev=[min(yy(1,:)) max(yy(1,:))];
        plot(clineh,clinev,':','Color',[1 1 1]*0.5)
        hold on
        Offset=clineh(1);
        plot((CenAd(i,:)-jc(CaseNum))*sca+i*(360/ph),...
            -ZAd(i,:)+max(yy(1,:)),'k')

        xlabel('phase (°)')
        ylabel('downstream (mm)')
        %title(sprintf('Set %s, Case # %g,
%s',char(S),CaseNum,char(ord(CaseNum))))
        title(sprintf('%s',char(ord(CaseNum))))
        set(gca,'TickDir','out')
        ylim([yy(1,max(yp))-0.5 yy(1,min(yp))+0.5])
        xlim([0 15*360/ph])

        %% Resize for importing into word.
        set(gcf,'Units','inches')
        set(gcf,'Position',[2 5 10 4])
        FS=8;
        FigureHeight=1.5;
        FigureWidth=7;
        set(gcf, 'PaperPositionMode', 'manual');
        set(gcf, 'PaperUnits', 'inches');
        set(gcf, 'PaperPosition', [0 0 FigureWidth FigureHeight]);
        set(gcf, 'PaperSize', [FigureWidth FigureHeight]);
        set(gca,'FontSize',FS,'FontName','Times')
    end
    hold off

    if Pau==1
        pause;
    end
end

% to export/save image to file
if ExPlot==2 || ExPlot==3
    ImageName=['Set' char(S) '_Case' num2str(CaseNum) '_Thresh'
num2str(Thresh)];
    print(gcf,'-dtiff',ImageName)
end
```

B.1.3   MATLAB code for extracting lateral glottal displacement from .avi images

```matlab
%   N = total number of specimens to include

clc;
%clf;
clear all

%   Labeling specimens
spec = 28;   % INPUT: specimen #

%   Amplitude
%   VFMRG Glottal Width (by Jake Munger)

% This program will calculate the glottal width of a vocal fold test.

%%                    DIRECTIONS

% Enter the file name of the start picture for filename_1.

% When the pictures appear, select the points in the following order
%       1) zoom in on the left side
%       2) press enter to un-pause the program
%       3) select the left side of specimen
%       4) zoom in on the right side
%       5) press enter to un-pause the program
%       6) select the right side of specimen
%  Repeat the zooming, un-pausing, and point selection for:
%       9) Left reference on ruler
%      10) 2cm to the right of the left reference
%    *****Be sure to select the top of the ruler for each of the
previous
%         two measurements******

format short g
clc;
clf;
clear all;

count = 1;

condition = 1;        % condition for while loop to continue or stop

while condition ~= 0
    %indicate the filename for the desired picture
    filename_1 = input('Please enter the name of the file (ending with
.jpg):\nEnter "0" when done.')

    for i = 1:4
        A = imread(filename_1);
        image(A);
        title('Glottal Amplitude')
        axis image
        pause;
        [x y] = ginput(1);
        point_1(i,1) = x;
```

```matlab
        point_1(i,2) = y;

    end

    %specimen left, right
    %Starting Reference Left and right
    SL = point_1(1,:);
    SR = point_1(2,:);
    SRL = point_1(3,:);
    SRR = point_1(4,:);

    gw_px = (SR(1,1)-SL(1,1));         % glottal width, [pixel]

    start_2_cm = sqrt((SRR(1,1)-SRL(1,1))^2+(SRR(1,2)-SRL(1,2))^2);
    one_cm = start_2_cm/2;

    gw_cm = gw_px/one_cm;

    amp(count,1) = count;
    amp(count,2) = gw_cm;

    count = count+1;

    xlswrite('C:\Documents and
Settings\Administrator\Desktop\Jameson\duct-open\Duct open Vocal fold
pictures for amplitude analysis\28\amp_28.xls'...
    ,amp)

    if filename_1 == 0
        condition = 0;
    else
        continue
    end
end
```
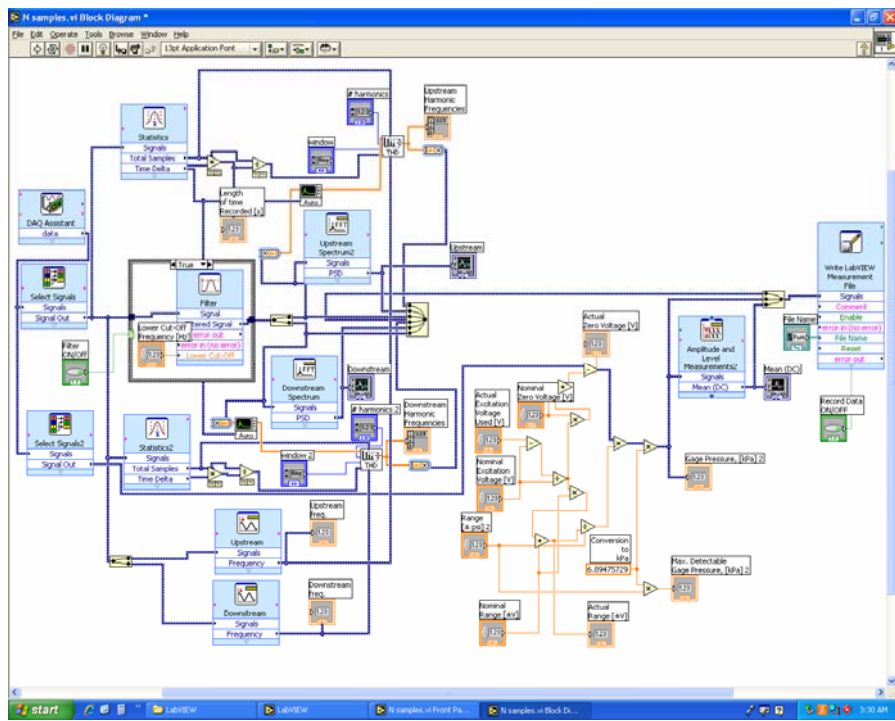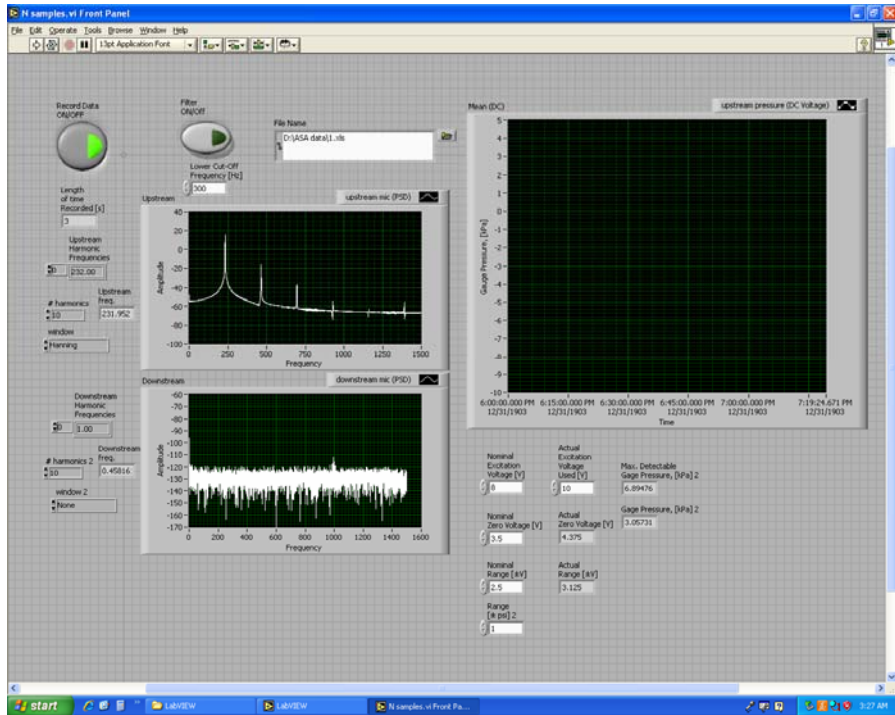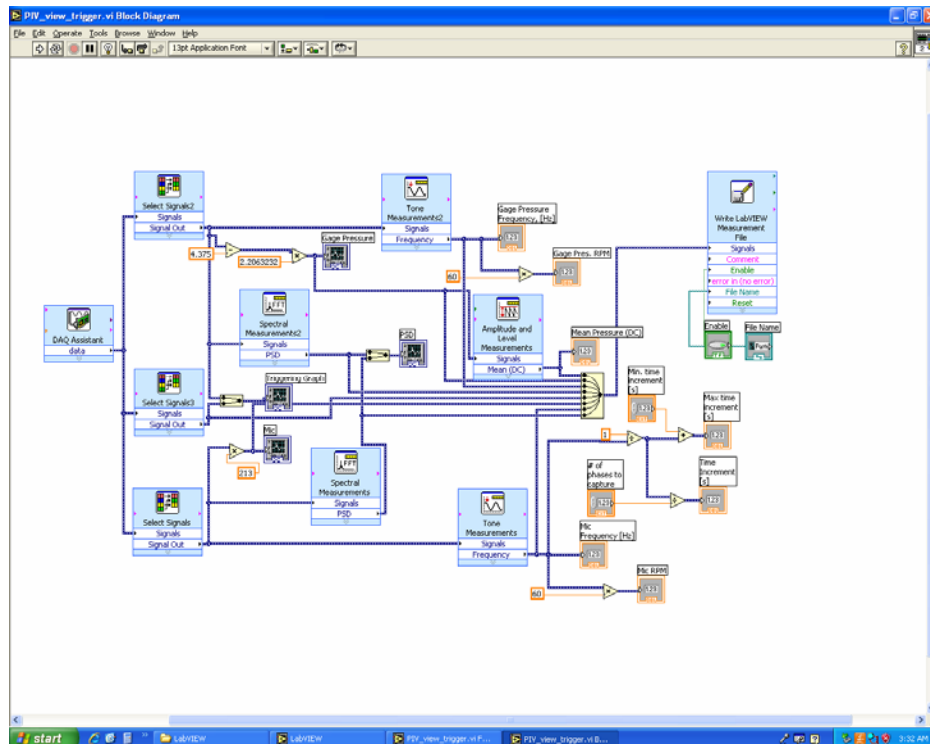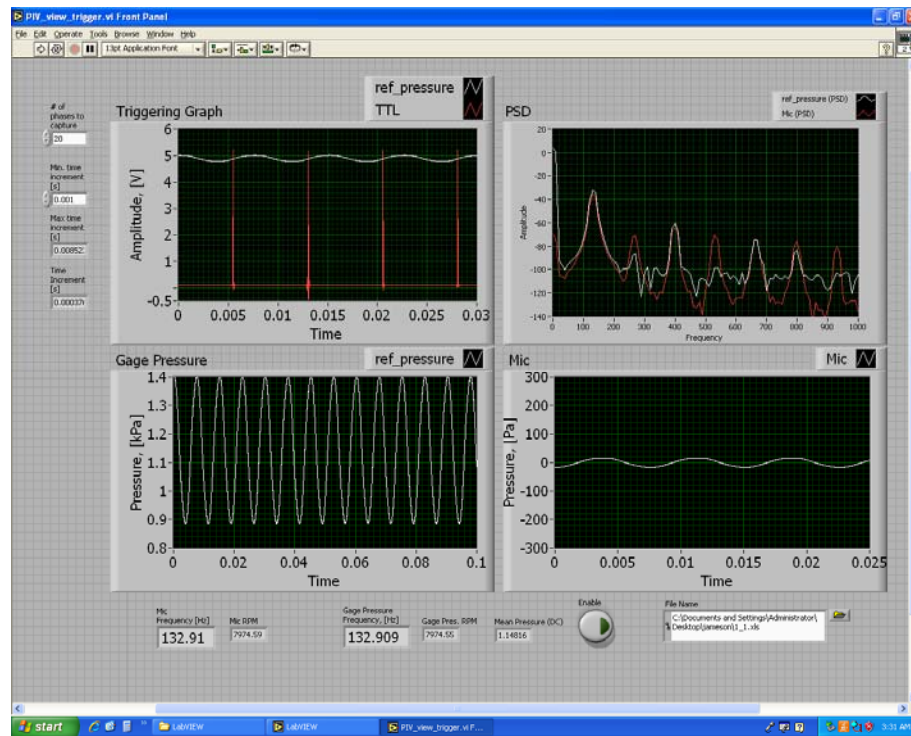
B.2 LabVIEW VI:

Nsamples (used to acquire data used in Chapter 3)

PIV trigger VI (used to acquire frequency, pressure, and trigger signal data)

C.   Sedimentation Effects and Seed Particle Inertia

Appropriate selection of seed particles used in PIV analysis, or any flow visualization, allows the fluid flow to be visualized. This occurs because the particles are large enough to be seen, but assumed to be small enough to not influence the flows normal behavior.

Several potential problems exist when choosing a seed particle, which include sedimentation and inertia issues. In slow flows, sedimentation can occur. Sedimentation refers to the accumulation of the seed particle due to its relatively high mass compared to that of the fluid. This is a problem if, for instance, the flow is horizontally but the particles are sinking vertically.

Inertial problems refer to the length of time required for a seed particle to move at the same speed as the flow. If the particle is relatively heavy, it will take some amount of time and length for the particle speed to match the flow speed.

What follows is a brief analysis of these issues, which results in an expression to test for the maximum particle size (diameter) that can be safely assumed to be neutrally buoyant in the flow.

C.1 Sedimentation

From a force balance on the seed particle in the vertical direction, the force of gravity on the seed particle is opposed by a buoyancy force and a viscous drag force:

$$\sum F_y = 0 \text{ and } F_{buoy} + F_{drag} = mg .$$

If

$$F_{buoy} = \rho_{fluid} V g = \rho_{fluid} \frac{4}{3} \pi r^3 g ,$$

$$F_{drag} = \frac{1}{2} \rho_{fluid} U_\infty^2 A C_D = 6 \pi \mu_{fluid} U_\infty r , \text{ and}$$

$$mg = \frac{4}{3} \pi r^3 \rho_{particle} g ,$$

then,

$$U_\infty = \frac{2}{9} \frac{r^2 g (\rho_{particle} - \rho_{fluid})}{\mu_{fluid}} , \qquad \textbf{(C.1)}$$

where μ is absolute (dynamic) viscosity, ρ is density, r is the particle radius, and g is the acceleration due to Earths gravity.

If $U_\infty << U_{fluid}$, then sedimentation should not be an issue. Relevant values are shown in Table C-1; for this research, sedimentation was clearly not a concern, given the high values of U_{fluid} (~40 m/s) compared to U_∞.

Table C-1 Sample sedimentation calculation.

	Fluid			Particle		u_∞
g	ρ	μ	ρ	radius		
(m/s^2)	(kg/m^3)	(N-s/m^2)	(kg/m^3)	(m)		(m/s)
9.81	1.21	1.85E-05	912	5.00E-07		2.68E-05

156

C.2 Inertia

When a seed particle is introduced into a fluid flow, it takes a finite amount of time for the particle to catch up to the speed of the flow. This time could be considered to be a time constant, and the system could be modeled as a 1st order system.

Assuming that both fluid and seed particles are moving in the same direction, but that the seed particle is moving more slowly than the flow, the force on the seed particle due to the relative fluid velocity is as follows,

$$F_{drag} = (ma)_{particle},$$

$$(ma)_{particle} = m_{particle} \frac{dU_{particle}}{dt}, \text{ and}$$

$$F_{drag} = 6\pi\mu r \left(u_{fluid} - u_{particle} \right).$$

Assuming a spherical particle shape, that u_{fluid} is constant, and that

$$U^* = \left(u_{fluid} - u_{particle} \right),$$

then

$$\frac{dU^*}{dt} = -\frac{dU_{particle}}{dt}, \text{ and}$$

$$\frac{1}{U^*} \frac{dU^*}{dt} = -\frac{9}{2} \frac{\mu_{fluid}}{r^2 \rho_{particle}} = -\frac{1}{\tau}. \qquad \textbf{(C.2)}$$

Equation C.2 is solved for τ, which is a time constant for the 1st order system model, and where μ is absolute (dynamic) viscosity, ρ is density, and r is the particle radius. Note that Equation C.2 is very similar to Equation C.1.

These equations result in a 1st-order response equation with a time constant, τ.
This last expression can be integrated to obtain a useful 1st-order equation,

$$\left[u_{fluid}(t) - u_{particle}(t)\right] = [u_{fluid}(0) - u_{particle}(0)]e^{\frac{-t}{\tau}}. \qquad \textbf{(C.3)}$$

This expression can be used to determine how long it takes the seed particle velocity to accelerate to within some percentage of the fluid velocity. Using velocity values similar to those measured in this thesis, consider $u_{fluid} = 60$ m/s (the high end of velocities measured in this thesis) and that the acceptable percentage error between particle and fluid velocity is 1%. Assuming $u_{particle} = 0$ at $t = 0$ (an extreme case), and using C.2 and C.3, then the values in Table C-2 are obtained.

Table C-2 Sample seed particle inertia calculation.

Fluid			Particle					
ρ (kg/m^3)	μ (N-s/m^2)	u(0) (m/s)	ρ (kg/m^3)	radius (m)	u(0) (m/s)	τ (μs)	t (μs)	L (cm)
1.21	1.85E-05	60	912	5.00E-07	0	2.74	12.6	0.0757

L is a conservative estimate for the distance that the seed particle would have to travel in order to be accelerated to match the fluid velocity. It is evident that L is very short compared with the tube lengths used in this research between the plenum and the vocal fold model. Also note that $t \ll$ period of vibration (~0.01 seconds). Therefore, the seed particles were sufficiently small.